Visualizing and characterizing excited states from time-dependent density functional theory

John M. Herbert[a*]

Time-dependent density functional theory (TD-DFT) is the most widely-used electronic structure method for excited states, due to a favorable combination of low cost and semi-quantitative accuracy in many contexts, even if there are well recognized limitations. This Perspective describes various ways in which excited states from TD-DFT calculations can be visualized and analyzed, both qualitatively and quantitatively. This includes not just orbitals and densities but also well-defined statistical measures of electron–hole separation and of Frenkel-type exciton delocalization. Emphasis is placed on mathematical connections between methods that have often been discussed separately. Particular attention is paid to charge-transfer diagnostics, which provide indicators to diagnose when TD-DFT may not be trustworthy due to its categorical failure to describe long-range electron transfer. Measures of exciton size and charge separation that are directly connected to the underlying transition density are recommended over more *ad hoc* metrics for quantifying charge-transfer character.

1 Introduction

Amongst various formulations of density functional theory (DFT) for electronic excited states,[1] by far the most widely used is linear-response DFT.[1–5] For historical reasons,[6] that formulation is commonly known as "time-dependent" (TD-)DFT,[1,5–8] despite the absence of time in its static, frequency-domain formulation. Semantics aside, the linear-response TD-DFT formalism has a pleasing familiarity for chemists, as it can be cast in the form of an eigenvalue problem in a space of singly-substituted Slater determinants. This is analogous to the method of configuration interaction with single substitutions (CIS),[9] but incorporating dynamical electron correlation in the TD-DFT case. In favorable contexts, including the electronic spectroscopy of many medium-sized organic molecules, TD-DFT achieves a mean accuracy of ~ 0.3 eV for vertical excitation energies,[1,10–14] which is often sufficient for solution-phase spectroscopy. At the same time, TD-DFT's formal scaling and computational cost are comparable to ground-state DFT,[8,15] meaning that it is often the only *ab initio* method for excited states that can address large chemical systems. These considerations have made TD-DFT into the *de facto* workhorse of computational electronic spectroscopy.

The present work provides an overview of visualization and analysis methods for linear-response TD-DFT, going beyond molecular orbitals (MOs) and aiming to describe (and potentially quantify) how charge is rearranged upon electronic excitation.

Both density-based and orbital-based visualization tools are considered, as are certain atomic partitions of the density change upon excitation,

$$\Delta\rho(\mathbf{r}) = \rho_{\text{exc}}(\mathbf{r}) - \rho_0(\mathbf{r}) . \tag{1.1}$$

These can be used to characterize the nature of an excited state in both qualitative and quantitative terms. Many of these analysis and visualization methods have been around for a long time, but only occassionally have the connections between them been discussed,[1,16–22] and often in a general form for correlated wave functions with arbitrary levels of excitation.[18–22] This obscures certain simplifications that are possible for CIS- and TD-DFT-type wave functions, for which the particle–hole picture is clear and explicit. The present work is limited to those particular *ansätze*, with an emphasis on connections between different visualization and analysis tools that exist in the literature.

Especially relevant are a variety of charge-transfer (CT) metrics.[22–27] These can be used as prognosticators of (potentially catastrophic) problems with conventional TD-DFT's description of long-range CT.[1,28–33] The practical effect is that TD-DFT significantly underestimates excitation energies for states having significant CT character,[1,9,34–36] including Rydberg states.[11,34] Although significant progress has been made towards correcting this behavior,[37–39] via long-range corrected (LRC) density functionals[40–46] and other range-separated hybrid (RSH) schemes,[47–51] it remains important to possess a means to diagnose problematic cases.

The remainder of this work is organized as follows. Section 2

a Department of Chemistry & Biochemistry, The Ohio State University, Columbus, Ohio 43210 USA E-mail: herbert@chemistry.ohio-state.edu

provides a brief introduction to the formalism of linear-response TD-DFT and also introduces some visualization tools based on the density matrix, which are more incisive than simply plotting $\Delta\rho(\mathbf{r})$ in real space. Orbital-based visualization tools, which remain the most popular means for qualitative characterization of an excited state, are introduced in Section 3. To quantify charge rearrangement during excitation, it is useful to introduce an atomic partition of $\Delta\rho(\mathbf{r})$ that can be made into a metric for CT, and can also assist in understanding states that are delocalized across more than one chromophore. These tools are introduced in Section 4. Section 5 introduces additional ways to quantify exciton delocalization that have a direct connection to the underlying Kohn-Sham wave function or transition density. Finally, the CT problem in TD-DFT is described in Section 6 along with a discussion of various metrics that can be used to indicate when (and for which excited states) this becomes an issue.

2 Theoretical background

We begin with a brief recapitulation of the linear-response TD-DFT formalism (Section 2.1), then introduce densities and density matrices for ground and excited states (Section 2.2). Attachment and detachment densities,[52] which are important tools for excited-state visualization, are introduced in Section 2.3.

2.1 Linear-response TD-DFT

Mathematical derivations of linear-response TD-DFT, starting from time-dependent response theory applied to the Kohn-Sham ground state, can be found elsewhere;[1–5] see Ref. 1 for a pedagogical version. The linear-response formalism is what is most often implied by "TD-DFT", as it is (by far) the most common form. An explicitly time-dependent or "real-time" formalism also exists,[1,53–55] which can be used to describe attosecond electron dynamics in an external electric field.[56–63] For excitation energies and most molecular electronic spectroscopy applications, however, the real-time method is much less efficient.[15] Real-time methods are not considered here, and visualization tools are somewhat different for that approach.[64–69]

Starting from the ground-state solution of the Kohn-Sham eigenvalue problem,[70]

$$\hat{F}\psi_r = \varepsilon_r \psi_r , \qquad (2.1)$$

the basic equation of linear response theory is

$$\begin{pmatrix} \mathbf{A} & \mathbf{B} \\ \mathbf{B}^* & \mathbf{A}^* \end{pmatrix} \begin{pmatrix} \mathbf{x}^{(n)} \\ \mathbf{y}^{(n)} \end{pmatrix} = \omega_n \begin{pmatrix} \mathbf{1} & \mathbf{0} \\ \mathbf{0} & -\mathbf{1} \end{pmatrix} \begin{pmatrix} \mathbf{x}^{(n)} \\ \mathbf{y}^{(n)} \end{pmatrix} . \qquad (2.2)$$

This is a non-Hermitian eigenvalue problem for the excitation amplitudes $\mathbf{x}^{(n)} = (x_{ia}^{(n)})$ and de-excitation amplitudes $\mathbf{y}^{(n)} = (x_{ia}^{(n)})$, for the nth excited state whose vertical excitation energy is ω_n. Throughout this work, we use indices $i, j, \ldots$ to denote occupied MOs; $a, b, \ldots$ to indicate virtual (unoccupied) MOs; and $r, s, \ldots$ to denote arbitrary MOs. Spin indices are omitted here; see Ref. 1 for a version of these equations that includes them. The matrices $\mathbf{A}$ and $\mathbf{B}$ in eqn. (2.2) are Hessians with respect to orbital rotations.[1,71] In the canonical MO basis that diagonalizes the Fock matrix $\mathbf{F}$, their matrix elements are

$$A_{ia,jb} = (\varepsilon_a - \varepsilon_i)\delta_{ij}\delta_{ab} + \frac{\partial F_{ia}}{\partial P_{jb}} \qquad (2.3a)$$

and

$$B_{ia,jb} = \frac{\partial F_{ia}}{\partial P_{bj}} , \qquad (2.3b)$$

where $\mathbf{P}$ is the one-electron density matrix. Expressions for $\mathbf{A}$ and $\mathbf{B}$ in terms of electron repulsion integrals and the exchange-correlation (XC) kernel can be found elsewhere.[1,8,9] Lastly, the quantities $\varepsilon_a - \varepsilon_i$ in eqn. (2.3a) are differences between virtual (ε_a) and occupied (ε_i) Kohn-Sham energy levels defined by the ground-state eigenvalue problem, eqn. (2.1). The difference $\varepsilon_a - \varepsilon_i$ appears along the diagonal of $\mathbf{A}$ and constitutes a zeroth-order approximation to an electronic excitation energy, consistent with a zeroth-order picture in which an electronic transition consists in promotion of one electron from a single occupied MO into a single virtual MO, $\psi_i \rightarrow \psi_a$.

A TD-DFT calculation consists of the iterative solution of eqn. (2.2) for a certain number of excited states, each characterized by vectors $\mathbf{x}^{(n)}$ and $\mathbf{y}^{(n)}$. These are subject to an unconventional normalization,

$$\sum_{ia} (x_{ia}^2 - y_{ia}^2) = 1 , \qquad (2.4)$$

consistent with the metric matrix in eqn. (2.2).[4,72–74] For brevity, we omit the state index n in eqn. (2.4) and subsequent expressions. Amplitudes $\{x_{ia}\}$ and $\{y_{ia}\}$ parameterize the *transition density matrix* (TDM) for the excitation in question. As a position-space kernel, that object is[4,8,73]

$$T(\mathbf{r},\mathbf{r}') = \sum_{ia} \left[x_{ia}\,\psi_a(\mathbf{r})\,\psi_i^*(\mathbf{r}') + y_{ia}\,\psi_i(\mathbf{r})\,\psi_a^*(\mathbf{r}') \right] . \qquad (2.5)$$

It provides one possible visualization tool, usually in the form of the *transition density*, $T(\mathbf{r}) \equiv T(\mathbf{r},\mathbf{r})$.

Often, eqn. (2.2) is simplified by invoking the Tamm-Dancoff approximation (TDA),[3,75] in which the de-excitation amplitudes y_{ia} are neglected. These amplitudes arise naturally in the equation-of-motion formalism for the one-particle density matrix,[4,74] yet in molecular TD-DFT calculations they are typically $\sim 100\times$ smaller than the largest x_{ia}. (This may not always be the case for solids.[76,77]) The matrix $\mathbf{B}$ is absent from the resulting TDA eigenvalue problem, which is simply

$$\mathbf{A}\mathbf{x} = \omega\mathbf{x} . \qquad (2.6)$$

For historical reasons,[78] the original eigenvalue problem in eqn. (2.2) is sometimes called the *random phase approximation* (RPA),[9] in order to distinguish it from the simpler Hermitian eigenvalue problem in eqn. (2.6). That terminology is avoided here, so as not to confuse it with other methods known as RPA.[78–81] Where we need to make a distinction, we refer to eqn. (2.2) as "full" TD-DFT and eqn. (2.6) as TD-DFT/TDA.

Use of the TDA is often essential for avoiding triplet instabilities and obtaining accurate triplet excitation energies.[82–85] Triplet instabilities in the ground-state Kohn-Sham solution indicate that an unrestricted wave function would lower the energy with respect to the (unstable) closed-shell solution,[86] and these instabilities manifest as negative excitation energies.[87] Triplet instabilities are common at bond-stretching geometries, where singlet and triplet states become quasi-degenerate,[88,89] but may also occur near the ground-state geometry when the fraction of Hartree-Fock exchange is large,[90–95] or for large values of the range separation parameter in RSH or LRC functionals.[82,83,96–98] Beyond indicating an instability, solutions with negative excitation energies are not physically meaningful and can lead to convergence failure in solving eqn. (2.2), if the iterative algorithm is predicated on the excitation energies being positive. Invoking the TDA decouples the stability problem from the excitation energy problem and is used in most calculations that are described here.

The TDA simplifies the structure of the transition density into a form where one can imagine a Kohn-Sham wave function[2,99] (determinant) whose form is analogous to the CIS *ansatz*, namely

$$\left|\Psi_{\text{exc}}\right\rangle = \sum_i^{\text{occ}} \sum_a^{\text{vir}} x_{ia}\left|\Psi_i^a\right\rangle, \tag{2.7}$$

Here, $\left|\Psi_i^a\right\rangle$ is a Slater determinant that differs from the ground state by a single substitution, $\psi_i \to \psi_a$. Given this form for $\left|\Psi_{\text{exc}}\right\rangle$, the real-space kernel $T(\mathbf{r},\mathbf{r}')$ in eqn. (2.5) can be connected to its more general definition in wave function theory,[17,73] which is

$$T(\mathbf{r},\mathbf{r}') = N \int \Psi_0^*(\mathbf{r}',\mathbf{r}_2,\ldots,\mathbf{r}_N)\,\Psi_{\text{exc}}(\mathbf{r},\mathbf{r}_2,\ldots,\mathbf{r}_N)\,d\mathbf{r}_2\cdots d\mathbf{r}_N, \tag{2.8}$$

where $\Psi_0(\mathbf{r}_1,\ldots,\mathbf{r}_N)$ is the ground-state wave function. The definition of $T(\mathbf{r},\mathbf{r}')$ in Eq. (2.8) is also valid for correlated wave functions.[18]

It has been argued that eigenvalue differences $\varepsilon_a - \varepsilon_i$ should be good approximations to true excitation energies in *exact* Kohn-Sham theory,[99–102] albeit without spin coupling so there is no distinction between excitations to different spin multiplicities. To the extent that this remains true in *approximate* DFT, one might imagine that configuration mixing in eqn. (2.7) occurs to a lesser extent in TD-DFT as compared to CIS, which is indeed observed to be the case.[103] For example, Figs. 1a and 1b compare amplitudes x_{ia} for $S_0 \to S_1$ excitation of formaldehyde, computed using TD-DFT/TDA with the PBE functional and also with the Hartree-Fock functional, equivalent to the CIS method. The TD-PBE eigenvector consists almost exclusively of the $2b_2 \to 2b_1$ amplitude whereas in a converged CIS calculation (including all virtual orbitals), this amplitude accounts for less than 20% of the norm of the transition density. (These calculations were performed using a real-space electronic structure code,[104] so there is no finite-basis approximation. CIS results with conventional Gaussian basis sets are shown in Fig 1c.) Truncating the virtual space leads to a more compact expansion and a larger $2b_2 \to 2b_1$ coefficient in the CIS case, but this has a disastrous effect on the excitation energy (Fig 1b). This is not a useful strategy.

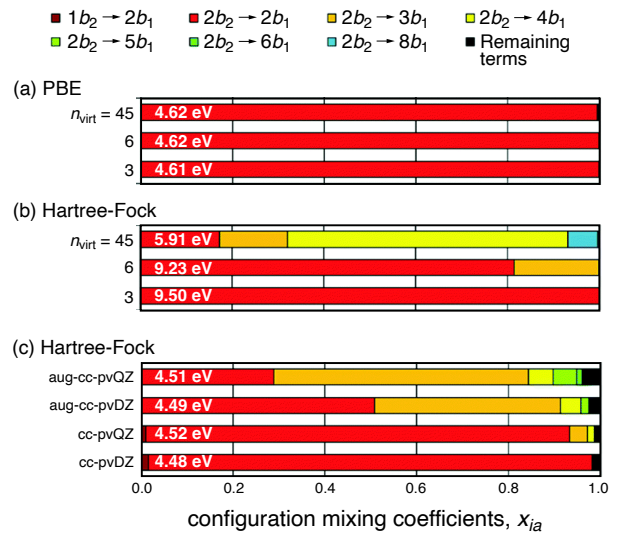That said, significant configuration mixing may be an unavoid-

Fig. 1 Bar graph of configuration mixing coefficients x_{ia} for the $1\,^1A_2$ state of formaldehyde: (a) TD-PBE/TDA calculations using active spaces containing n_{virt} virtual orbitals, as implemented in a real-space electronic structure code; (b) CIS calculations using the same active spaces; and (c) conventional CIS calculations in Gaussian basis sets. Calculated excitation energies provide a measure of convergence with respect to active space or basis set. Adapted from Ref. [103].

able consequence of using hybrid functionals that contain some fraction of "exact" (Hartree-Fock) exchange. Virtual MOs in Hartree-Fock theory experience an N-electron potential rather than a $(N-1)$-electron potential,[105] so the virtual levels ε_a are upshifted such that even the frontier virtual MOs are often unbound ($\varepsilon_a > 0$). These are discretized continuum states,[106] and a large number of them will need to mix together in order to generate the localized wave function of a bound excited state. Inclusion of diffuse basis functions, which are often necessary to obtain converged excitation energies,[7,107] also generate significant configuration mixing as shown in Fig. 1c.

Configuration mixing muddies the picture of electron and hole, so it is desirable to have alternative ways of visualizing an excitation besides plotting a potentially large number of occupied and virtual MOs, corresponding to the significant amplitudes x_{ia}. To that end, we next introduce excited-state electron densities that can be used to visualize an excitation in real space.

2.2 Densities and density matrices

Within TD-DFT, the density matrix for an excited state can be expressed as

$$\mathbf{P}_{\text{exc}} = \mathbf{P}_0 + \Delta\mathbf{P}^{\text{elec}} + \Delta\mathbf{P}^{\text{hole}} + \mathbf{Z}. \tag{2.9}$$

Here, $\mathbf{P}_0$ is the ground-state density matrix and

$$\Delta\mathbf{P} = \Delta\mathbf{P}^{\text{elec}} + \Delta\mathbf{P}^{\text{hole}} \tag{2.10}$$

is the (unrelaxed) difference density matrix. The quantity $\mathbf{Z}$ is the so-called "Z-vector" contribution that accounts for orbital relaxation in the excited state.[8,94,108]

The "particle" (or electron) and "hole" components of $\Delta\mathbf{P}$ are

available from the TD-DFT response vectors:[94,108–110]

$$\Delta\mathbf{P}^{\text{elec}} = \tfrac{1}{2}\left[(\mathbf{x}+\mathbf{y})^{\dagger}(\mathbf{x}+\mathbf{y}) + (\mathbf{x}-\mathbf{y})^{\dagger}(\mathbf{x}-\mathbf{y})\right] \qquad (2.11a)$$

$$\Delta\mathbf{P}^{\text{hole}} = -\tfrac{1}{2}\left[(\mathbf{x}+\mathbf{y})(\mathbf{x}+\mathbf{y})^{\dagger} + (\mathbf{x}-\mathbf{y})(\mathbf{x}-\mathbf{y})^{\dagger}\right]. \qquad (2.11b)$$

Expressions for the matrix elements in the MO basis can be simplified to afford[109]

$$(\Delta\mathbf{P}^{\text{elec}})_{ab} = \sum_{i}(x_{ia}^{*}x_{ib} + y_{ia}^{*}y_{ib}) \qquad (2.12a)$$

$$(\Delta\mathbf{P}^{\text{hole}})_{ij} = -\sum_{a}(x_{ia}x_{ja}^{*} + y_{ia}y_{ja}^{*}). \qquad (2.12b)$$

These quantities are normalized such that

$$\text{tr}(\Delta\mathbf{P}^{\text{elec}}) = 1 = -\text{tr}(\Delta\mathbf{P}^{\text{hole}}). \qquad (2.13)$$

Although we have not been explicit about spin indices, the spin-orbital indices (i, a, etc.) could be limited to either α or β spin. By doing so, one could obtain a spin density matrix for either the particle ($\Delta\mathbf{P}_{\alpha}^{\text{elec}} - \Delta\mathbf{P}_{\beta}^{\text{elec}}$) or the hole ($\Delta\mathbf{P}_{\alpha}^{\text{hole}} - \Delta\mathbf{P}_{\beta}^{\text{hole}}$), whose real-space representation would reveal spin polarization for an open-shell system.

Whereas $\Delta\mathbf{P}$ is available from $\mathbf{x}$ and $\mathbf{y}$ alone, calculation of $\mathbf{Z}$ in eqn. (2.9) requires solution of the coupled-perturbed equations that are associated with the TD-DFT excited-state gradient.[94,110] The density matrix $\mathbf{P}_{\text{exc}}$ that includes $\mathbf{Z}$ is known as the "relaxed" density matrix, whereas

$$\mathbf{P}_{\text{unrlx}} = \mathbf{P}_{0} + \Delta\mathbf{P} \qquad (2.14)$$

is the unrelaxed density matrix. Examples illustrating the role of $\mathbf{Z}$ are deferred to Section 2.3.

The quantities $\Delta\mathbf{P}^{\text{elec}}$ and $\Delta\mathbf{P}^{\text{hole}}$ can be conceptualized as separate densities for the excited electron and the hole that it leaves behind in the occupied space. More precisely, this is true of the real-space densities $\Delta\rho_{\text{elec}}(\mathbf{r})$ and $\Delta\rho_{\text{hole}}(\mathbf{r})$ that are encoded by these density matrices. Unlike the difference density,

$$\Delta\rho(\mathbf{r}) = \Delta\rho_{\text{elec}}(\mathbf{r}) + \Delta\rho_{\text{hole}}(\mathbf{r}), \qquad (2.15)$$

which exhibits both positive and negative regions in space, $\Delta\rho_{\text{elec}}(\mathbf{r}) \geq 0$ everywhere in space, and $\Delta\rho_{\text{hole}}(\mathbf{r}) \leq 0$. Sometimes it is more informative to visualize these two quantities separately. It is therefore suggested that $\Delta\rho_{\text{elec}}(\mathbf{r})$ should be called the *particle density* and $\Delta\rho_{\text{hole}}(\mathbf{r})$ the *hole density*. (These terms are sometimes used differently,[18] but our usage is consistent with the idea of $\Delta\mathbf{P}^{\text{hole}}$ as the density matrix for the hole.[72]) An example is depicted in Fig. 2, where the particle and hole densities can be visually superimposed by the reader to suggest the difference density $\Delta\rho(\mathbf{r})$, which is also shown. The $\mathbf{Z}$-vector contribution is omitted in this example, so these are unrelaxed densities.

The molecule in Fig. 2 is a polyfluorene oligomer with a single keto defect (fluorenone) in one of the terminal monomer units.[111] It provides an example of how particle and hole densities are useful for interpreting excited states that are strongly mixed in the canonical MO basis, meaning there are numerous
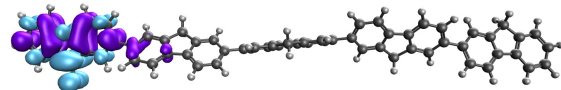

(a) particle (attachment) density
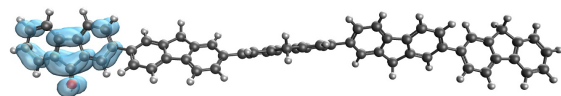
(b) hole (detachment) density
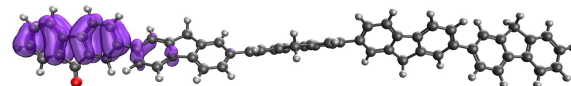
(c) difference density

(d) transition density

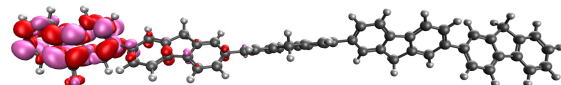**Fig. 2** Unrelaxed densities for the $S_0 \to S_2$ transition of a five-unit fluorenone-terminated polyfluorene whose leftmost fluorene unit contains a carbonyl defect: (a) particle density ($\Delta\rho_{\text{elec}}$), (b) hole density ($\Delta\rho_{\text{hole}}$), (c) difference density ($\Delta\rho = \Delta\rho_{\text{elec}} + \Delta\rho_{\text{hole}}$), and (d) transition density $T(\mathbf{r})$. TD-DFT/TDA calculations were performed at the CAM-B3LYP/3-21G* level. Adapted from Ref. 1; copyright 2023 Elsevier.

amplitudes x_{ia} that are similar in magnitude. In this particular example, the frontier MOs are completely delocalized along the length of the oligomer, which is not atypical for π-conjugated chromophores. Nevertheless, it is obvious from the densities in Fig. 2 that the excited state in question is localized as a result of the defect. This is *not* obvious within the canonical MO basis, however, wherein the transition density consists of a roughly equal mixture of four different $\psi_i \to \psi_a$ excitations, as shown in Fig. 3a. Localization arises from phase interference in a coherent superposition of four terms, but this is essentially impossible to discern by inspecting the relevant MOs alone.

2.3 Attachment and detachment densities

For CIS and TD-DFT calculations, the particle and hole densities defined in Section 2.2 coincide precisely with the *attachment density* and the *detachment density*, respectively, quantities that were originally defined in a manner that is not be limited to single-excitation theories.[52] This definition sheds additional light on the nature of $\Delta\mathbf{P}^{\text{elec}}$ and $\Delta\mathbf{P}^{\text{hole}}$ in TD-DFT. First, let us diagonalize a difference density matrix $\Delta\mathbf{P}$ and express the result in the form

$$\mathbf{U}^{\dagger}(\Delta\mathbf{P})\mathbf{U} = \begin{pmatrix} \mathbf{a} & \mathbf{0} \\ \mathbf{0} & \mathbf{d} \end{pmatrix} \qquad (2.16)$$

where the nonzero blocks $\mathbf{a}$ and $\mathbf{d}$ are diagonal matrices that contain the positive and the negative eigenvalues of $\Delta\mathbf{P}$, respectively. Density matrices corresponding to the attachment and detachment densities are then defined as[16,17,52]

$$\Delta\mathbf{P}^{\text{attach}} = \mathbf{U} \begin{pmatrix} \mathbf{a} & \mathbf{0} \\ \mathbf{0} & \mathbf{0} \end{pmatrix} \mathbf{U}^{\dagger} \qquad (2.17a)$$

(a) canonical molecular orbitals

HOMO–1 — 20% → LUMO

HOMO–2 — 26% → LUMO

HOMO–3 — 21% → LUMO

HOMO–4 — 20% → LUMO
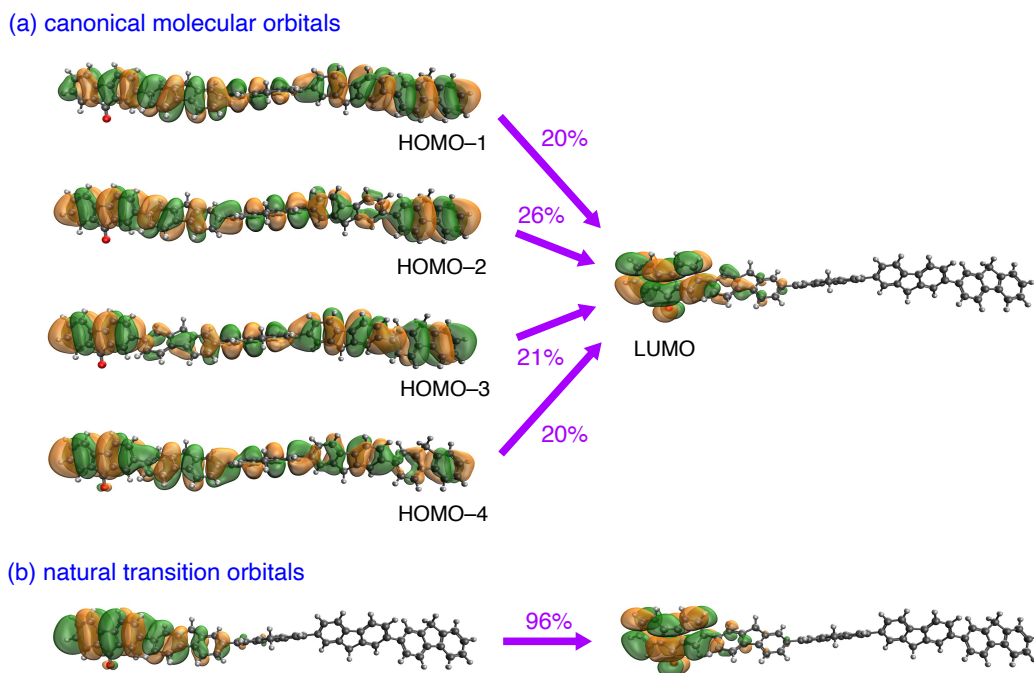
(b) natural transition orbitals

96%

Fig. 3 Transition density for the fluorenone-terminated polyfluorene oligomer that is also depicted in Fig. 2, viewed here in two different representations: (a) the canonical MO representation, with weights x_{ia}^2 given as percentages, and (b) the NTO representation, with a single weight λ_1^2 that is also given as a percentage. TD-DFT/TDA calculations were performed at the CAM-B3LYP/3-21G* level. Adapted from Ref. 1; copyright 2023 Elsevier.

and

$$\Delta \mathbf{P}^{\text{detach}} = \mathbf{U} \begin{pmatrix} \mathbf{0} & \mathbf{0} \\ \mathbf{0} & \mathbf{d} \end{pmatrix} \mathbf{U}^\dagger . \qquad (2.17b)$$

Note that $\Delta \mathbf{P}^{\text{attach}}$ is positive semidefinite and $\Delta \mathbf{P}^{\text{detach}}$ is negative semidefinite.

This procedure could be followed for any difference density matrix, including the relaxed one from a TD-DFT calculation, or one that is obtained from a correlated wave function. In the special case that $\Delta \mathbf{P}$ is the unrelaxed difference density matrix from a TD-DFT calculation [eqn. (2.10)], it follows that $\Delta \mathbf{P}^{\text{attach}} \equiv \Delta \mathbf{P}^{\text{elec}}$ and $\Delta \mathbf{P}^{\text{detach}} \equiv \Delta \mathbf{P}^{\text{hole}}$. Although this equivalence has been noted before,[1,17] it does not seem to be widely appreciated. It arises from a unique feature of single-excitation theories, namely, a direct correspondence between CI coefficients and matrix elements of the TDM.[18,73,74,112] In the CIS case, for example, $x_{ia} = \langle \Psi_{\text{exc}} | \hat{a}_a^\dagger \hat{a}_i | \Psi_0 \rangle$.

Considering the specific case of $\Delta \mathbf{P}$ in eqn. (2.10), qualitative insight into the nature of an excited state can often be gleaned by analyzing its particle and hole components, $\Delta \mathbf{P}^{\text{elec}}$ and $\Delta \mathbf{P}^{\text{hole}}$. It must be borne in mind, however, that electron/hole separation does not survive the contribution from orbital relaxation, i.e., from $\mathbf{Z}$ in eqn. (2.9). Nonzero matrix elements $Z_{ia} = Z_{ai}$ introduce occupied–virtual coupling, in contrast to the occupied–occupied and virtual–virtual terms that define the unrelaxed difference density [eqn. (2.12)]. However, one may construct the

relaxed difference density,

$$\Delta \mathbf{P}_{\text{rlx}} = \mathbf{P}_{\text{exc}} - \mathbf{P}_0 = \Delta \mathbf{P} + \mathbf{Z} , \qquad (2.18)$$

and substitute this for $\Delta \mathbf{P}$ in eqn. (2.16). This defines attachment and detachment contributions to the relaxed density and recovers a particle/hole picture that includes orbital relaxation.

Orbital relaxation effects can be especially significant for states with CT character, as demonstrated in Fig. 4 for the case of a donor–acceptor complex consisting of naphthalene and tetra-cyanoquinone. Unrelaxed particle and hole densities (on the left in Fig. 4) suggest that the S_1 state of the complex has almost perfect CT character, with the excited electron localized on the acceptor (tetracyanoquinone) and the hole localized on the donor (naphthalene). A dipole moment change $\Delta \mu = 14.9$ D upon excitation underscores this CT character. However, the corresponding relaxed densities (on the right in Fig. 4) are both delocalized over both monomers. The change in dipole moment computed from the relaxed density is substantially reduced although still quite large: $\Delta \mu = 10.9$ D. Note that the excitation energy is precisely the same regardless of which densities are used to visualize the transition, as is the ground-state dipole moment of 1.3 D, but the value of the excited-state dipole moment depends substantially on whether it is computed using the relaxed or unrelaxed density matrix for the excited state.

This example underscores the fact that the use of $\Delta \mathbf{P}_{\text{rlx}}$ rather than $\Delta \mathbf{P}$ can have a significant effect on excited-state properties,[108,113,118] especially for states with a high degree of CT character.[108] The relaxed dipole moment, which is the *correct* dipole moment for the excited state (according to linear response the-

unrelaxed   **relaxed**
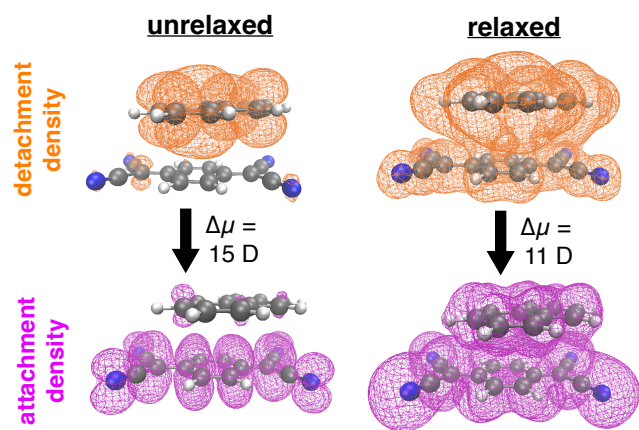
$\Delta\mu = 15\,D$ $\Delta\mu = 11\,D$

Fig. 4 Relaxed and unrelaxed detachment densities (upper images, in orange) and attachment densities (lower images, in magenta) for the $S_0 \rightarrow S_1$ transition of a donor–acceptor complex involving naphthalene and tetracyanoquinone. Calculations were performed at the TD-ωB97X-D/6-31G* level within the TDA and all densities are plotted using 90% iso-probability contours. Unrelaxed densities (on the left), corresponding to density matrices in eqn. (2.11), are localized on either the donor or the acceptor. Relaxed densities (on the right) are delocalized over both molecules, although the state maintains significant CT character as evidenced by the dipole moment change upon excitation, $\Delta\mu$.

Table 1 Excitation energies and excited-state dipole moments compared to experiment.[a]

Molecule & Method	ΔE (eV)	μ (D)[b]	
		unrelaxed	relaxed
formaldehyde ($^1A_2$)			
TD-BLYP	3.82	-0.05	-1.34
TD-B3LYP	3.98	-0.22	-1.40
TD-BH&HLYP	4.08	-0.39	-1.40
TD-HF	4.39	-0.60	-1.26
CASSCF(12,10)			-1.29
experiment	4.07[c]		-1.56 ± 0.07[d]
p-nitroaniline (^{1}CT)			
TD-BLYP	3.61	23.57	11.71
TD-B3LYP	4.07	20.81	12.40
TD-BH&HLYP	4.63	16.81	12.43
TD-HF	4.89	11.53	10.71
CASSCF(12,12)			16.35
experiment	4.24[e]		13.35[f]

[a] Data are from Ref. 113 except where indicated. [b] Minus signs indicate that the dipole moment changes direction upon excitation. [c] Ref. 114. [d] Ref. 115. [e] Ref. 116. [f] Ref. 117.

ory), is computed as $\mu_x^{\mathrm{rlx}} = \mathrm{tr}(\boldsymbol{\mu}_x \mathbf{P}_{\mathrm{exc}})$ for the x component, and its unrelaxed analog is $\mu_x^{\mathrm{unrlx}} = \mathrm{tr}(\boldsymbol{\mu}_x \mathbf{P}_{\mathrm{unrlx}})$. In Table 1, these two quantities are juxtaposed for the first excited state of formaldehyde ($^1A_2$), and for an excited state of p-nitroaniline that is characterized by CT from the amino group to the nitro group. Even for the comparatively benign case of formaldehyde, use of the relaxed density alters the total dipole moment by more than 1 D for several different density functionals, bringing the value much closer to experiment. The contrast is more dramatic for p-nitroaniline, whose ^{1}CT state exhibits a large dipole moment ($\mu \approx 13$ D),[117,119] leading to significant orbital relaxation. For certain functionals, the unrelaxed density overestimates the excited-state dipole moment by more than a factor of two, although the effect decreases as the fraction of exact exchange is increased. (Relaxed and unrelaxed dipole moments differ by more than a factor of two for formaldehyde as well,[113,118] but the dipole moment is much smaller in that case.)

Although relaxed densities are required for reliable and quantitative excited-state property calculations, there is much qualitative information to be gleaned from unrelaxed densities. For example, the CT nature of the donor $\rightarrow$ acceptor transition in the naphthalene–tetracyanoquinone dimer (Fig. 4) comes through in both the relaxed and unrelaxed dipole moments, even if orbital relaxation serves to delocalize both particle and hole across both monomers. Other examples considered below will neglect the **Z**-vector contribution, which is adequate for a quick survey of the nature of the excited states.

3 Natural transition orbitals

Densities reveal how charge is moved around upon excitation but they sacrifice the phase (sign) information that is contained in the orbitals, which might be helpful for understanding the character

of an excited state. If the number of significant amplitudes x_{ia} is small, then the canonical Kohn-Sham MOs are a good way to visualize the state in question while retaining phase information, but this may be inconvenient if there are too many participating amplitudes, which is often the case with hybrid functionals and high-quality basis sets.

The quantity $T(\mathbf{r}, \mathbf{r}')$ that is defined in eqns. (2.5) and (2.8) does contain phase information, and can be plotted in three-dimensional space by setting $\mathbf{r} = \mathbf{r}'$. However, the transition density $T(\mathbf{r}) \equiv T(\mathbf{r}, \mathbf{r})$ cannot be directly interpreted in terms of the movement of charge. For example, consider the transition density for the fluorenone-terminated polyfluorene oligomer that was considered above (Fig. 2d). Although its nodal structure contains elements of the nodal structures of both $\Delta\rho_{\mathrm{elec}}(\mathbf{r})$ and $\Delta\rho_{\mathrm{hole}}(\mathbf{r})$, the transition density $T(\mathbf{r})$ is clearly distinct from the difference density $\Delta\rho(\mathbf{r})$. What can be gleaned from $T(\mathbf{r})$ is the nature of the transition moment for the excitation in question, which must lie along the long axis of the molecule in Fig. 2d because the negative and positive lobes of $T(\mathbf{r})$ approximately cancel along the short axis. Clearly, the result of the fluorenone defect is that this particular excited state is a property of the terminal monomer (fluorenone), not a property of the whole polymer. That fact is not obvious from the canonical MOs that participate in the transition, which are shown in Fig. 3a. The *natural transition orbitals* (NTOs),[120] which are plotted in Fig. 3b and introduced below, will help to recover an electron/hole picture within a representation that contains phase information.

3.1 Theory

Starting from $\Delta\mathbf{P}^{\mathrm{elec}}$ and $\Delta\mathbf{P}^{\mathrm{hole}}$ in eqn. (2.12), phase information can be restored (in a manner that maximally preserves the qualitative characteristics of these densities) by using their eigenvectors to define a change-of-basis for the canonical MOs. The

transformation $\mathbf{U}_\text{o}$ that diagonalizes $\Delta\mathbf{P}^\text{hole}$ defines a transformation of the occupied MOs that we express as

$$\mathbf{U}_\text{o}^\dagger(\Delta\mathbf{P}^\text{hole})\mathbf{U}_\text{o} = \underbrace{\begin{pmatrix} \lambda_1^2 & 0 & 0 & \cdots \\ 0 & \lambda_2^2 & 0 & \cdots \\ & & \ddots & 0 \\ 0 & \cdots & 0 & \lambda_{n_\text{occ}}^2 \end{pmatrix}}_{\mathbf{\Lambda}^2}. \qquad (3.1)$$

The $n_\text{occ} \times n_\text{occ}$ diagonal matrix $\mathbf{\Lambda}^2$ contains the eigenvalues of $\Delta\mathbf{P}^\text{hole}$. (It is the square of a diagonal matrix $\mathbf{\Lambda}$ that will be introduced in Section 3.2, where we will discover that the values λ_i have their own significance.) Eigenvalues of $\Delta\mathbf{P}^\text{hole}$ are non-negative, which we indicate by writing them as λ_i^2, and they are normalized such that $\sum_i \lambda_i^2 = 1$ [*cf.* eqn. (2.13)]. In similar fashion, we introduce a matrix $\mathbf{U}_\text{v}$ that diagonalizes $\Delta\mathbf{P}^\text{elec}$,

$$\mathbf{U}_\text{v}^\dagger(\Delta\mathbf{P}^\text{elec})\mathbf{U}_\text{v} = \begin{pmatrix} -\mathbf{\Lambda}^2 & \mathbf{0} \\ \mathbf{0} & \mathbf{0} \end{pmatrix}, \qquad (3.2)$$

which defines a transformation of the virtual MOs. For single-excitation wave functions, the matrices $\Delta\mathbf{P}^\text{elec}$ and $\Delta\mathbf{P}^\text{hole}$ have the same eigenvalues, up to a sign,[111,120] so $\mathbf{\Lambda}^2$ is the same matrix in both eqns. (3.1) and (3.2). (Extra zeros in the latter are needed to dimension the matrices consistently.)

The matrix $\mathbf{U}_\text{o}$ transforms the canonical occupied MOs into a set of "hole" orbitals that we will call $\{\psi_i^\text{hole}(\mathbf{r})\}$, while $\mathbf{U}_\text{v}$ transforms the canonical virtual MOs into a corresponding set of "particle" (or "electron") orbitals $\{\psi_i^\text{elec}(\mathbf{r})\}$ where $i = 1,\ldots,n_\text{occ}$ in both cases; even for the virtual orbital transformation in eq. (3.2), there are only n_occ nonzero eigenvalues. These transformed orbitals are the NTOs for the hole and for the excited electron, respectively. They are potent tools for qualitative analysis because they reduce the $2n_\text{occ}n_\text{virt}$ excitation amplitudes x_{ia} and y_{ia} into just n_occ unique amplitudes, as discussed further in Section 3.2. For now, we simply note that the particle and hole densities are weighted averages of single-NTO probability densities:

$$\Delta\rho_\text{elec}(\mathbf{r}) = \sum_{i=1}^{n_\text{occ}} \lambda_i^2 \left| \psi_i^\text{elec}(\mathbf{r}) \right|^2 \qquad (3.3a)$$

$$\Delta\rho_\text{hole}(\mathbf{r}) = -\sum_{i=1}^{n_\text{occ}} \lambda_i^2 \left| \psi_i^\text{hole}(\mathbf{r}) \right|^2. \qquad (3.3b)$$

Examples of NTOs are provided in Sections 3.3 and 3.4.

The term "NTO" was first suggested by Martin in 2003,[120] but this form of analysis was introduced much earlier by Luzanov and co-workers.[121,122] It has since been rediscovered (and expressed in the notation used above) by others.[112,120,123] The terminology reflects the sense in which "natural" is used in quantum chemistry to mean eigenfunctions of a density matrix.[124–126] Just as *natural orbitals* are eigenfunctions of $\mathbf{P}$ (even in the case of a correlated wave function),[124] with eigenvalues that are *natural occupation numbers*, the NTOs diagonalize the TDM. Within a single-excitation model, this is equivalent to diagonalizing the unrelaxed difference density matrix $\Delta\mathbf{P}$, although that equivalence is lost in the case of a correlated wave function. (In the latter case, one

must distinguish between NTOs that diagonalize the TDM and the *natural difference orbitals* (NDOs) that diagonalize the difference density matrix.[18,19]) Similarly, *natural ionization orbitals* diagonalize the difference density obtained upon electron removal.[127] None of these quantities should be confused with *natural bond orbitals* or any of the other "natural" concepts introduced by Weinhold and co-workers.[128–130]

3.2 Interpretation

The transformations in eqns. (3.1) and (3.2) fully define the NTOs in TD-DFT, but an equivalent and illustrative definition is possible. Keeping to the TDA case for simplicity, we consider $\mathbf{x}$ to be a rectangular matrix of dimension $n_\text{occ} \times n_\text{virt}$. Hole and particle NTOs are defined by separate unitary transformations of the occupied and virtual MOs ($\mathbf{U}_\text{o}$ and $\mathbf{U}_\text{v}$, respectively), and an equivalent definition of these two transformations involves a singular value decomposition (SVD) of $\mathbf{x}$:

$$\mathbf{U}_\text{o}^\dagger \mathbf{x} \mathbf{U}_\text{v} = \begin{pmatrix} \mathbf{\Lambda} & \mathbf{0} \\ \mathbf{0} & \mathbf{0} \end{pmatrix}. \qquad (3.4)$$

Here, $\mathbf{\Lambda}$ is the $n_\text{occ} \times n_\text{occ}$ matrix of singular values λ_i, the same matrix that appears (as $\mathbf{\Lambda}^2$) in eqs. (3.1) and (3.2). According to eqn. (3.4), the matrices $\mathbf{U}_\text{o}$ and $\mathbf{U}_\text{v}$ contain the left and right singular vectors of $\mathbf{x}$, respectively, but they are identical to the eponymous transformations defined as eigenvectors of $\Delta\mathbf{P}^\text{hole}$ and $\Delta\mathbf{P}^\text{elec}$.

As compared to the how NTOs were introduced in Section 3.1, the construction in eqn. (3.4) demonstrates more clearly why no more than n_occ of the singular values are non-zero, and shows why the eigenvalues of $\Delta\mathbf{P}^\text{hole}$ and $\Delta\mathbf{P}^\text{elec}$ occur in pairs.[120] From yet another point of view, eqn. (3.4) is a special case of a *corresponding orbitals* transformation,[131–133] which selects a subset of virtual orbitals in one-to-one correspondence with the occupied orbitals. In this case, the NTOs are obtained from the corresponding orbitals transformation that diagonalizes the TDM.

If $\Delta\mathbf{P}^\text{hole}$ is dominated by a single NTO then so is $\Delta\mathbf{P}^\text{elec}$, which is a consequence of the correspondence between amplitudes x_{ia} and elements of the one-particle density matrix (Section 2.3). As a result, for single-excitation theories (only), the NTOs are equivalent to excited-state natural orbitals.[112] For CIS-type wave functions, the eigenvalues in the natural orbital basis (*i.e.*, the natural occupation numbers) can be specified in terms of the singular values of the transition amplitudes:[112]

$$n_r = \begin{cases} 1 - \lambda_r^2, & 1 \le r \le n_\text{occ} \\ \lambda_r^2, & n_\text{occ} < r \le 2n_\text{occ} \\ 0, & r > 2n_\text{occ} \end{cases}. \qquad (3.5)$$

The values $n_r = 1 - \lambda_r^2$ represent the hole that is created, and $n_r = \lambda_r^2$ correspond to the excited electron; this demonstrates why $\Delta\mathbf{P}^\text{elec}$ and $\Delta\mathbf{P}^\text{hole}$ have the same eigenvalues, up to a sign. Redundant orbitals ($n_r = 0$) have been eliminated by the SVD in eqn. (3.4). Although the direct connection between the excitation amplitudes, transition density, and one-electron density matrix for the excited state is a unique feature of the single-excitation

ansatz, the concept of attachment and detachment densities as eigenfunctions of $\Delta\mathbf{P}$, separable based on the sign of the eigenvalues in eqns. (2.16) and (2.17), is generalizable to wave functions of arbitrary complexity. The individual eigenfunctions of $\Delta\mathbf{P}$, which are the NDOs,[18] then generalize the concept of NTOs for many-body theories, without the need to introduce "correlated NTOs".[134]

Notice also that the TDM is diagonal in the NTO basis:

$$T(\mathbf{r},\mathbf{r}') = \sum_i^{n_{occ}} \lambda_i \, \psi_i^{elec}(\mathbf{r}) \left[\psi_i^{hole}(\mathbf{r}') \right]^* . \qquad (3.6)$$

This constitutes another proof that the transformation to NTOs distills a given excitation into the smallest possible number of occupied/virtual orbital pairs. In a well-defined sense, the NTO basis is the best choice for conceptualizing excited states in terms of a one-electron promotion from an occupied MO into a virtual MO. The NTOs are state-specific, so this optimal basis changes from one excited state to the next. (State-averaged NTOs have been suggested as a compact basis for correlated wave function expansions.[18]) In eqns. (3.1) and (3.2), we have written the eigenvalues of $\Delta\mathbf{P}^{elec}$ and $\Delta\mathbf{P}^{hole}$ as λ_r^2 in order to emphasize the correspondence with probabilities x_{ia}^2 in the canonical MO basis, whereas the singular values λ_r in eqn. (3.4) are the amplitudes themselves, rotated into the NTO basis.

For chemists, there exists a temptation to designate the orbitals comprising the first NTO pair (having the largest singular values λ_i) as "HONTO" and "LUNTO",[135–157] in analogy to the highest occupied MO (HOMO) and lowest unoccupied MO (LUMO). (The terms "HOTO" and "LUTO" have also been used.[111,158]) This seems to be especially prevalent in the literature on thermally-activated delayed fluorescence (TADF) emitters.[144–157] As even some who use this terminology have acknowledged,[137] this usage is incorrect insofar as "highest" and "lowest" are typically used in the context of the *aufbau* principle, whereas orbital energies are undefined in the NTO basis because the Fock matrix is not diagonal. As such, it makes no sense to discuss the energies of NTOs, and this makes the "HONTO" and "LUNTO" terminology especially confusing when discussed alongside HOMO/LUMO energy gaps, as is often done in the TADF literature. In this author's view, the terms "HONTO/LUNTO" should be avoided, so that visual descriptions of NTOs are kept separate from arguments based on one-electron energy levels. In discussing the NTO pairs with the largest singular values, a more appropriate term is *principal transition orbitals*, or perhaps *principal NTOs* (pNTOs). The full set of NTOs can be labeled pNTO, pNTO − 1, pNTO − 2, ..., in order of decreasing singular values $\lambda_1 > \lambda_2 > \lambda_3 > \cdots$. That is the nomenclature that will be used here.

3.3 Examples

Equation (3.3) demonstrates how the NTOs extract the most important contributions to the particle and hole densities, or in other words the most significant contributions to the unrelaxed attachment and detachment densities. In the case where there is only one significant singular value ($\lambda_1^2 \approx 1$), then $|\psi_1^{elec}(\mathbf{r})|^2 \approx \Delta\rho_{elec}(\mathbf{r})$ and $|\psi_1^{elec}(\mathbf{r})|^2 \approx \Delta\rho_{hole}(\mathbf{r})$, which are unrelaxed attachment and
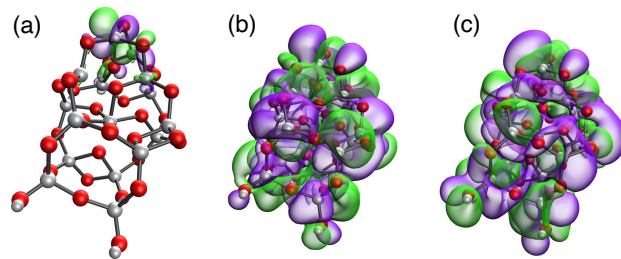

Fig. 5 Orbitals participating in the lowest titanium K-edge transition in $Ti_{16}O_{32}H_2$, computed using TD-DFT/TDA (PBE0/def2-ma-SVP). (a) The principal electron NTO $\psi_1^{elec}(\mathbf{r})$, for which $\lambda_1^2 = 1.00$. (b–c) Two canonical virtual MOs $\psi_a(\mathbf{r})$, for which $x_{ia}^2 = 0.19$ and 0.09. Isosurfaces plotted here encapsulate 85% of the probability densities $|\psi(\mathbf{r})|^2$.

detachment densities, respectively. This connection does not seem to be widely appreciated.

In some cases the use of densities rather than orbitals may be more convenient, especially when several singular values are significant. That situation that is discussed in Section 3.4. On the other hand, the NTOs preserve phase information that is lost upon squaring the orbitals and that information may be useful in some situations, *e.g.*, to distinguish $n\pi^*$ from $\pi\pi^*$ in cases of significant orbital mixing, or to reveal the $\pi \to \pi^*$ in a case with complicated nodal structure, as in the example of Fig. 3b.

For a very different example, we turn to x-ray spectroscopy at the titanium K-edge. Calculations on a $Ti_{16}O_{32}H_2$ cluster (Fig. 5) were performed at the PBE0/def2-ma-SVP level,[15] where the basis set is "minimally augmented" (denoted "ma"),[159] which is intended to describe any nascent band structure. The K-edge consists of transitions from Ti(1s) to valence virtual orbitals at almost 5,000 eV, and to access core-level excitations these calculations invoke the core/valence separation approximation.[160] That means omitting amplitudes x_{ia} unless ψ_i corresponds to a core orbital of interest, meaning Ti(1s) in the present example, while retaining the full virtual space. The principal particle NTO in this example exhibits essentially just one nonzero singular value ($\lambda_1^2 = 1.00$) and is depicted in Fig. 5a, where its Ti(3d) character is evident along with some admixture of O(2p). The hole NTO is not shown but corresponds to the Ti(1s) on a nearby atom, meaning that the asymmetry of the cluster has localized this Ti(1s) → Ti(3d) pre-edge feature to one end of the cluster.

In the canonical MO basis, the same transition is completely scrambled and essentially uninterpretable. Two of the relevant canonical virtual orbitals are shown in Figs. 5b and 5c but there are 17 distinct amplitudes with $|x_{ia}| \gtrsim 0.1$, the largest of which contributes only 19% of the norm of the transition eigenvector, and all 17 of which collectively contribute only 85%.

Note that Fig. 5 indicates the fraction of $|\psi(\mathbf{r})|^2$ that is encapsulated within each depicted isosurface, which is necessary in order to make meaningful side-by-side comparisons of orbital localization or size. Isoprobability surfaces can be readily computed,[161] given volumetric data on a grid (*e.g.*, in the format of a "cube" file),[106] and this functionality is available in some visualization programs.[162] Orbitals should not be compared side-by-side unless one is plotting a consistent fraction of $|\psi(\mathbf{r})|^2$, lest one given
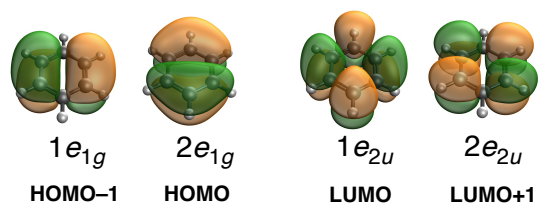
Fig. 6 Frontier MOs for benzene (B3LYP/6-31G* level). The two occupied orbitals are degenerate, as are the two virtual orbitals.

a false impression of relative size.

The example in Fig. 5 shows that $\mathbf{x}$ may be characterized in some cases by just one singular value, with $\lambda_1^2 \approx 1$. In such cases, the principal NTO pair can be used to distill the picture into one that involves just one occupied and one virtual orbital, without loss of information. Such is also the case for the $S_0 \rightarrow S_2$ transition of the fluoronone-terminated polyfluorene that is shown in Fig. 3, for which $\lambda_1^2 = 0.96$. The NTO basis presents a simple picture (Fig. 3b), but in the canonical MO basis there are four different amplitudes x_{ia} contribute significantly to the same transition (Fig. 3a). The latter are highly delocalized in the occupied space and form a localized hole only upon coherent superposition, whereas the localization is immediately evident in the NTO basis. Higher-energy transitions of polyfluorenes do involve a larger number of significant NTO pairs, [136] which is not unusual. Since NTOs are the optimal particle/hole basis, the presence of more than one significant singular value λ_i is a signature of un-resolvable multideterminant character in the excited-state wave function, which cannot be rotated away by unitary change of basis. [18,19,112] The next section considers this in more detail.

3.4 Static correlation

The presence of more than one significant singular value (λ_i) in the SVD of $\mathbf{x}$ can be driven by symmetry-induced orbital degeneracies. Such is the case for benzene, whose frontier MOs (Fig. 6) consist of a pair of degenerate e_{1g} orbitals (HOMO and HOMO -1) along with a pair of degenerate e_{2u} orbitals (LUMO and LUMO $+1$). In small basis sets, there is essentially no difference between the canonical MOs and the NTOs for the low-lying excited states and they can be used interchangeably in the following discussion. Four singly-excited determinants can be constructed from the aforementioned frontier MOs, and together these make up the first four singlet excited states of benzene. These states are:

$$|S_1(B_{2u})\rangle = \left(\left|\Psi_{1e_{1g}}^{1e_{2u}}\right\rangle + \left|\Psi_{2e_{1g}}^{2e_{2u}}\right\rangle\right)/\sqrt{2} \qquad (3.7a)$$

$$|S_2(B_{1u})\rangle = \left(\left|\Psi_{1e_{1g}}^{1e_{2u}}\right\rangle - \left|\Psi_{2e_{1g}}^{2e_{2u}}\right\rangle\right)/\sqrt{2} \qquad (3.7b)$$

$$|S_3(E_{1u})\rangle = \left(\left|\Psi_{2e_{1g}}^{1e_{2u}}\right\rangle + \left|\Psi_{1e_{1g}}^{2e_{2u}}\right\rangle\right)/\sqrt{2} \qquad (3.7c)$$

$$|S_3{}'(E_{1u})\rangle = \left(\left|\Psi_{2e_{1g}}^{1e_{2u}}\right\rangle - \left|\Psi_{1e_{1g}}^{2e_{2u}}\right\rangle\right)/\sqrt{2} . \qquad (3.7d)$$

States S_1 and S_2 are optically dark in one-photon spectroscopy but S_3 is dipole-allowed and doubly degenerate. [164] Calculations

at the TD-B3LYP/6-31G* level conform to this simple four-orbital model with $> 99\%$ fidelity. Although the TD-DFT results might at first seem complicated, in the sense that there is no excited state that is primarily HOMO($2e_{1g}$) $\rightarrow$ LUMO($1e_{2u}$) in nature, there is actually little else that these states could have been, given the symmetry of the system. Symmetry here is a parlor trick that makes the situation seem complicated by introducing unresolvable multiconfigurational character, wherein a minimum of four orbitals and two determinants is required to describe the low-lying excited states, even within a single-excitation theory such as CIS or TD-DFT.

A more interesting example, which is not driven by symmetry, is the keto-defect polyfluorene oligomer whose $S_0 \rightarrow S_2$ transition was considered in Figs. 2 and 3 and whose $S_0 \rightarrow S_3$ transition is depicted in Fig. 7a. There is interest in these molecules for fabrication of organic light-emitting devices, [165–170] as this is one of the few classes of materials that can span the whole range of visible wavelengths at low operating voltage, [165] and with good emission properties for blue light. [166] These properties arise from highly delocalized excited states of the π system that may exhibit large polarizabilities and hyperpolarizabilities, giving rise to non-linear optical properties. [171] In the present example, such states are accessed at higher excitation energies such as $\omega = 4.5$ eV for $S_0 \rightarrow S_3$. The oscillator strength for this delocalized transition ($f = 4.5$) is about 25 times greater than that of the defect-localized $S_0 \rightarrow S_2$ excitation.

For $S_0 \rightarrow S_3$, even the principal NTOs are delocalized over the length of the molecule (Fig. 7a), meaning that this is genuine delocalization and is not an artifact of the representation. The principal NTO pair accounts for only 67% of the transition density while a second NTO pair contributes another 20%. Irreducible mixing of more than one NTO pair is a signature of static correlation in the excited state. [18,19,112] (Note that there is no contradiction with the use of a single-determinant formalism for the ground state, because the CIS wave function *ansatz* is multideterminantal.) From another point of view, the presence of more than one significant singular value in the TDM indicates that the natural orbitals of the ground state differ significantly from those in the excited state. [112] A close examination of the NTOs in Fig. 7a reveals that $\psi_1^{\text{hole}}(\mathbf{r})$ and $\psi_2^{\text{hole}}(\mathbf{r})$ are out of phase with one another at the left end of the molecule, but evolve across its length such that they are in phase on the right terminus of the molecule. The same is true of $\psi_1^{\text{elec}}(\mathbf{r})$ and $\psi_2^{\text{elec}}(\mathbf{r})$, which suggests that the excited state in question can only properly be described using a minimum of two determinants. This would not be obvious from attachment/detachment density analysis.

Formal analysis suggests that static correlation, manifesting as more than one significant NTO pair, may occur in cases where a molecule consists of two or more weakly-interacting chromophores, [172] even if these chromophores are but different chemical moieties within the same molecule. An example is the molecule shown in Fig. 7b that consists of three identical ligands connected to a central 1,3,5-triazene moiety in a propeller motif, wherein each ligand may be considered a distinct chromophore. (This and other triazene derivatives have been investigated [145] in the context of optoelectronic applications such as triplet-triplet
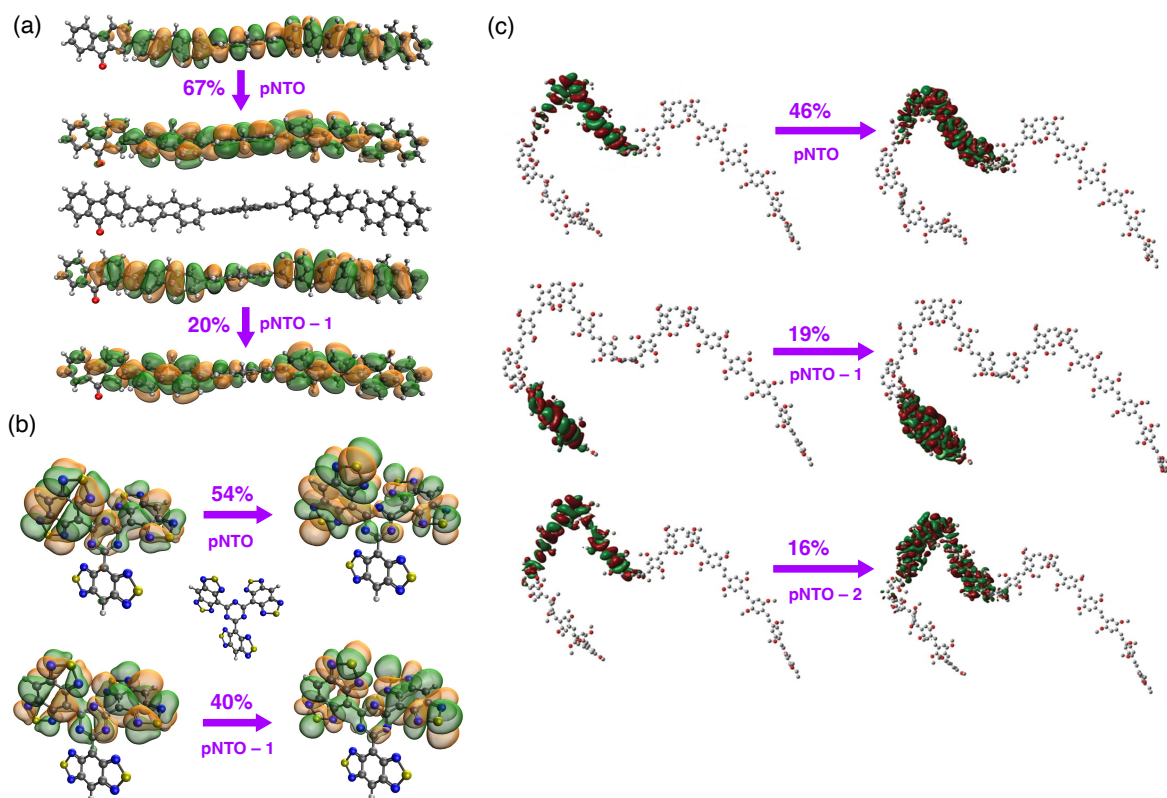
Fig. 7 NTOs for transitions that exhibit significant static correlation in the excited state: (a) $S_0 \rightarrow S_3$ excitation ($\omega = 4.5$ eV, $f = 4.5$) of a five-unit polyfluorene polymer with a keto defect (as in Figs. 2 and 3), computed using TD-DFT/TDA at the CAM-B3LYP/3-21G* level; (b) $S_0 \rightarrow S_1$ excitation ($\omega = 2.8$ eV, $f = 0.4$) of a 1,3,5-triazene derivative,[145] computed at the TD-ωB97X-D/TDA/6-31+G* level; and (c) $S_0 \rightarrow S_2$ excitation of a 20-unit MEH-PPV polymer, computed at the TD-ωB97X-D/6-31G* level. Panel (c) is adapted from Ref. 163; copyright 2014 American Chemical Society.

annihilation and TADF.[173–177]) Canonical MOs for this molecule are not shown but are mostly delocalized over all three ligands, nevertheless the NTOs for the $S_0 \rightarrow S_1$ transition are delocalized over just two of the three ligands (Fig. 7b). Although this could be inferred also from the particle and hole densities, what those densities cannot reveal is the role of static correlation: this excited state is evidently an irreducible combination of *two* particle/hole pairs. Another example with multiple chromophores within the same molecule is the poly[2-methoxy-5-(2-ethylhexyl-oxy)-1,4-phenylene vinylene] (MEH-PPV) polymer that is shown in Fig. 7c.[163] Here, breaks in the conjugation divide the polymer into several effective intramolecular chromophores, yet electronic coupling between them is sufficient to maintain coherence of the exciton across these gaps in conjugation.

The close connection between significant NTO pairs and static correlation suggests that the NTOs can be used to infer electron configurations, and in particular to detect changes in electron configuration across a potential energy surface. (In fact, a more descriptive name for the NTOs might be *natural electron configurations*.[179]) Consider the electrocylic ring-opening of oxirane (C_2H_4O), a prototypical reaction for which the Woodward-Hoffman rules were developed.[180,181] Potential energy curves along the C–C–O bond angle of the ring are plotted in Fig. 8 and isosurface plots of the principal NTO pair are provided at various points, for transitions to S_2 and S_3.[178] The reaction involves a

conical intersection between these two excited states, at an angle $\theta_{CCO} \approx 62°$, and the nonadiabatic transition that occurs there is accompanied by an abrupt switch in the qualitative nature of $\psi_1^{elec}(\mathbf{r})$, as shown in Fig. 8a. On the other hand, $\psi_1^{hole}(\mathbf{r})$ remains qualitatively consistent as the system passes through the intersection. By means of these NTOs, one may assign the diabatic character of either state: for $\theta_{CCO} < 62°$, the S_2 state is $n \rightarrow \sigma^*$ and the S_3 state is $n \rightarrow 3p_z$, whereas this character is reversed for $\theta_{CCO} > 62°$. Away from any near-degeneracy between Born-Oppenheimer potential surfaces, no such abrupt change is seen in the nature of the dominant NTOs, as illustrated in Fig. 8b.

4 Atomic partitions

Orbitals and densities introduced above provide convenient tools to visualize excited states in real space. The present section describes tools that attempt to quantify charge rearrangement in $\Delta\rho(\mathbf{r})$ by partitioning the density change into atomic contributions.

4.1 Mulliken analysis

Consider the ^{1}CT state of *p*-nitroaniline whose dipole moment change is listed in Table 1. Although the HOMO is nominally located on the amino group and the LUMO on the nitro group, both orbitals extend over a significant portion of this small molecule, thus the CT character of the state in question may not be obvious
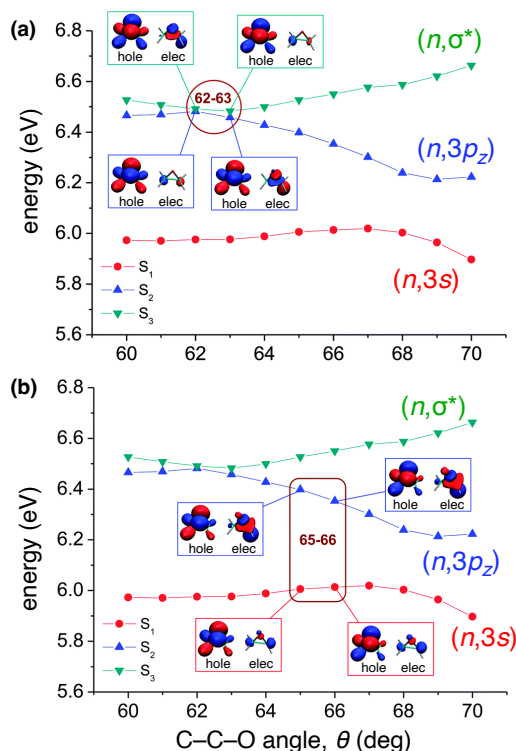
Fig. 8 Energy profiles along the electrocyclic ring-opening coordinate of oxirane (CH_2CH_2O), illustrating changes in the dominant NTO pairs at different points along the reaction coordinate. (a) Near the S_2/S_3 intersection at $\theta = 62°$, the hole remains consistent on both states as the system passes through the conical intersection, whereas the excited electron switches its character abruptly, from $3p_z$ to σ^*. (b) Where the electronic states are well-separated (*e.g.*, for $\theta = 65°$), the dominant NTOs remain qualitatively consistent as the system moves along the potential surface. Adapted from Ref. 178.

from the MOs. A Mulliken-style[182–184] partition of $\Delta\mathbf{P}^{\mathrm{elec}}$ and $\Delta\mathbf{P}^{\mathrm{hole}}$ might help to quantify the nature and extent of the charge rearrangement. In this approach, the charge that is transferred to atom A by electronic excitation is defined as

$$\Delta q_A^{\mathrm{elec}} = \sum_{\mu \in A} (\mathbf{S}\Delta\mathbf{P}^{\mathrm{elec}})_{\mu\mu} , \qquad (4.1)$$

where $\mathbf{S}$ is the atomic orbital (AO) overlap matrix. Simultaneously, atom A may lose some charge if it contributes to the hole, which may be quantified as

$$\Delta q_A^{\mathrm{hole}} = \sum_{\mu \in A} (\mathbf{S}\Delta\mathbf{P}^{\mathrm{hole}})_{\mu\mu} . \qquad (4.2)$$

Other common atomic partitions of a density matrix can be applied equally well, to obtain Löwdin charges rather than Mulliken charges,[105] for example. These decompositions are subject to the same variability with respect to the choice of AO basis set that characterizes ground-state Mulliken or Löwdin atomic charges, and are intended only to aid qualitative understanding. Charges derived from the molecular electrostatic potential[185] are much more reliable when it comes to reproducing electrostatic properties of excited states,[24] such as dipole moments, while Hirshfeld charges have been recommended for tracking photochemical

changes in electronic structure.[186]

4.2 Charge-transfer numbers

A different sort of atomic partition are the *CT numbers* that were first suggested by Luzanov and co-workers.[72,121,122,187–189] Like the difference charges $\Delta q_A^{\mathrm{elec}}$ and $\Delta q_A^{\mathrm{hole}}$, these quantities attempt to identify and quantify charge flow upon electronic excitation, based on atomic indices. For atoms or groups of atoms A and B, one might intuitively define an $A \to B$ charge transfer number according to[72,189]

$$l_{A \to B} = \sum_{\mu \in A} \sum_{\nu \in B} (x_{\mu\nu}^2 + y_{\mu\nu}^2) \qquad (4.3)$$

where

$$x_{\mu\nu} = \sum_{ia} c_{\mu i} x_{ia} c_{\nu a} \qquad (4.4)$$

is a transition amplitude expressed in the AO basis.[189] (The quantity $y_{\mu\nu}$ is defined analogously and $x_{\mu\nu}$ is sometimes called a pseudo-density.[190,191]) The idea behind eqn. (4.3) is that squared amplitudes $x_{\mu\nu}^2$ and $y_{\mu\nu}^2$ are associated with probabilities for transfer of charge from $\mu \in A$ to $\nu \in B$. However, the formula in eqn. (4.3) accounts neither for the normalization condition in eqn. (2.4), nor for the fact that the AOs are non-orthogonal. This may not be an issue when $l_{A \to B}$ is used to analyze semi-empirical calculations,[188,192–198] where the inherent minimal basis might be assumed to be orthonormal, but the same formula has been put forward for all-electron TD-DFT calculations in arbitrary basis sets.[72,189] Normalization could be enforced in a straightforward fashion,[199] defining

$$\tilde{l}_{A \to B} = \frac{l_{A \to B}}{\sum_{\lambda\sigma}(x_{\lambda\sigma}^2 + y_{\lambda\sigma}^2)} . \qquad (4.5)$$

Failure to account for the AO overlap matrix, however, leads to significant discrepancies in CT numbers computed in small versus large basis sets.[199]

For this reason, an alternative definition due to Plasser *et al.* is preferable,[18,200] as it accounts for non-orthogonality of the AO basis functions. This definition starts from the normalization condition

$$\int |T(\mathbf{r}, \mathbf{r}')|^2 d\mathbf{r}\, d\mathbf{r}' = 1 . \qquad (4.6)$$

Rewriting this in terms of $\mathbf{S}\Delta\mathbf{P}$, as in eqns. (4.1) and (4.2), suggests an atomic partition analogous to Mayer's bond-order matrix, $\mathbf{M}$.[201,202] For a closed-shell system, that quantity has matrix elements

$$M_{AB} = \sum_{\mu \in A} \sum_{\nu \in B} (\mathbf{PS})_{\mu\nu}(\mathbf{SP})_{\mu\nu} \qquad (4.7)$$

and thereby partitions $(\mathbf{SP})_{\mu\nu}$ into contributions $\mu \in A$ and $\nu \in B$. A matrix $\Delta\mathbf{M}$, representing changes in bond orders, can be obtained by swapping $\mathbf{S}\Delta\mathbf{P}$ for $\mathbf{SP}$ in eqn. (4.7):

$$(\Delta M)_{AB} = \sum_{\mu \in A} \sum_{\nu \in B} [(\Delta\mathbf{P})\mathbf{S}]_{\mu\nu}[\mathbf{S}(\Delta\mathbf{P})]_{\mu\nu} . \qquad (4.8)$$

The quantity ΔM_{AB} can then be taken as an alternative definition of a CT number,[200] a convention that has since been adopted

by others.[199,203–205] Alternatively, one might exploit trace invariance in $\text{tr}(\Delta\mathbf{M}) = \sum_{A,B}(\Delta M)_{AB}$ to partition the summand in eqn. (4.8) in the spirit of a symmetric (Löwdin) orthogonalization of $\Delta\mathbf{P}$.[105,206–208] This means two factors of $\mathbf{S}^{1/2}(\Delta\mathbf{P})\mathbf{S}^{1/2}$ as opposed to the separate factors of $(\Delta\mathbf{P})\mathbf{S}$ and $\mathbf{S}(\Delta\mathbf{P})$ that appear in eqn. (4.8).[27] This leads to a definition

$$\Omega_{A\to B} = \sum_{\mu\in A}\sum_{\nu\in B}[\mathbf{S}^{1/2}(\Delta\mathbf{P})\mathbf{S}^{1/2}]^2_{\mu\nu} \qquad (4.9)$$

to quantify the flow of charge from A to B, which amounts to a Löwdin-style partition of $\Delta\mathbf{P}$.[27] The quantity $\Omega_{A\to B}$ is a CT index in the spirit of $l_{A\to B}$ but corrected to take proper account of the non-orthogonal AO basis set. A Mulliken-style partition has also been formulated,[18] in the spirit of eqn. (4.8), however Löwdin populations are generally more stable and free of negative population artifacts.[27,184] That said, the value of $\Omega_{A\to B}$ certainly depends on the choice of AO basis set, as does any Löwdin population analysis.[184]

The method based on eqn. (4.9) has been called *fragment transition density analysis*,[199,203,209] because in the case of a correlated wave function one could imagine using the TDM in place of $\Delta\mathbf{P}$. For TD-DFT there is no distinction, although one could substitute $\Delta\mathbf{P}_{\text{rlx}}$ in place of $\Delta\mathbf{P}$, thereby using the relaxed density to understand charge flow. This is likely the better approach for analyzing CT states, for reasons discussed in Section 2.3.

The CT indices $\Omega_{A\to B}$ satisfy the normalization condition

$$\sum_{A,B}\Omega_{A\to B} = 1 \qquad (4.10)$$

for single-excitation wave functions. (The normalization condition is more complicated for other types of wave functions.[18]) An expression analogous to eqn. (4.10) has been suggested for $l_{A\to B}$,[189] yet this claim seems suspicious for all-electron TD-DFT calculations in non-orthogonal basis sets. Several other concepts introduced by Luzanov *et al.*[72,189] in the context of the indices $l_{A\to B}$ would seem to be rigorously valid only when the alternative definition $\Omega_{A\to B}$ is used instead. These include a *gross excitation localization index* (GLI),[72,189]

$$\text{GLI}_A = \Omega_{A\to A} + \text{CT}_A \qquad (4.11)$$

where

$$\text{CT}_A = \frac{1}{2}\sum_{B\neq A}(\Omega_{A\to B} + \Omega_{B\to A}) \, . \qquad (4.12)$$

The quantity CT_A is a measure of the charge that is shifted around in ways that involve atom A. It follows that

$$\sum_A \text{GLI}_A = 1 \, , \qquad (4.13)$$

which suggests that GLI_A provides an atomic or functional group partition of the excited electron. Along similar lines, it is possible to use the quantities $\Omega_{A\to B}$ to define the size of an exciton, although we postpone that discussion until Section 4.5. The CT character associated with atom A can be quantified using

$$N_{\text{CT}} = \sum_A \text{CT}_A \, , \qquad (4.14)$$

which measures the total CT character associated with A. The net charge transferred from A to B is

$$\Delta q_{A\to B} = \Omega_{A\to B} - \Omega_{B\to A} \, . \qquad (4.15)$$

4.3 Example: DMABN molecule

Mai *et al.*[27] provide examples illustrating the use of CT numbers $\Omega_{A\to B}$ in complicated cases of photochemical reactions involving transition metal complexes. Here, we consider a relatively simple example, 4-(dimethylamino)benzonitrile (DMABN), which has something of a history in TD-DFT. Its spectroscopy consists of dipole-allowed ultraviolet transitions to a pair of states known as ^1L_a and ^1L_b,[210–212] in a notation that comes from Platt's free-electron model.[213] (This notation is most often encountered in the spectroscopy of polycyclic aromatic hydrocarbons, PAHs.[21,214–220]) Setting aside detailed symmetry considerations, these two states have roughly perpendicular transition moments, along axes "a" and "b". The $S_0\to {}^1L_a$ transition is primarily a HOMO $\to$ LUMO excitation, with significant ionic character in PAHs, while $S_0\to {}^1L_b$ is a mixture of $(\text{HOMO}-1)\to\text{LUMO}$ and HOMO $\to (\text{LUMO}+1)$.[221] TD-DFT calculations sometimes afford an unbalanced treatment of these two states,[220–223] which are quite close in energy in the case of DMABN.[224]

The DMABN molecule is a canonical example of the phenomenon of *dual fluorescence*, or the appearance of two fluorescence bands whose intensity ratio is highly sensitive to solvent polarity.[210,225–227] Other donor–π–acceptor (or "push-pull") systems also exhibit this behavior,[228–230] and examples such as push-pull porphyrins and thiophene-based push-pull polymers have been widely studied as potential photosensitizers for solar cells.[231–238] Often, TD-DFT calculations have been used in an attempt to establish design principles.[239–243] Other categories of push-pull systems may be useful as dopants to produce devices with novel optoelectronic properties, including photoswitchable molecules,[244] and molecules that exhibit TADF without the use of heavy metals.[245–247]

Dual fluorescence represents an exception to Kasha's rule,[248–251] which states that emission typically occurs in a single band originating from the lowest excited state, insofar as radiationless internal conversion from higher-lying excited states is usually rapid and efficient. The dependence on solvent polarity has long been been interpreted in terms of excited-state dynamics that access a twisted intramolecular CT (TICT) state, characterized by rotation of the –N(CH$_3$)$_2$ group out of the phenyl plane.[210,225,252–260] In this picture, the TICT state is stabilized in polar solvents, relative to the "locally excited" (LE) state, which has $^1\pi\pi^*$ character, and is the origin of the longer-wavelength fluorescence band. This interpretation has been questioned, however, in both DMABN[261–268] and similar donor–π–acceptor systems.[269–272]

What is not in dispute is that the S_1 and S_2 states of DMABN exhibit different degrees of CT upon vertical excitation. In the gas phase, S_1 is the LE state and S_2 is the CT state, as evidenced by a dipole moment that is ≈ 6 D larger in S_2 than S_1, even while the S_1 dipole moment is ≈ 3 D larger than that of S_0.[224] This interpretation is furthered by examining CT numbers and GLIs for
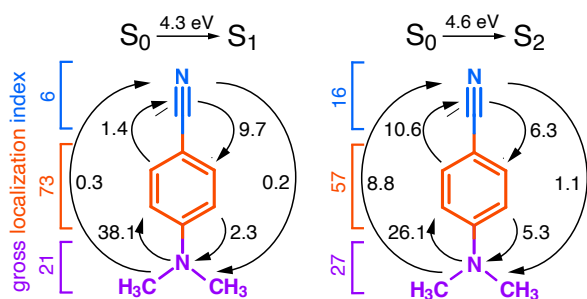
Fig. 9 Analysis of intramolecular charge rearrangement for excitation to the S_1 and S_2 states of DMABN, using color-coded fragments representing the cyano, phenyl, and amino moieties. CT numbers $\tilde{l}_{A \to B}$ for selected atoms (given here as percentages) are shown in black, at the arrows, and gross excitation localization indices GLI_A (also as percentages) are shown at the brackets. Calculations were performed at the TD-B3LYP/aug-cc-pVDZ level. Adapted from Ref. 72; copyright 2010 John Wiley and Sons.
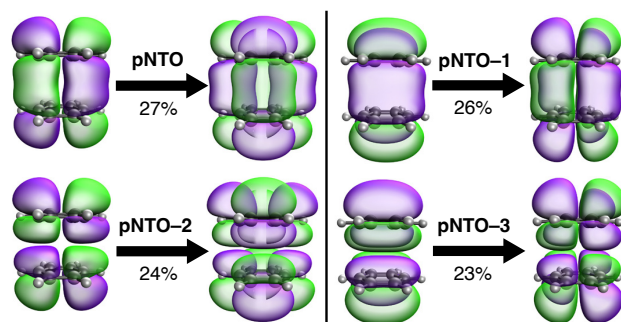

Fig. 10 Principal NTO pairs pairs for the lowest dipole-allowed FE state of the benzene dimer, in a cofacial D_{6h} arrangement. Calculations were performed at the TD-DFT/TDA level using CAM-B3LYP/6-31G* and these isosurfaces contain 80% of the orbital densities.

both states, which are provided in Fig. 9 based on Luzanov's definition ($l_{A \to B}$), normalized as percentages to sidestep issues with the normalization of eqn. (4.3). These quantities suggest that the $S_0 \to S_1$ transition is characterized by a single large CT number corresponding to electron transfer from the amino lone pair into the phenyl ring, yet the GLI analysis suggests that 73% of the excited electron is localized on the phenyl ring, consistent with the idea that S_1 is the $\pi\pi^*$ state. For the S_2 state, the CT numbers provide clear evidence of amino $\to$ phenyl $\to$ cyano electron transfer, with smaller fractions of the excited electron localized on the amino and phenyl groups as compared to S_1, and a larger fraction transferred to the cyano moiety.

4.4 Frenkel excitons and charge-resonance states

New forms of complexity emerge in systems having multiple electronic chromophores that are identical or near-identical and whose vertical excitation energies are quasi-degenerate. If the electronic coupling between chromophores is sufficiently strong, then the monomer excitations will mix and the excited-state wave function for the aggregate system will be delocalized across more than one chromophore. [273–276] Consider the case of two identical monomers in a high-symmetry arrangement, such as a cofacial benzene dimer with D_{6h} symmetry, for which the pNTOs are illustrated in Fig. 10. As discussed in Section 3.4, a minimum of four Slater determinants is required to describe the frontier excitations of the benzene monomer [eqn. (3.7)], and the same is true for the dimer but the relevant pNTOs are delocalized over both monomers.

Collective excitations of electronically coupled chromophores can be conceptualized as linear combinations of basis states $|\Psi_1^*\Psi_2\rangle$ and $|\Psi_1\Psi_2^*\rangle$ in which one monomer or the other is excited. These are the *Frenkel exciton* (FE) states, as in the classic case of H- and J-aggregates of PAHs. [277] In a high-symmetry system such as the benzene dimer, the mixing coefficients are equal:

$$\left|\Psi_\pm^{FE}\right\rangle = \frac{1}{\sqrt{2}}\left(\left|\Psi_1^*\Psi_2\right\rangle \pm \left|\Psi_1\Psi_2^*\right\rangle\right). \qquad (4.16)$$
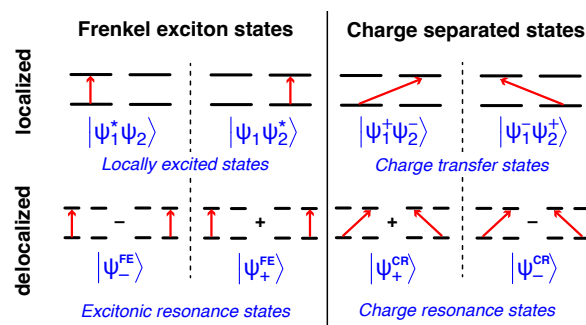
Fig. 11 Different representations of FE (or excitonic resonance) excited states versus CT excited states, in a symmetric dimer whose ground-state wave function is denoted $|\Psi_1\Psi_2\rangle$. Adapted from Ref. 200; copyright 2012 American Chemical Society.

In lower-symmetry examples, the isolated-monomer excitations may not be exactly degenerate. Mixing may still occur but the coefficients need not be equal, so a more general expression is

$$\left|\Psi^{FE}\right\rangle = c_1\left|\Psi_1^*\Psi_2\right\rangle + c_2\left|\Psi_1\Psi_2^*\right\rangle \qquad (4.17)$$

for mixing coefficients c_1 and c_2.

When the chromophores are at close-contact (van der Waals) separation, there is also the possibility of intermolecular CT, which can be represented using basis states $|\Psi_1^+\Psi_2^-\rangle$ and/or $|\Psi_1^-\Psi_2^+\rangle$. For highly symmetric systems, these these forward and backward CT states may be degenerate, leading to the formation *charge-resonance* (CR) states,

$$\left|\Psi_\pm^{CR}\right\rangle = \frac{1}{\sqrt{2}}\left(\left|\Psi_1^+\Psi_2^-\right\rangle \pm \left|\Psi_1^-\Psi_2^+\right\rangle\right), \qquad (4.18)$$

which are characterized by equal amounts of forward and backward CT. [46,274,278] If the electron-transfer process is similar in energy to the $S_0 \to S_1$ monomer excitation energy, then either CT excitons or else localized CT states may further mix with FE states. This type of mixing has been widely discussed in the theory of excimers and photoluminescence. [273,274,279–281] Various scenarios are illustrated schematically in Fig. 11.

The states depicted in Fig. 11 form an idealized basis to guide one's thinking about delocalization and excitation energy transfer in multichromophore systems. In the real world, these basis

Table 2 Descriptors for the excimer states of a symmetric dimer.[a]

State[b]	$\Delta q_{1\to 2}$[c]	N_{CT}[d]	$PR_{e\text{-}h}$[e]	$\boldsymbol{\Omega}$[f]
$\|\Psi_1^*\Psi_2\rangle$	0	0	1	$\begin{pmatrix} 0 & 0 \\ 1 & 0 \end{pmatrix}$
$\|\Psi_1\Psi_2^*\rangle$	0	0	1	$\begin{pmatrix} 0 & 1 \\ 0 & 0 \end{pmatrix}$
$\|\Psi_1^-\Psi_2^+\rangle$	-1	1	1	$\begin{pmatrix} 1 & 0 \\ 0 & 0 \end{pmatrix}$
$\|\Psi_1^+\Psi_2^-\rangle$	1	1	1	$\begin{pmatrix} 0 & 0 \\ 0 & 1 \end{pmatrix}$
$\|\Psi_-^{FE}\rangle$	0	0	2	$\begin{pmatrix} 0 & 0.5 \\ 0.5 & 0 \end{pmatrix}$
$\|\Psi_+^{FE}\rangle$	0	0	2	$\begin{pmatrix} 0 & 0.5 \\ 0.5 & 0 \end{pmatrix}$
$\|\Psi_+^{CR}\rangle$	0	1	2	$\begin{pmatrix} 0.5 & 0 \\ 0 & 0.5 \end{pmatrix}$
$\|\Psi_-^{CR}\rangle$	0	1	2	$\begin{pmatrix} 0.5 & 0 \\ 0 & 0.5 \end{pmatrix}$

[a] Adapted in part from Ref. 200; copyright 2012 American Chemical Society. [b] See Fig. 11. [c] Eqn. (4.15). [d] Eqn. (4.14). [e] Eqn. (4.25). [f] Eqn. (4.19).

states interact and mix, so the real picture may be more muddled. An important case where both FE and CT states are in play are the π-stacked nucleobase dimers.[29,31,282–284] The FE states are optically allowed from the ground state, whereas the CT states are optically dark, but ultrafast spectroscopy provides evidence for interplay between them.[285–290] Low-lying excited states of tetracene and pentacene also exhibit this type of FE/CT mixing,[46,291–295] which is relevant to the singlet fission (SF) process.[46,296–300] In the perylene diimide dimer, which is a common molecular scaffold for SF,[301,302] there has been much discussion of solvent-induced symmetry breaking that can convert CR states into localized CT states.[303,304] Within a quantum chemistry calculation, even low-polarity dielectric boundary conditions ($\varepsilon = 3$, as in organic thin films) can provide sufficient polarization to break the electronic symmetry and localize the CT states.[278]

In cases where mixing is significant, it can be challenging to develop a conceptual picture based on detailed calculations, even in a dimer system. Because each of the four wave functions $\|\Psi_\pm^{FE}\rangle$ and $\|\Psi_\pm^{CR}\rangle$ is delocalized over both chromophores, FE states cannot be distinguished from CR states on the basis of particle/hole or attachment/detachment densities.[122] The key to differentiating them is to recognize that the CT indices ($\Omega_{A\to B}$ or $l_{A\to B}$) contain information about correlations between particle and hole that are averaged away in the densities $\Delta\rho_{elec}$ and $\Delta\rho_{hole}$. This has been analyzed in terms of the cumulant of the two-electron density matrix,[305] but a more straightforward analysis is to use a 2×2 matrix comprised of the quantities $\Omega_{A\to B}$ or $l_{A\to B}$, in which fragments A and B represent the two monomers.[200]

The matrix $\boldsymbol{\Omega}$ comprised of the CT numbers $\Omega_{A\to B}$ is presented in Table 2 for the delocalized states $\|\Psi_\pm^{FE}\rangle$ and $\|\Psi_\pm^{CR}\rangle$ that appear

Fig. 11, along with the four basis states that contribute to them. We use a slightly unusual indexing convention for $\boldsymbol{\Omega}$, which is

$$\boldsymbol{\Omega} = \begin{pmatrix} \Omega_{2\to 1} & \Omega_{2\to 2} \\ \Omega_{1\to 1} & \Omega_{1\to 2} \end{pmatrix} \tag{4.19}$$

for the 2×2 case spanned by monomers 1 and 2, as in Table 2. This differs from the usual matrix indexing convention, and from the $\boldsymbol{\Omega}$ matrices defined by Plasser and Lischka,[200] but is consistent with real-space plots of $T(\mathbf{r}_{hole}, \mathbf{r}_{elec})$ that appear in Section 5. In those plots, the particle and hole coordinates $\mathbf{r}_{elec}$ and $\mathbf{r}_{hole}$ have their coordinate origins in the lower left, per usual convention, so it makes sense to put the $\Omega_{1\to 1}$ matrix element in the lower left of $\boldsymbol{\Omega}$, since this matrix presents a discretized version of the same information that is conveyed by $T(\mathbf{r}_{hole}, \mathbf{r}_{elec})$.

By means of the matrix $\boldsymbol{\Omega}$, the FE and CR states become easily distinguishable: matrix elements along the diagonal ($\Omega_{2\to 1}$ and $\Omega_{1\to 2}$) are associated with charge separation while the anti-diagonal direction ($\Omega_{1\to 1}$ and $\Omega_{2\to 2}$) is associated with charge-neutral excitations and thus FE states. Note that the full matrix $\boldsymbol{\Omega}$ is necessary in order to make these distinctions and the GLI in eqn. (4.11) is insufficient. The metric N_{CT} [eqn. (4.14)] differentiates charge-neutral excitations (both localized and delocalized) from charge-separated ones, and $\Delta q_{1\to 2}$ [eqn. (4.15)] establishes the direction of charge flow.

This analysis is idealized in the sense that it assumes orthonormal basis functions, and is intended to demonstrate simply that the aforementioned metrics are capable of distinguishing between delocalized states and thus providing information that $\Delta\rho_{elec}$ and $\Delta\rho_{hole}$ do not. (In real systems, a given excitation may exhibit both FE and CT character, as discussed above.) These metrics rely on our ability to assign amplitudes $x_{\mu\nu}$ to atoms and are thus susceptible to the same basis-set sensitivity that can be problematic for Mulliken or Löwdin charge analysis. That said, this type of analysis has been used in real calculations to classify the excited states of π-stacked dimers of naphthalene,[200] adenine,[200,283] and pyridine,[306] for example.

4.5 Participation ratio

Table 2 also introduces the *participation ratio* (PR) as a means to distinguish between localized and delocalized states. This is a measure of delocalization over sites that is used in a wide variety of contexts.[18,307–312] A generic definition is

$$PR = \frac{1}{\sum_{i=1}^n p_i^2} \tag{4.20}$$

where p_i is the probability of localization onto site i, for a system with n sites. In quantum mechanics, p_i is usually the square of some coefficient that expresses the wave function as a linear combination of localized basis functions that are assignable to sites, say,

$$\|\psi_k\rangle = \sum_{i=1}^n a_{ki} \|\phi_i\rangle . \tag{4.21}$$

The denominator in eqn. (4.20) then involves the fourth power of the amplitudes a_{ki},

$$\mathrm{PR}(\psi_k) = \frac{\left(\sum_{i=1}^n a_{ki}^2\right)^2}{\sum_{j=1}^n a_{kj}^4} . \qquad (4.22)$$

We assume normalized coefficients henceforth, in which case the numerator in this expression equals unity, as in eqn. (4.20). If $p_i = 1/n$, indicating equal probabilities for each site, then PR = n. In general, the PR may be interpreted as the number of sites over which the wave function delocalizes, and for that reason it has sometimes been called a *collectivity index*.[72]

The presence of a reciprocal in eqn. (4.20) seems to have led to some confusion, whereby this quantity is sometimes called the *inverse* participation ratio (IPR).[313–318] However, calling the quantity defined in eqn. (4.20) a PR is consistent with the earliest examples in the literature,[307–310] and perhaps more importantly it means that the PR increases (rather than decreases) as additional monomers participate in the excitation. With eqn. (4.20) taken to define the PR, then its inverse is

$$\mathrm{IPR} = \sum_{i=1}^n p_i^2 , \qquad (4.23)$$

meaning that IPR = $1/n$ if $p_i = 1/n$. That is consistent with the idea of the inverse (reciprocal) of participation by n chromophores, and also appears to be standard notation in the literature on localization phenomena.[309–311,319–322] However, both Mukamel and co-workers,[312–314] as well as Fleming and co-workers,[315,323] are inconsistent regarding whether eqn. (4.20) defines the PR or the IPR. In view of the arguments above, PR should be defined by eqn. (4.20) and its inverse, if needed, can be called 1/PR.

For TD-DFT, one might define separate PRs for the electron and the hole:[200]

$$\mathrm{PR}_{\mathrm{elec}} = \left[\sum_B \left(\sum_A \Omega_{A \to B}\right)^2\right]^{-1} \qquad (4.24a)$$

$$\mathrm{PR}_{\mathrm{hole}} = \left[\sum_A \left(\sum_B \Omega_{A \to B}\right)^2\right]^{-1} . \qquad (4.24b)$$

(Note carefully the order of the summation indices and the fact that $\mathbf{\Omega}$ is not symmetric. The quantities $\mathrm{PR}_{\mathrm{elec}}$ and $\mathrm{PR}_{\mathrm{hole}}$ are distinct.) Combining these two quantities affords a PR for the electron–hole pair:[200]

$$\mathrm{PR}_{\text{e-h}} = \frac{1}{2}(\mathrm{PR}_{\mathrm{elec}} + \mathrm{PR}_{\mathrm{hole}}) . \qquad (4.25)$$

Following appropriate coordinate transformations, each of these PRs involves a summation over $x_{\mu\nu}^4$, as in eqn. (4.22). In the idealized case of the states presented in Fig. 11, one finds that the four localized states are characterized by $\mathrm{PR}_{\text{e-h}} = 1$ and are thus distinguishable from the four delocalized states, for which $\mathrm{PR}_{\text{e-h}} = 2$. This is indicated in Table 2.

The quantities $\mathrm{PR}_{\mathrm{elec}}$ and $\mathrm{PR}_{\mathrm{hole}}$ measure the size of the exciton in terms of the coordinates of the electron ($\mathbf{r}_{\mathrm{elec}}$) or the hole ($\mathbf{r}_{\mathrm{hole}}$), respectively. Their average, $\mathrm{PR}_{\text{e-h}}$, is thus a measure
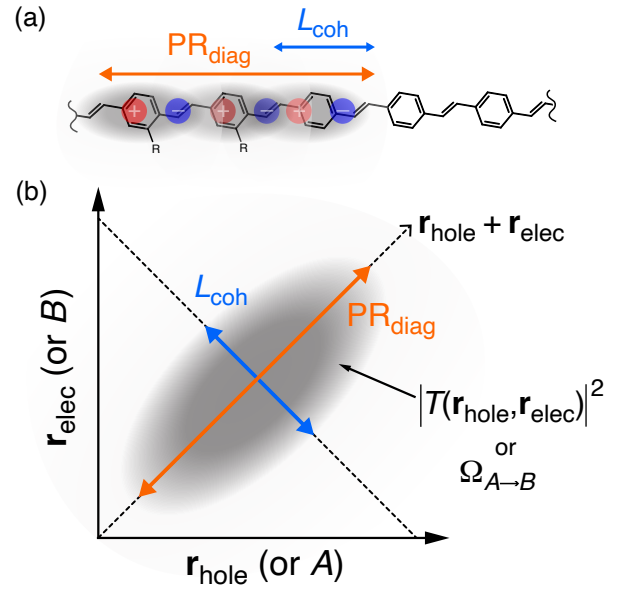

Fig. 12 Guide to interpreting $T(\mathbf{r}_{\mathrm{hole}}, \mathbf{r}_{\mathrm{elec}})$ as a two-dimensional probability distribution, or $\mathbf{\Omega}$ as a two-dimensional matrix, for a hypothetical excitation in a conjugated polymer. (a) Schematic illustrations of the coherence length L_{coh} [eqn. (4.26)], which measures electron–hole separation in the intracule coordinate $\mathbf{r}_{\mathrm{elec}} - \mathbf{r}_{\mathrm{hole}}$, along with the diagonal length $\mathrm{PR}_{\mathrm{diag}}$ that measures overall exciton size via the extracule coordinate $\mathbf{r}_{\mathrm{elec}} + \mathbf{r}_{\mathrm{hole}}$. The entire exciton should be construed as a superposition of electron–hole pairs, each of which has a characteristic separation L_{coh}, whereas the superposition extends over approximately $\mathrm{PR}_{\mathrm{diag}}$ distinct sites. (b) Schematic illustration of a two-dimensional probability distribution $|T(\mathbf{r}_{\mathrm{hole}}, \mathbf{r}_{\mathrm{elec}})|^2$. Heat maps of $\mathbf{\Omega}$ can be interpreted as two-dimensional plots with the same axes ($\mathbf{r}_{\mathrm{hole}}, \mathbf{r}_{\mathrm{elec}}$). In that case, distance is measured in units of atoms or functional groups (sites A in $\Omega_{A \to B}$), depending on how the molecule is partitioned. The overall size of the exciton is limited by the size of the molecule as an upper bound, and L_{coh} is then limited by $\mathrm{PR}_{\mathrm{diag}}$. This figure is based on a similar one in Ref. 312.

of exciton size along the extracule coordinate,[324] $\mathbf{r}_{\mathrm{elec}} + \mathbf{r}_{\mathrm{hole}}$. A complementary metric is the *coherence length* of the exciton (L_{coh}),[200,312] which measures exciton size in terms of the intracule coordinate,[324] $\mathbf{r}_{\mathrm{elec}} - \mathbf{r}_{\mathrm{hole}}$. The coherence length may be defined using CT indices according to[200]

$$L_{\mathrm{coh}} = \left[(\mathrm{PR}_{\text{e-h}}) \sum_{A,B} (\Omega_{A \to B})^2\right]^{-1} \qquad (4.26)$$

and a cartoon description for a conjugated polymer is provided in Fig. 12a. Note how off-diagonal elements of $\mathbf{\Omega}$ (or $\Delta\mathbf{P}$) characterize coherences between atoms or fragments in the electronic excitation. Here, "off-diagonal" means $\Omega_{A \to B}$ where $A \neq B$; consult the model $\mathbf{\Omega}$ matrices in Table 2 and beware of the unusual indexing convention introduced in eqn. (4.19). A value $L_{\mathrm{coh}} = 1$ indicates that there is no such contribution from $A \neq B$, which implies that the excitation is a superposition of localized excitations (a FE state), or that it is simply localized on a single site.[200]

The length scale over which a FE state is delocalized is measured in the extracule coordinate, and a sensible definition of a

Table 3 Excitation energies (ΔE), oscillator strengths (f), and various descriptors (PR$_{e\text{-h}}$, L_{coh}, PR$_{\text{NTO}}$, and $\boldsymbol{\Omega}$) for some singlet transitions S$_0 \to$ S$_n$ in (PV)$_6$Ph.[a]

	S$_1$ $1\,^1B_u$	S$_2$ $2\,^1A_g$	S$_3$ $2\,^1B_u$	S$_4$ $3\,^1A_g$	S$_5$ $4\,^1A_g$	S$_6$ $3\,^1B_u$
ΔE (eV)	3.15	3.56	4.00	4.22	4.39	4.47
f	5.66	0.00	0.61	0.00	0.00	0.02
PR$_{e\text{-h}}$[b]	5.53	6.32	6.69	5.14	6.30	3.80
L_{coh}[c]	3.90	3.38	3.03	4.98	3.04	2.20
PR$_{\text{NTO}}$[d]	1.59	2.14	2.99	2.39	4.00	4.16
$\boldsymbol{\Omega}$[e]						

[a] Calculations performed at the ADC(2) level and reprinted from Ref. 200; copyright 2012 American Chemical Society. [b] Eqn. (4.25). [c] Eqn. (4.26). [d] Eqn. (4.28). [e] $\Omega_{AB} = \Omega_{A \to B}$, using a monomer-based partition; see Eq. (4.19).

PR to describe this is[200]

$$\text{PR}_{\text{diag}} = \frac{(\sum_A \Omega_{A \to A})^2}{\sum_B (\Omega_{B \to B})^2} \, . \tag{4.27}$$

This has been called a "diagonal" PR,[200] or sometimes a diagonal length scale,[312] as indicated by the notation. However, the extracule coordinate lies along the *anti-diagonal* direction in a real-space representation of $T(\mathbf{r}_{\text{hole}}, \mathbf{r}_{\text{elec}})$; see Fig. 12b. The indexing convention for $\boldsymbol{\Omega}$ in eqn. (4.19) reflects the fact that this matrix is essentially a coarse-graining of $T(\mathbf{r}_{\text{hole}}, \mathbf{r}_{\text{elec}})$. Within this convention, the length scale PR$_{\text{diag}}$ appears along the anti-diagonal direction of $\boldsymbol{\Omega}$, so that a heat map of the latter will resemble $|T(\mathbf{r}_{\text{hole}}, \mathbf{r}_{\text{elec}})|^2$ in Fig. 12b.

For an example of the use of $\boldsymbol{\Omega}$ and other metrics introduced in this section, we turn to poly(*p*-phenylene vinylene) or PPV, which is the electroluminescent chromophore in one of the first organic light-emitting diodes fashioned from a polymeric material.[325–328] Excited states of a six-unit PPV polymer [(PV)$_6$Ph] are considered in Table 3.[200] Although these calculations were performed using a many-body wave function method, they are characterized in Table 3 using the descriptors introduced above, which are equally valid for TD-DFT. Indices A and B in these (PV)$_6$Ph examples correspond to PV monomer units and $\boldsymbol{\Omega}$ is depicted as a grayscale heat map in Table 3.

For the lowest few singlet excited states, including the S$_1$ bright state, PR$_{e\text{-h}}$ ranges from 3.8–6.7 with PR$_{e\text{-h}} > 5$ in all but one case. This indicates near-complete delocalization of the exciton over the molecule. The S$_1$, S$_2$, and S$_3$ states are characterized by zero, one, and two nodes along the extracule coordinate, respectively, and could be interpreted as sequential states belonging to a single exciton band, with particle-in-a-box character along the exciton center-of-mass coordinate. The S$_4$, S$_5$, and S$_6$ states (again with zero, one, and two nodes, respectively) constitute a second exciton band. This is consistent with the idea that the intracule and extracule coordinates $\mathbf{r}_{\text{elec}} \pm \mathbf{r}_{\text{hole}}$ sometimes behave as separable quasiparticle coordinates in conjugated polymers.[163,329] However, Plasser and Lischka question whether these should indeed be characterized as FE states, given their significant coherence lengths (*e.g.*, $L_{\text{coh}} = 3.9$ for S$_1$ and $L_{\text{coh}} = 5.0$ for S$_4$).[200] These values quantify the diagonal length scale in the $\boldsymbol{\Omega}$ heat

maps and can be interpreted as electron–hole separation, measured in units of PV monomers. The computed values suggest that the electron and hole are well separated, unlike the conventional FE picture of a tightly-bound electron and hole.

Evidence of static correlation in this PPV system can abe detected using the quantity

$$\text{PR}_{\text{NTO}} = \frac{1}{\sum_i \lambda_i^4} \, , \tag{4.28}$$

where the λ_i are the singular values associated with each NTO pair. The quantity PR$_{\text{NTO}}$ is a participation ratio in the NTO basis; *cf*. eqns. (4.20) and (4.22). For the six-unit polymer described in Table 3, the quantity PR$_{\text{NTO}}$ starts at a value of 1.6 for the S$_1$ state and increases monotonically as one moves up the excitation manifold, with PR$_{\text{NTO}} \approx 4$ for states S$_5$ and S$_6$. These two states are each characterized by an average of four significant particle/hole pairs, indicating significant static correlation.

The PR makes an appearance in certain analytic theories of exciton transport in organic photovoltaic materials.[316,317,330] For example, a simple analytic theory predicts that the effective Huang-Rys parameter (linear exciton–phonon coupling constant) should be $S(n) = S(1)/\text{PR}$ in a polymer with n repeat units, where $S(1)$ is the Huang-Rys parameter for the monomer unit.[316]

The PR is also used in studies of conjugated polymers to define an effective length scale for an exciton, which need not be the same as the conjugation length in the ground state. With this in mind, it is interesting to revisit the NTOs for MEH-PPV that are depicted in Fig. 7c, where three pairs of NTOs are needed to recover 81% of the transition density. These NTOs show that the excitation delocalizes around the bent portion of the molecule, suggesting that a purely geometric definition of broken conjugation is insufficient to understand exciton localization in this system, and similarly inadequate to define the effective size of the chromophore; other mechanisms such as dipole-dipole coupling and superexchange can drive delocalization even when geometric distortion leads to loss of conjugation.[163] With an excited-state wave function in hand, however, an effective chromophore size can be inferred by measuring the particle–hole separation for the exciton.[163] This is the anti-diagonal coordinate in the $\boldsymbol{\Omega}$ plots of Table 3, for a different PPV system. This analysis technique and other statistical measures of electron–hole correlation are described in the next section.

5 Exciton wave function

The concept of an "exciton" or bound particle/hole pair is ubiquitous in solid-state physics yet it can be difficult to connect that language to the MO-based concepts that are used in quantum chemistry.[20,331] Any excited state in a single-excitation theory consists of an excited electron and a hole in the occupied space. A connection between the two formlisms can be made by identifying virtual–occupied function pairs $\psi_a(\mathbf{r}_{\text{elec}})\, \psi_i^*(\mathbf{r}_{\text{hole}})$ as a quasiparticle basis. The transition density kernel $T(\mathbf{r}, \mathbf{r}')$ in eqn. (2.5), written in the form $T(\mathbf{r}_{\text{elec}}, \mathbf{r}_{\text{hole}})$, is then identified as a "wave function" for the exciton. That said, the true excited-state wave function in a many-body formalism is Ψ_{exc} in eqn. (2.8), which is used to construct $T(\mathbf{r}, \mathbf{r}')$. Nevertheless, $T(\mathbf{r}_{\text{elec}}, \mathbf{r}_{\text{hole}})$ is of-

ten called a "wave function" in quasiparticle theories based on the two-particle Green's function and the Bethe-Salpeter equation.[332,333]

Semantics aside, examination of $T(\mathbf{r}_{elec}, \mathbf{r}_{hole})$ reveals the separation and spatial correlations between particle and hole. In quantum chemistry, this form of analysis was pioneered by Mukamel, Tretiak, and Chernyak,[111,312–314,334–336] and later used by others,[337–341] mostly in the context of organic photovoltaic materials and using semi-empirical CIS-type wave functions. These ideas were subsequently formalized by Plasser and co-workers,[18,19,22,200,342] who generalized them to wave functions of arbitrary complexity, represented using non-orthogonal basis functions. Plasser and co-workers also applied these ideas to organic photovoltaics,[306,343–345] albeit using TD-DFT and correlated wave functions rather than semi-empirical methods.

5.1 Electron–hole correlation

If $T(\mathbf{r}_{elec}, \mathbf{r}_{hole})$ is to serve as the exciton wave function then it might seem that $|T(\mathbf{r}_{elec}, \mathbf{r}_{hole})|^2$ should be the corresponding probability density, although this analogy breaks down when one realizes that the normalization condition in eqn. (4.6) is not generally obeyed for correlated wave functions.[18,19] (That has occasionally been used to quantify deviation from one-electron character.[204,346,347]) For single-excitation wave functions, eqn. (4.6) is strictly valid and one may integrate over either $\mathbf{r} \equiv \mathbf{r}_{elec}$ or $\mathbf{r}' \equiv \mathbf{r}_{hole}$ to obtain separate one-particle densities for the electron and the hole.[18] For TD-DFT, these quantities are the same as the particle and hole densities defined in Section 2.2. In terms of $T(\mathbf{r}_{elec}, \mathbf{r}_{hole})$, they are

$$\Delta\rho_{elec}(\mathbf{r}_{elec}) = \int \left|T(\mathbf{r}_{elec}, \mathbf{r}_{hole})\right|^2 d\mathbf{r}_{hole} \qquad (5.1a)$$

$$\Delta\rho_{hole}(\mathbf{r}_{hole}) = \int \left|T(\mathbf{r}_{elec}, \mathbf{r}_{hole})\right|^2 d\mathbf{r}_{elec} \qquad (5.1b)$$

with

$$\int \Delta\rho_{elec}(\mathbf{r})\, d\mathbf{r} = 1 = -\int \Delta\rho_{hole}(\mathbf{r})\, d\mathbf{r}. \qquad (5.2)$$

This normalization is consistent with eqn. (2.13). An atomic partition provides an equivalent definition of the CT numbers that were introduced in Section 4.2:[18,209]

$$\Omega_{A \to B} = \int_A d\mathbf{r}_{hole} \int_B d\mathbf{r}_{elec} \left|T(\mathbf{r}_{elec}, \mathbf{r}_{hole})\right|^2. \qquad (5.3)$$

If we take $|T(\mathbf{r}_{elec}, \mathbf{r}_{hole})|^2$ seriously as a probability distribution for the exciton, it should afford the correlated probability of finding the hole at position $\mathbf{r}_{hole}$, given the presence of the excited electron at position $\mathbf{r}_{elec}$. A schematic view is provided in Fig. 12b. According to eqn. (5.3), this plot conveys the same qualitative information, in the same way, as does a heat-map plot of $\mathbf{\Omega}$, as in the examples of Table 3, but it does so in real space whereas $\Omega_{A \to B}$ does so in atom or functional-group space. The coherence length L_{coh} [eqn. (4.26)] is a characteristic length scale for charge separation (intracule coordinate $\mathbf{r}_{elec} - \mathbf{r}_{hole}$), whereas PR_{diag} [eqn. (4.27)] measures the total size of the excitation (extracule coordinate $\mathbf{r}_{elec} + \mathbf{r}_{hole}$), meaning

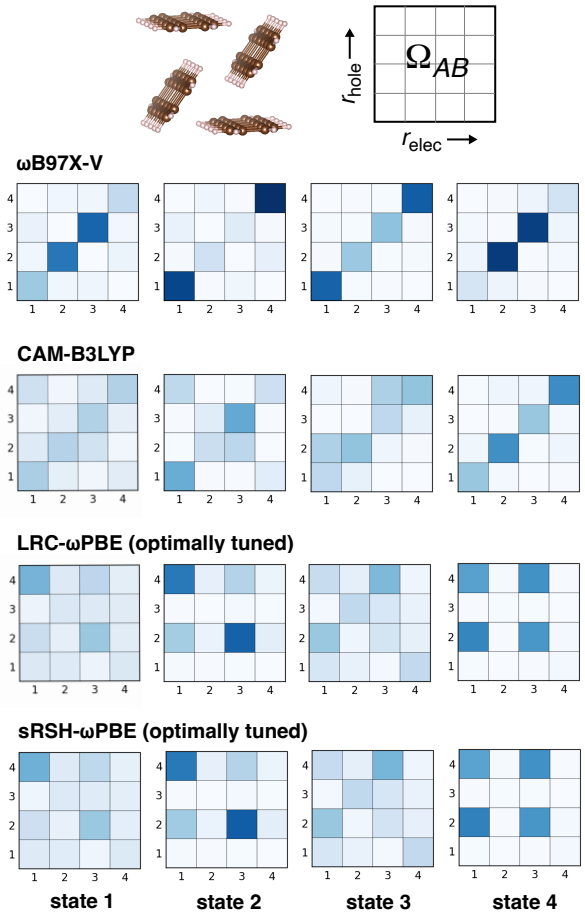The CT matrix $\mathbf{\Omega}$ can be used to demonstrate how various XC

Fig. 13 Heat maps of the CT matrix $\mathbf{\Omega}$ for the first four singlet excited states of the (pentacene)$_4$ model that is shown at the top. Matrix elements $\Omega_{A \to B}$ are obtained from a monomer-based partition of $|T(\mathbf{r}_{hole}, \mathbf{r}_{elec})|^2$ and results from four different XC functionals are shown. Darker blue color indicates larger values of $\Omega_{A \to B}$ whereas white indicates that $\Omega_{A \to B} \approx 0$. Adapted from Ref. 46; copyright 2020 American Chemical Society.

functionals afford qualitatively divergent behavior for excitonic states in multichromophore systems.[46] TD-DFT excitation energies for charge-separated states are exquisitely sensitive to a functional's fraction of Hartree-Fock exchange (if any),[35] much more so than localized excitations such as $\pi\pi^*$ or $n\pi^*$.[31] Adjusting the fraction of exact exchange thus has the effect of tuning charge-separated states in or out of resonance with FE states, which will affect whether (and to what extent) the FE states mix with either localized CT states or delocalized CR states.

As an example, Fig. 13 shows heat maps of $\mathbf{\Omega}$ for singlet excited states in a (pentacene)$_4$ cluster, illustrating significant qualitative discrepancies between results obtained with different functionals. Using ωB97X-V,[348] the states S$_1$ to S$_4$ are mostly FE states, as evident from the diagonal character of the $\mathbf{\Omega}$ heat maps; consult Table 2 and eqn. (4.19) for a guide. For example, the S$_1$ and S$_4$ states primarily involve mixing basis states $|\Psi_1 \Psi_2^* \Psi_3 \Psi_4\rangle$ and $|\Psi_1 \Psi_2 \Psi_3^* \Psi_4\rangle$. Optimally-tuned RSH functionals,[38,43–45] including LRC-ωPBE and a screened RSH approach (sRSH-ωPBE) that respects asymptotic behavior within a low-dielectric crystal

medium,[349] exhibit a much greater degree of charge separation. This separation resembles localized CT insofar as it is not symmetric about the anti-diagonal of $\mathbf{\Omega}$ (*i.e.*, $\Omega_{A\to B}$ is very different from $\Omega_{B\to A}$). CAM-B3LYP presents an intermediate case where CT and FE character are both evident.

Tretiak and co-workers have made extensive use of atomic partitions of the TDMs from semi-empirical quantum chemistry, to analyze excitonic states in conjugated polymers of interest for organic electronics. [111,312,314,334–336,350,351] This analysis has sometimes been ported to all-electron TD-DFT calculations without recognition that AO overlaps need to be considered. [352,353] If those overlaps are ignored, or else if an orthogonalized minimal basis is employed, then there is little distinction between $l_{A\to B}$ in eqn. (4.3) and $\Omega_{A\to B}$ in eqn. (4.9), if normalization is ignored for the purpose of inferring spatial correlations between particle and hole. Tretiak and co-workers use slightly modified CT indices, [312] namely

$$\xi_{AA} = \left| \sum_{\mu \in A} (\Delta \mathbf{P})_{\mu\mu} \right| \tag{5.4}$$

in place of $l_{A\to A}$ and

$$\xi_{AB} = \left[\sum_{\mu \in A} \sum_{\nu \in B} [(\Delta \mathbf{P})_{\mu\nu}]^2 \right]^{1/2} \quad \text{for } A \neq B \tag{5.5}$$

in place of $l_{A\to B}$. When collected into a matrix $\mathbf{\xi}$, these quantities measure electron–hole separation and overall exciton size in the same manner as the $\mathbf{\Omega}$ matrix.

Heat maps of $\mathbf{\xi}$ are depicted in Fig. 14 for a 20-unit PPV oligomer, [336] where indices A and B in ξ_{AB} refer to PPV units. In these examples, the length PR_{diag} in the anti-diagonal direction (extracule coordinate $\mathbf{r}_{\text{elec}} + \mathbf{r}_{\text{hole}}$) signifies that the excitation is delocalized over essentially the entire oligomer, regardless of the XC functional that is employed. On the other hand, the coherence length (in the diagonal direction), which indicates charge separation, is rather sensitive to the fraction of Hartree-Fock exchange, as it was for (pentacene)$_4$. For functionals with a large fraction of exact exchange, including Hartree-Fock theory itself, L_{coh} approaches a limiting value of ≈ 2 monomer units, but for semilocal functionals such as BLYP and PBE the coherence length approaches the length of the entire polymer. This is observed in other conjugated polymers as well. [108,343–345,354]

5.2 Quantifying exciton size

A one-particle probability distribution that preserves certain aspects of electron–hole information is the *electron–hole correlation function*, [333]

$$\mathscr{F}(\mathbf{r}) = \int \left| T(\mathbf{r}+\mathbf{r}_{\text{hole}}, \mathbf{r}_{\text{hole}}) \right|^2 d\mathbf{r}_{\text{hole}} . \tag{5.6}$$

The function $\mathscr{F}(\mathbf{r})$ represents the probability of finding the centroids of the electron and the hole separated by a vector $\mathbf{r}$. The mean electron–hole distance can be sensibly defined as the expectation value of the vector between their barycenters,

$$R_{\text{e-h}} = \left\langle \| \mathbf{r}_{\text{elec}} - \mathbf{r}_{\text{hole}} \| \right\rangle , \tag{5.7}$$
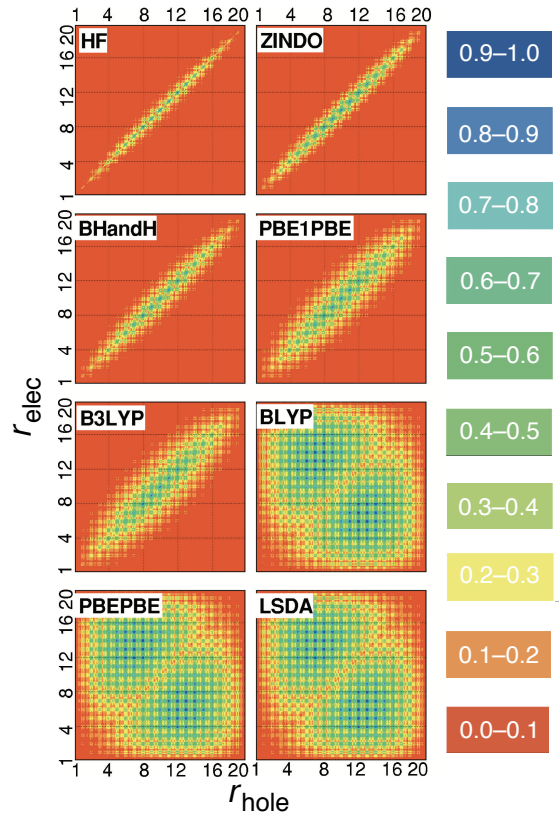

Fig. 14 Heat maps of $\mathbf{\xi}$ for (PPV)$_{20}$ obtained from TD-DFT with various functionals. The $\mathbf{\xi}$ matrix is defined in eqns. (5.4) and (5.5) and its interpretation is the same as that of $\mathbf{\Omega}$, representing $T(\mathbf{r}_{\text{hole}}, \mathbf{r}_{\text{elec}})$ but with the axes measured in units of PPV monomers. Equivalently, the heat map of $\mathbf{\xi}$ represents the probability of transferring charge from the site indicated on the horizontal axis to the site indicated on the vertical axis. Adapted from Ref. 336; copyright 2007 American Institute of Physics.

which is computable by means of $\mathscr{F}(\mathbf{r})$:

$$R_{\text{e-h}} = \int r \mathscr{F}(r) \, dr . \tag{5.8}$$

(Here, $r = \|\mathbf{r}\|$.) The CT character of the excitation in question can be estimated in terms of the fraction of an electron that is transferred (Q_{CT}), which can be defined as

$$Q_{\text{CT}} = 1 - \int_{\mathbf{r} \in V_{\text{molec}}} \mathscr{F}(\mathbf{r}) \, d\mathbf{r} . \tag{5.9}$$

The notation $\mathbf{r} \in V_{\text{molec}}$ indicates integration of the volume occupied by a single molecule in a in a crystal or other aggregate. [333]

Figure 15 plots $\mathscr{F}(\mathbf{r})$ for the lowest few singlet excitons in a periodic calculation of a functionalized pentacene derivative that is perhaps the most widely-investigated SF material. [296–300] The SF process amounts to rapid spin-allowed conversion of a singlet excited state on one molecule into a pair of triplet excitations on two neighboring molecules,

$$\text{S}_0 \xrightarrow{h\nu} \text{S}_1 \xrightarrow{\text{SF}} {}^1(\text{T}_1\text{T}_1) \to \text{T}_1 + \text{T}_1 . \tag{5.10}$$
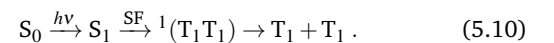
The correlated triplet-pair or "multi-exciton" state, ${}^1(\text{T}_1\text{T}_1)$, represents a true double excitation in electronic structure terms. [355–357]
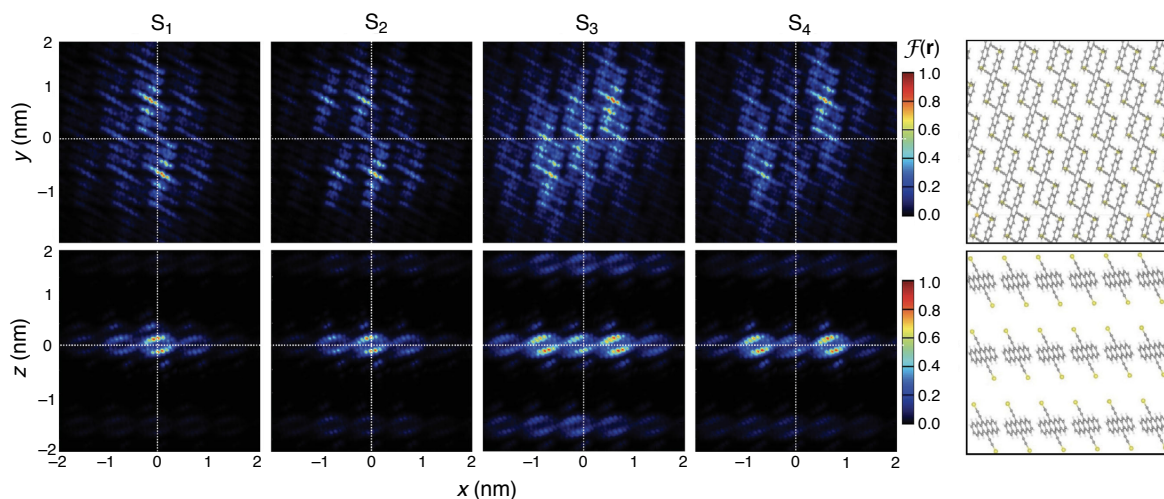
Fig. 15 Electron–hole correlation functions $\mathcal{F}(\mathbf{r})$ [eqn. (5.6)] for the first four singlet excited states of a periodic crystal of 6,13-bis(tri-isopropylsilylethynyl) (TIPS) pentacene. These have been projected onto either the xy plane (upper panels) or the xz plane (lower panels). Corresponding cuts through the crystal structure are shown at the far right, with methyl groups removed from the TIPS side chains for clarity. Reprinted from Ref. 292; copyright 2015 John Wiley & Sons.

Following decoherence, SF ultimately results in two charge carriers ($T_1 + T_1$) for the price of a single photon. This photochemical two-for-one has the potential to overcome the thermodynamic limit on conversion efficiency for one-to-one processes.[358,359] However, there are basic mechanistic questions that are still being investigated, including the role of low-energy CT states,[46,291–295] vibronic coherence,[356,360–366] the nature of exciton/phonon couplings,[367] and whether the $^1(T_1T_1)$ state may represent a trap rather than an intermediate.[368]

In the electron–hole correlation plots in Fig. 15, the origin corresponds to zero net separation between electron and hole ($\mathbf{r}_{\mathrm{elec}} = \mathbf{r}_{\mathrm{hole}}$) but the plots do not indicate significant probability there. Rather, the regions of highest probability in the xy plane are those around $(x = 0, y = \pm 1 \text{ nm})$, indicative of charge separation between nearest-neighbor molecules, although the extent of $\mathcal{F}(\mathbf{r})$ indicates delocalization over as many as three molecules.[292] This leads to an exciton length > 5 Å, as determined by eqn. (5.8), with $\approx 50\%$ CT character according to the definition in eqn. (5.9).[333] In contrast, plots in the xz plane of the crystal indicate no delocalization in the z direction, due to the large intermolecular spacing arising from bulky substituent groups.

The quantity $T(\mathbf{r}_{\mathrm{elec}}, \mathbf{r}_{\mathrm{hole}})$ can also be used to evaluate a variety of statistical properties of the joint electron/hole probability distribution.[20,22] These measures are indicated schematically in Fig. 16 and include the root-mean-square (RMS) size of the electron and the hole,

$$\sigma_{\mathrm{elec}} = \left(\langle \mathbf{r}_{\mathrm{elec}} \cdot \mathbf{r}_{\mathrm{elec}} \rangle - \langle \mathbf{r}_{\mathrm{elec}} \rangle \cdot \langle \mathbf{r}_{\mathrm{elec}} \rangle \right)^{1/2} \tag{5.11a}$$

$$\sigma_{\mathrm{hole}} = \left(\langle \mathbf{r}_{\mathrm{hole}} \cdot \mathbf{r}_{\mathrm{hole}} \rangle - \langle \mathbf{r}_{\mathrm{hole}} \rangle \cdot \langle \mathbf{r}_{\mathrm{hole}} \rangle \right)^{1/2}, \tag{5.11b}$$

and the RMS value of the electron–hole separation,

$$d_{\mathrm{exc}} = \left\langle \| \mathbf{r}_{\mathrm{elec}} - \mathbf{r}_{\mathrm{hole}} \|^2 \right\rangle^{1/2}. \tag{5.12}$$

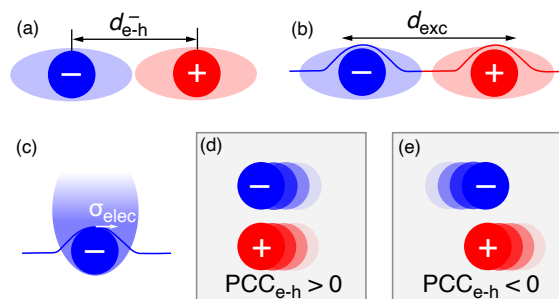The latter provides an alternative to $R_{\mathrm{e-h}}$ in eqn. (5.8), or L_{coh}

Fig. 16 Schematic depictions of statistical measures of electron–hole correlation, including (a) the average electron–hole separation, $d_{\mathrm{e-h}}^-$; (b) the RMS electron–hole separation, d_{exc}; (c) the RMS size of the electron, σ_{elec}; and (d)–(e) Pearson's correlation coefficient for electron and hole, $\mathrm{PCC}_{\mathrm{e-h}}$. Adapted from Ref. 342; copyright 2018 American Chemical Society.

in eqn. (4.26), as a way to characterize exciton size. All three quantities measure electron–hole separation, meaning the anti-diagonal direction $\mathbf{\Omega}$ or $\boldsymbol{\xi}$ (Fig. 12), but they are numerically distinct. These quantities play a central role in attempts to quantify the CT character of a given excited state, which will be explored in Section 6.

To examine these definitions a bit further, we define

$$d_{\mathrm{e-h}}^{\pm} = \left\| \langle \mathbf{r}_{\mathrm{elec}} \rangle \pm \langle \mathbf{r}_{\mathrm{hole}} \rangle \right\|, \tag{5.13}$$

where $\langle \mathbf{r}_{\mathrm{elec}} \rangle$ and $\langle \mathbf{r}_{\mathrm{hole}} \rangle$ are the centroids of the attachment and detachment densities, respectively. Equivalently, these are the expectation values of the position operator, averaged over $\Delta\rho_{\mathrm{elec}}(\mathbf{r})$ or $\Delta\rho_{\mathrm{hole}}(\mathbf{r})$. For example, the x component of $\langle \mathbf{r}_{\mathrm{elec}} \rangle$ is

$$\langle x_{\mathrm{elec}} \rangle = \int x \, \Delta\rho_{\mathrm{elec}}(\mathbf{r}) \, dx. \tag{5.14}$$

The quantity $d_{\mathrm{e-h}}^+$ in eqn. (5.13) is another measure of exciton size. Its value depends on the choice of laboratory-fixed coordi-

nate frame, but given a sensible choice for the coordinate origin $d_{\text{e-h}}^+$ can be used to assess how the exciton migrates upon change in molecular geometry. The quantity $d_{\text{e-h}}^-$ is a measure of the electron–hole separation (see Fig. 16a) but $d_{\text{e-h}}^- = 0$ for any centrosymmetric system.[22] This means that $d_{\text{e-h}}^-$ cannot detect charge separation in any system with inversion symmetry, which has important implications in solid-state systems. In a centrosymmetric (or near-symmetric) solid, the value of $d_{\text{e-h}}^-$ may be zero or small, with a correspondingly small dipole moment change upon excitation, even for an exciton that is characterized by significant charge separation.[46] That charge separation can be detected by examining the CT numbers $\Omega_{A\to B}$ (using heat maps of the $\boldsymbol{\Omega}$ matrix, for example), but it would be useful to have a quantitative metric that might afford a length scale for charge separation.

In view of these remarks, d_{exc} in eqn. (5.12) seems to offer a more robust measure of electron–hole separation, as compared to $d_{\text{e-h}}^-$. The former satisfies mathematical bounds given by[22]

$$d_{\text{exc}}^2 \geq (d_{\text{e-h}}^-)^2 + (\sigma_{\text{elec}} - \sigma_{\text{hole}})^2 \qquad (5.15a)$$

$$d_{\text{exc}}^2 \leq (d_{\text{e-h}}^-)^2 + (\sigma_{\text{elec}} + \sigma_{\text{hole}})^2 . \qquad (5.15b)$$

The physical interpretation of these bounds is that the RMS exciton size (d_{exc}) cannot be larger than the sum of the RMS sizes of the electron and the hole.

For MEH-PPV polymers (Fig. 7c), examination of d_{exc} and $d_{\text{e-h}}^\pm$ leads to the conclusion that excitations in this system can be viewed as two independent quasiparticles in the intracule and extracule coordinates of the electron/hole pair.[163] As compared to geometric considerations, the RMS exciton size proves to be a better diagnostic for the effective size of the chromophore in a long, disordered polymer. That length scale (measured by d_{exc}) is sometimes longer than what might have been anticipated simply by counting conjugated bonds, due to electronic coupling between conjugatively distinct segments of the polymer. For the low-lying excited states of interest for optoelectronic applications, the value of d_{exc} is effectively constant whereas $d_{\text{e-h}}^+$ is observed to increase with excitation energy.[163]

Other statistical descriptors of an exciton include the covariance between the vectors $\mathbf{r}_{\text{elec}}$ and $\mathbf{r}_{\text{hole}}$, defined as

$$\text{COV}(\mathbf{r}_{\text{hole}}, \mathbf{r}_{\text{elec}}) = \langle \mathbf{r}_{\text{hole}} \cdot \mathbf{r}_{\text{elec}} \rangle - \langle \mathbf{r}_{\text{hole}} \rangle \cdot \langle \mathbf{r}_{\text{elec}} \rangle . \qquad (5.16)$$

This quantity is connected to the RMS exciton size via the relation[22,342]

$$d_{\text{exc}}^2 = (d_{\text{e-h}}^-)^2 + \sigma_{\text{elec}}^2 + \sigma_{\text{hole}}^2 - 2\,\text{COV}(\mathbf{r}_{\text{hole}}, \mathbf{r}_{\text{elec}}) . \qquad (5.17)$$

The covariance can be used to compute Pearson's correlation coefficient (PCC) between the probability distributions for the electron and the hole, which is

$$\text{PCC}_{\text{e-h}} = \frac{\text{COV}(\mathbf{r}_{\text{hole}}, \mathbf{r}_{\text{elec}})}{\sigma_{\text{elec}}\,\sigma_{\text{hole}}} . \qquad (5.18)$$

This quantity is defined such that

$$-1 \leq \text{PCC}_{\text{e-h}} \leq 1 , \qquad (5.19)$$

with positive values indicating concerted motion of the two quasi-particles (Fig. 16d) and negative values indicating that they avoid each other dynamically (Fig. 16e).[22]

Analysis of correlations between the size of the electron and hole quasiparticles, as a function of conjugation length, suggests that the semilocal TD-DFT results for $(\text{PPV})_{20}$ in Fig. 14 are consistent with quasiparticles avoiding one another, or in other words, more consistent with a CT state than with a bound exciton.[345] Reducing the fraction of Hartree-Fock exchange is tantamount to eliminating electron–hole attraction, leading to an effectively repulsive interaction between the excited electron and the hole.[336] As a result, *TD-DFT using semilocal functionals contains no electron–hole interaction*, and is inherently unable to describe bound excitons. This observation explains large errors for TD-DFT excitations energies in some conjugated π systems.[220,222,369,370] In the $(\text{PPV})_{20}$ example at least, the failure mode cannot be deduced from the MOs alone because the anti-diagonal length scales (PR_{diag}) are essentially identical for all functionals.[345] Instead, real-space analysis of the transition density is required, to visualize electron–hole correlation.[18]

6 Diagnostics for charge transfer

Results for models of crystalline tetracene (Fig. 13) and for conjugated polymers (Fig. 14) allude to systemic problems with the description of long-range CT in TD-DFT calculations. These problems are well documented,[1,9,28–36] but for completeness they are briefly recapitulated in Section 6.1. Nevertheless, for localized valence excitations TD-DFT affords a level of accuracy that is difficult to match with any other quantum chemistry method except in very small molecules. That accuracy depends sensitively on the choice of XC functional but mean absolute errors of ~ 0.3 eV have been demonstrated (using benchmark data sets) for the best-performing functionals.[1,10–14]

The imbalance between TD-DFT's treatment of localized versus charge-separated excitations has spawned a small industry dedicated to providing diagnostic tools to determine which excitation energies may be problematic, as valence and CT excitations can mix in large systems. (This is especially true in the presence of explicit solvent molecules.[30–32,371]) Historically speaking, the first such metric was introduced by Tozer and co-workers.[23] That metric, which remains useful, is described in Section 6.2 followed by a more general discussion in Section 6.3 that introduces several other CT metrics and relates them back to statistical measures of electron–hole separation that were introduced in Section 5.2. These connections have seldom been made clear in the literature, and even more infrequently have they been discussed in terms of physically meaningful properties of the exciton.

6.1 CT problem in TD-DFT

A fundamental discussion of how CT problems in TD-DFT arise from approximate XC functionals can be found in Ref. 33. A succinct and non-technical summary is that for any semilocal XC functional, including any generalized gradient approximation (GGA) that lacks Hartree-Fock exchange and even meta-GGAs that lack Hartree-Fock exchange, the interaction between the ex-

cited electron and the hole vanishes beyond the length scale at which electron and hole wave functions cease to overlap. This was mentioned above, in the context of understanding unbound excitons in conjugated polymers (Section 5.2), but it can be formulated and understood in a general way.

For well-separated donor and acceptor orbitals ψ_i and ψ_a, respectively, the TD-DFT orbital Hessian matrix elements reduce to

$$A_{ia,jb} \approx (\varepsilon_a - \varepsilon_i)\delta_{ij}\delta_{ab} - C_{HFX}(ij|ab) \qquad (6.1a)$$

$$B_{ia,jb} \approx 0 \qquad (6.1b)$$

where C_{HFX} is the coefficient of Hartree-Fock exchange.[1] For any semilocal functional ($C_{HFX} = 0$), eqn. (6.1a) reduces to a block-diagonal form with diagonal matrix elements that are simply differences in Kohn-Sham energy levels, $\varepsilon_a - \varepsilon_i$. For a sufficiently large system, there is nothing to prevent spatially separated orbitals ψ_i and ψ_a from having an energy gap $\lambda = hc/(\varepsilon_a - \varepsilon_i)$ that happens to coincide with a visible or ultraviolet wavelength. These will manifest in semilocal TD-DFT as spurious excited states,[1,28–32] which appear to move charge around at relatively low energies.[30] These spurious CT excitation energies are much lower than one would estimate using Mulliken's formula for long-range CT excitation energies,[9] which is

$$\omega_{CT}(R) \gtrsim IE + EA - \frac{1}{4\pi\varepsilon_0 R} \ . \qquad (6.2)$$

Equation (6.2) expresses the excitation energy ω_{CT} between well-separated donor and acceptor moieties in terms of the ionization energy (IE) of the donor and the electron affinity (EA) of the acceptor, along with a Coulomb penalty of $1/(4\pi\varepsilon_0 R)$ for creating an ion pair. What is missing in semilocal TD-DFT is the Coulomb penalty for separating charge, which is provided in hybrid DFT by the Hartree-Fock exchange integral $(ij|ab)$ in eqn. (6.1a).

If the spurious CT states predicted by TD-DFT are relatively sparse in the excitation manifold then they will be optically dark, consistent with a vanishing transition moment between non-overlapping donor and acceptor orbitals, $\langle\psi_i|\hat{\mu}_x|\psi_a\rangle \approx 0$. A solvated system, however, will engender a dense manifold of spurious CT states, some of whose energies will be (accidentally) near-resonant with genuine dipole-allowed transitions. This leads to intensity borrowing by the spurious CT states, with concomitant loss of intensity by the genuine bright state.[30] Just as certain higher-lying valence excitations predicted by MO theory may be absent from the spectrum, having been "dissolved in the Rydberg sea",[372,373] one may state that valence transitions in large-scale TD-DFT can dissolve into a charge-transfer sea. Hybrid functionals with relatively small fractions of Hartree-Fock exchange, including B3LYP with $C_{HFX} = 0.2$ and PBE0 with $C_{HFX} = 0.25$, can still be susceptible to this problem, albeit less so than semilocal functionals.[30,31]

To diagnose and quantify anomalous CT in TD-DFT calculations, one may employ properties of the TDM to measure exciton size, delocalization, and charge-separated character, as discussed in Section 5. A schematic example is shown in Fig. 17 us-
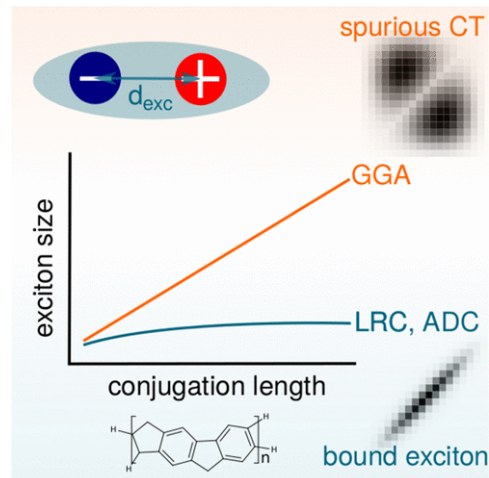

Fig. 17 Cartoon depiction of exciton size versus conjugation length for ladder-type poly(*p*-phenylene). The quantity d_{exc} [eq. (5.12)] is the RMS exciton size, which increases without bound when GGA functionals are used in TD-DFT. Reprinted from Ref. 345; copyright 2017 American Chemical Society.

ing ladder-type poly(*p*-phenylene) polymers.[338,374] Here, semilocal TD-DFT calculations predict a bound exciton that is delocalized across the entire polymer, regardless of oligomer length, which is the same problem that was documented for (PPV)$_{20}$ in Fig. 14. Hybrid functionals significantly attenuate the charge separation but not the FE delocalization.[336] LRC functionals, in which $C_{HFX} \to 1$ at long range only,[1,31,40–42,46] predict a finite size limit for the exciton, in agreement with many-body calculations.[345] "Optimally-tuned" LRC functionals, wherein the range-separation parameter is adjusted to satisfy the IE theorem (IE $= -\varepsilon_{HOMO}$), are often used as a workaround for TD-DFT's CT problem.[37–39,43–45]

The DMABN molecule provides an interesting case study. Figure 18 characterizes the nature of its $S_0 \to S_1$ and $S_0 \to S_2$ transitions, accessing the ^1L_a and ^1L_b states that were introduced in Section 4.3. According to the lore, one of these should be the LE($\pi\pi^*$) state and the other should exhibit nascent CT character that is enhanced upon twisting. At the planar ground-state geometry (on the left in Fig. 18), both transitions exhibit significant delocalization across the donor–π–acceptor framework, although the attachment density (representing the excited electron) is slightly enhanced on the cyano group in S_2 as compared to S_1. Upon 90° twist of the amino group (on the right in Fig. 18), and in a polar dielectric medium, detachment densities for both transitions localize onto the amino lone pair. For the twisted geometry, S_1 is clearly the CT state and it is significantly stabilized by solvent polarization. In contrast, the excitation energy for the LE state is scarcely affected by the twist.

A point of historical debate was the fact that the PBE and B3LYP functionals both predict reasonably accurate excitation energies for the ^1L_a and ^1L_b states, for DMABN and other small donor–π–acceptor molecules.[23,375,376] A resolution to this apparent paradox comes in the form of metric for quantifying CT character, which will be introduced below and ultimately suggests that the extent of CT in the planar geometry of DMABN is not very large.[23]
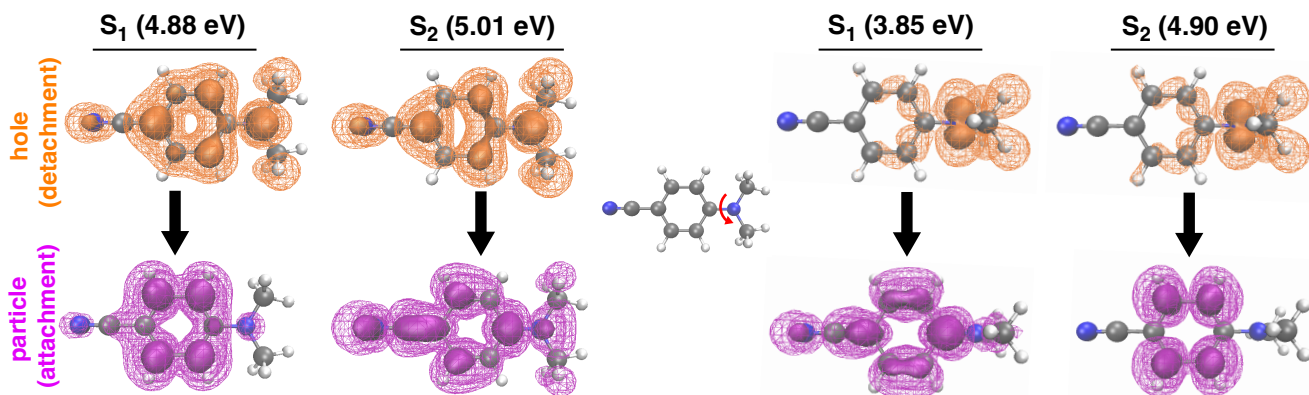
Fig. 18 Particle (attachment) and hole (detachment) densities for the $S_0 \to S_1$ and $S_0 \to S_2$ transitions in DMABN, in both its planar ground-state geometry (on the left) and with a 90° twist of the dimethylamino moiety (on the right). Opaque and wire mesh surfaces encapsulate 50% and 90% of each density, respectively. TD-DFT/TDA calculations were performed using LRC-ωPBE/6-31G* with a dielectric constant of 37.5 (representing acetonitrile).

Only in hindsight can this be inferred from the densities in Fig. 18, which do not suggest any dramatic difference between S_1 and S_2 at the ground-state geometry. (The difference is much more pronounced in the twisted geometry.) As such, DMABN serves as a cautionary tale warning that one must be careful with blanket statements that TD-DFT fails categorically for CT states, or at least one must be careful about what gets called a CT excitation. Energies for truly long-range CT will indeed be systematically (and catastrophically) underestimated by semilocal TD-DFT, but errors may be small if the donor and acceptor orbitals are not completely separated in space. In the planar geometry of ground-state DMABN, these orbitals are clearly *not* well-separated in space. A metric that might indicate this fact is introduced next.

6.2 Tozer's spatial proximity metric

A resolution to the DMABN paradox was provided by the very first CT metric to be introduced for TD-DFT calculations, by Tozer and co-workers.[23] Their proposed metric is defined as

$$\Lambda = \frac{\sum_{ia} \kappa_{ia}^2 O_{ia}}{\sum_{jb} \kappa_{jb}^2} \tag{6.3}$$

where

$$\kappa_{ia} = x_{ia} + y_{ia} \tag{6.4}$$

and

$$O_{ia} = \int |\psi_i(\mathbf{r})| \, |\psi_a(\mathbf{r})| \, d\mathbf{r} . \tag{6.5}$$

Note the absolute value signs in the integrand of O_{ia}, which are necessary because occupied and virtual MOs are orthogonal, $\langle \psi_i | \psi_a \rangle = 0$. For this reason, we resist using the term "overlap" to describe the spatial proximity of MOs. If we need a name for O_{ia}, we will call it the "spatial overlap" of ψ_i and ψ_a. This and similar metrics are sometimes used to quantify the spatial proximity of HOMO and LUMO in donor–acceptor materials.[377]

In view of the normalization condition for $\mathbf{x}$ and $\mathbf{y}$ [eqn. (2.4)], it is unclear why the definition of Λ does not involve both $\mathbf{x} + \mathbf{y}$ and $\mathbf{x} - \mathbf{y}$. Perhaps it is in loose analogy to the expressions for the particle and hole density matrices [eqn. (2.11)], which contain

terms like $(\mathbf{x} + \mathbf{y})^\dagger (\mathbf{x} + \mathbf{y})$ and $(\mathbf{x} + \mathbf{y})(\mathbf{x} + \mathbf{y})^\dagger$, although these expressions also contain $(\mathbf{x} - \mathbf{y})^\dagger (\mathbf{x} - \mathbf{y})$ and $(\mathbf{x} - \mathbf{y})(\mathbf{x} - \mathbf{y})^\dagger$. (The latter terms have sometimes been erroneously omitted.[220]) Whatever the reason, the definition of Λ in eqn. (6.3) is used consistently in practice,[23,25,220,378–380] yet the decision to abdicate proper normalization seems questionable and has implications for other CT metrics that are discussed in Section 6.3. Within the TDA there is no issue, since $\mathbf{y} = \mathbf{0}$ and $\sum_{ia} x_{ia}^2 = 1$, thus the denominator in eqn. (6.3) has well-defined normalization in that case. This implies that $0 \le \Lambda \le 1$ within the TDA, but this need not be the case for full TD-DFT calculations that include the y_{ia} amplitudes.

Tozer *et al.* find that $0.45 \le \Lambda \le 0.89$ for localized valence excitations, whereas Rydberg excitations lie in the range $0.08 \le \Lambda \le 0.27$.[23] Examining excitation energy errors as a function of Λ, it becomes clear that there are approximate, functional-dependent thresholds below which TD-DFT results should not be trusted. Errors are large, for example, when $\Lambda < 0.4$ for B3LYP or when $\Lambda < 0.3$ for PBE,[23] and values of Λ correlate with excitation energy errors along flexible torsional coordinates that can lead to intramolecular CT in some conformations.[381] Resolution of the DMABN paradox comes in noting that its intramolecular CT excitation corresponds to $\Lambda = 0.72$ (TD-PBE) in the planar geometry,[23] which is not very CT-like. For the LRC-ωPBE/6-31G* calculations that are shown in Fig. 18, the corresponding values are $\Lambda(S_1) = 0.53$ and $\Lambda(S_2) = 0.67$ in the planar geometry, indicating that the nominal CT state actually has somewhat larger spatial proximity between particle and hole. This is true in the twisted geometry as well, although the values of Λ are much smaller and lie in the "danger zone": $\Lambda(S_1) = 0.20$ and $\Lambda(S_2) = 0.22$. Results at the TD-B3LYP/6-31G* level are similar.

While the Λ metric has proven successful as a diagnostic for TD-DFT errors, its numerical value does not provide much physical insight. Moreover, it may fail to detect problems when the excited state involves excitation from a relatively compact orbital into a much more delocalized orbital,[378] as the two MOs may share significant spatial proximity (in the sense of O_{ia}) yet the delocalized nature of the final state might still engender an er-

roneously low excitation energy. Large density rearrangements in certain excited states of PAH molecules fall into this category, and anomalously low TD-DFT excitation energies are obtained for larger aromatic systems.[220–222,382] These can be rectified through the use of asymptotically-correct LRC functionals,[220,382] yet such states do not exhibit what might be understood as CT in intuitive chemical terms, involving donor and acceptor functional groups. Moreover, values of Λ do not portend any problems in such cases.[220] Perhaps for these reasons, there has been significant effort devoted to identifying alternative CT metrics for use in TD-DFT. This is discussed in the next section.

6.3 Other CT metrics

Much of the work on alternative CT metrics for TD-DFT originates with Ciofini and co-workers,[24,229,239,354,383–388] who introduce particle and hole densities but do not refer to them as such. Instead, these quantities are called $\rho_+(\mathbf{r})$ and $\rho_-(\mathbf{r})$ and are defined by regions of space where the excitation engenders either positive or negative changes in the density, respectively:[354,385]

$$\Delta\rho_+(\mathbf{r}) = \begin{cases} \Delta\rho(\mathbf{r}), & \Delta\rho(\mathbf{r}) > 0 \\ 0, & \Delta\rho(\mathbf{r}) \leq 0 \end{cases} \quad (6.6a)$$

$$\Delta\rho_-(\mathbf{r}) = \begin{cases} 0 & \Delta\rho(\mathbf{r}) > 0 \\ \Delta\rho(\mathbf{r}), & \Delta\rho(\mathbf{r}) \leq 0 \end{cases} . \quad (6.6b)$$

There is no new information here, relative to what was discussed in Sections 2.2 and 2.3, because one may identify $\Delta\rho_+(\mathbf{r})$ as $\Delta\rho_{\text{elec}}(\mathbf{r})$ and $\Delta\rho_-(\mathbf{r})$ as $\Delta\rho_{\text{hole}}(\mathbf{r})$. To see this, recall that the attachment and detachment densities were defined by eigenvectors of $\Delta\mathbf{P}$ corresponding to positive eigenvalues ($\Delta\mathbf{P}^{\text{attach}}$) or negative eigenvalues ($\Delta\mathbf{P}^{\text{detach}}$); see eqn. (2.17). Since $\Delta\rho_{\text{elec}}(\mathbf{r})$ and $\Delta\rho_{\text{hole}}(\mathbf{r})$ have names that invoke both their physical meaning and their connection to the particle/hole formalism, we will use $\Delta\rho_{\text{elec}}(\mathbf{r})$ and $\Delta\rho_{\text{hole}}(\mathbf{r})$ in place of $\Delta\rho_+(\mathbf{r})$ and $\Delta\rho_-(\mathbf{r})$.

Ciofini et al.[354] introduced what is now a widely-used measure of charge separation, which they call D_{CT} and which is equal to the distance between the centroids of $\Delta\rho_{\text{elec}}(\mathbf{r})$ and $\Delta\rho_{\text{hole}}(\mathbf{r})$. That quantity, however, is simply $d_{\text{e-h}}^-$ as defined in eqn. (5.13). In more detail,

$$d_{\text{e-h}}^\pm = \left\| \int \left[\Delta\rho_{\text{elec}}(\mathbf{r}) \pm \Delta\rho_{\text{hole}}(\mathbf{r}) \right] \hat{\mathbf{r}} \, d\mathbf{r} \right\|, \quad (6.7)$$

where $\|\cdots\|$ indicates the legnth of the vector that is defined by three different integrals, substituting x, y, or z for $\hat{\mathbf{r}}$ in eqn. (6.7) to define components of the vector, as in the definition of $\langle x_{\text{elec}} \rangle$ in eqn. (5.14). The metric $D_{\text{CT}} \equiv d_{\text{e-h}}^-$ is increasingly being used to analyze TD-DFT calculations,[24,229,239,354,383–389] although most authors refer to it as "D_{CT}", "Ciofini's CT metric", or similar language that obscures its straightforward physical interpretation as the distance between barycenters of the particle and the hole.[20] Although the physical interpretation has been noted elsewhere,[354,388] failure to introduce particle and hole densities *per se* obscures the conceptual origin of D_{CT} and its connection to quantities such as the attachment and detachment densities. Call-
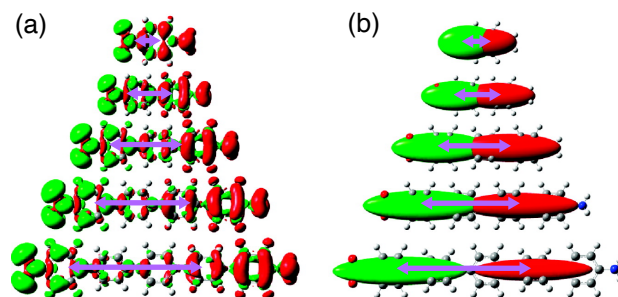

Fig. 19 (a) Electron and hole densities (in green and red, respectively) and (b) Gaussian approximations to these quantities for a sequence of poly(*p*-phenyl)nitroanilines, $O_2N–(C_6H_4)_n–NH_2$. Calculations were performed at the TD-PBE0/6-31+G* level using a solvent model.[354] Purple arrows connects centroids of the electron and hole densities. Adapted from Ref. 354; copyright 2011 American Chemical Society.

ing this quantity $d_{\text{e-h}}^-$ makes the physical meaning inherent in the nomenclature; the definition in eqn. (5.13) is obvious and meaningful. More complicated generalizations of D_{CT} have been suggested,[387] though it is not clear what advantages these may have as compared to straightforward moment analysis of the excitonic wave function, à la eqns. (5.11) and (5.12).

As noted in Section 5.2, $d_{\text{e-h}}^- \equiv 0$ for any centrosymmetric system.[22] To obtain a non-vanishing CT metric for systems with inversion symmetry, Ciofini et al. introduce alternative diagnostics that they call the "t index"[354,383] and the "H index".[229,239,354,383] The latter quantity (H) is essentially $(\sigma_{\text{elec}} + \sigma_{\text{hole}})/2$ but restricted to a one-dimensional donor–acceptor coordinate. This provides a measure of the exciton's spread, and the t-index is then defined as $t = D_{\text{CT}} - H$. We suggest replacing t with an alternative measure of essentially the same information, the *charge-displacement distance*,[1] which we define as

$$d_{\text{CD}} = d_{\text{e-h}}^- - \frac{1}{2}\left(\sigma_{\text{elec}} + \sigma_{\text{hole}}\right). \quad (6.8)$$

The quantity d_{CD} represents the center-to-center distance between electron and hole, reduced by the average of the RMS size of either quasiparticle. It provides a physically meaningful way to combine the electron–hole separation $d_{\text{e-h}}^-$ with something that measures the extent of the excitonic wave function, providing an intuitive way to convey the same information as the D_{CT} and t indices.

A novel analysis tool introduced by Ciofini et al.[354] is the idea of Gaussian approximations to $\Delta\rho_{\text{elec}}(\mathbf{r})$ and $\Delta\rho_{\text{hole}}(\mathbf{r})$ that are based on the rigorous second moments of the transition density, *i.e.*, the quantities σ_{elec}^2 and σ_{hole}^2 that are defined in eqn. (5.11). These approximations provide a quantitative way to realize the cartoons in Fig. 16, which might be easier to conceptualize than the transition density itself because nodal structure is removed. Examples are depicted in Fig. 19 for a sequence of poly(*p*-phenyl)nitroaniline molecules. Due to the complex nodal structure along the conjugated backbone of these molecules (Fig. 19a), barycenters of $\Delta\rho_{\text{elec}}(\mathbf{r})$ and $\Delta\rho_{\text{hole}}(\mathbf{r})$ are more clearly evident in their Gaussian approximations (Fig. 19b). Whereas the particle and hole densities extend to the very edges of the molecule, the
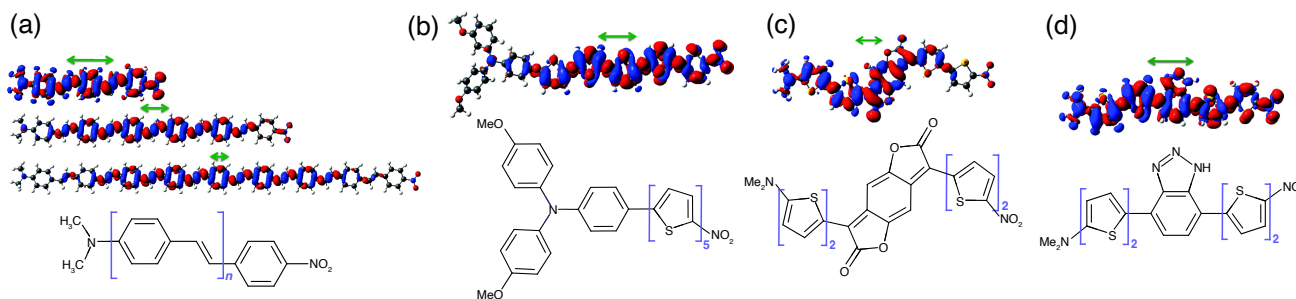
Fig. 20 Particle densities $\Delta\rho_{\text{elec}}(\mathbf{r})$ (in red) and hole densities $\Delta\rho_{\text{hole}}(\mathbf{r})$ (in blue) for various push-pull chromophores that are indicated in the lower part of the figure. Each chromophore has the structure $(CH_3)_2N$–π–NO_2, where "π" indicates a large conjugated system. Examples include: (a) several oligomers of α,ω-dimethylaminonitro-(p-phenylene vinylene)$_n$; (b) a tertiary amine of the form $N(PhOCH_3)_2(PhR)$, where Ph = phenyl and R is a pentathiophene side chain with a terminal nitro group; and finally, α,ω-dimethylaminonitro-(p-thiophene)$_5$ with the central thiophene unit replaced by either (c) benzodifuranone or else (d) benzotriazole. Green arrows indicate the charge-separation distance, $d_{\text{e-h}}^-$. These arrows have been displaced away from the molecules for clarity but their endpoints coincide with the centroids of the particle and hole densities. Adapted from Ref. 239; copyright 2012 American Chemical Society.
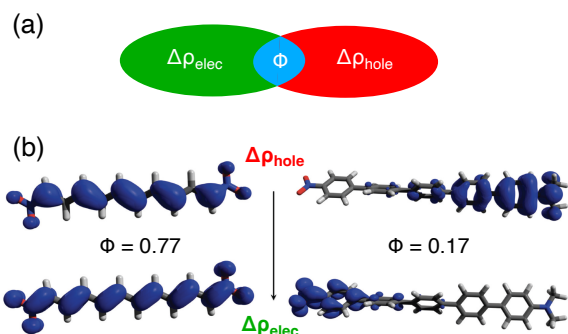

Fig. 21 (a) Schematic view of the charge-separation metric ϕ defined in eqn. (6.9), using cartoon representations of the particle and hole densities made to resemble those in Fig. 19b. Roughly speaking, the integrand in eqn. (6.9) is non-zero in the blue region of overlap between $\Delta\rho_{\text{elec}}(\mathbf{r})$ and $\Delta\rho_{\text{hole}}(\mathbf{r})$. (b) Examples of a localized excitation in the polyene $O_2N(CH)_{10}NO_2$ (on the left) and a CT excitation in the push-pull polymer O_2N–$(C_6H_4)_5$–$N(CH_3)_2$ (on the right), with values of ϕ indicated. Calculations in (b) were performed at the TD-PBE0/6-311++G(2d,p) level and the plots are adapted from Ref. 17.

charge separation distance $d_{\text{e-h}}^-$ is noticeably shorter and is indicated by the arrows in Fig. 19.

This is even more clear in the examples of Fig. 20, where plots of the particle and hole densities appear to be considerably more delocalized than the quantitative measure afforded by $d_{\text{e-h}}^-$. The extent of spatial charge separation is therefore smaller than plots of $\Delta\rho_{\text{elec}}(\mathbf{r})$ and $\Delta\rho_{\text{hole}}(\mathbf{r})$ might lead one to imagine. Notably, the isocontour value that is used in this type of isosurface plot can be manipulated to make an orbital or density appear almost arbitrarily compact or diffuse. For that reason, the author recommends that such plots should always indicate the fraction of the density that is encapsulated within the isosurface. Only then can the size of two densities be compared side-by-side.[161]

Long-distance charge separation is characterized by negligible overlap between particle and hole densities, meaning that $\Delta\rho_{\text{elec}}(\mathbf{r})\,\Delta\rho_{\text{hole}}(\mathbf{r}) \approx 0$ everywhere in space. Based on that ob-

servtion, Etienne *et al.*[16,17,390] suggest a charge-overlap metric

$$\phi = \int \left|\Delta\rho_{\text{elec}}(\mathbf{r})\,\Delta\rho_{\text{hole}}(\mathbf{r})\right|^{1/2}d\mathbf{r}\,. \tag{6.9}$$

We omit a normalizing denominator that is included in Ref. 16, as it equals unity for TD-DFT calculations because both $\Delta\rho_{\text{elec}}(\mathbf{r})$ and $|\Delta\rho_{\text{hole}}(\mathbf{r})|$ integrate to exactly one electron. Roughly speaking, the integral in eqn. (6.9) involves the blue region that is depicted schematically in Fig. 21a.

The metric ϕ is defined such that $0 \leq \phi \leq 1$. If $\phi = 0$ then there is no spatial overlap between electron and hole, thus the excitation in question is entirely CT-like. An example that lies close to this limit is an end-to-end donor–acceptor electron-transfer excitation in a twisted push-pull chromophore whose particle and hole densities are plotted on the right side of Fig. 21b. The twisted geometry severs the conjugation of the π system, resulting in particle and hole densities that localize on opposite ends of the molecule and a small value of the charge-overlap metric, $\phi \approx 0.2$. On the right in Fig. 21b is an excited state in a different molecule that lies near the opposite limit, with significant spatial overlap of $\Delta\rho_{\text{elec}}(\mathbf{r})$ and $\Delta\rho_{\text{hole}}(\mathbf{r})$. In the latter case, both the electron and the hole are delocalized over the length of the molecule, and $\phi \approx 0.8$.

Other CT metrics have been proposed in the spirit of Λ in eqn. (6.3) but attempting to find a diagnostic whose numerical value might be physically meaningful. One of these is a charge-separation metric Δr,[25,26] defined as

$$\Delta r = \frac{\sum_{ia}\kappa_{ia}^2\|\mathbf{R}_{ia}\|}{\sum_{jb}\kappa_{jb}^2} \tag{6.10}$$

where

$$\mathbf{R}_{ia} = \langle\psi_i|\hat{\mathbf{r}}|\psi_i\rangle - \langle\psi_a|\hat{\mathbf{r}}|\psi_a\rangle\,. \tag{6.11}$$

The quantity $\mathbf{R}_{ia}$ is the displacement vector between the centroids of orbitals $\psi_i(\mathbf{r})$ and $\psi_a(\mathbf{r})$, thus Δr averages the charge displacement associated with each excitation $\psi_i \rightarrow \psi_a$, using weights κ_{ia}^2. Although this seems like an intuitive and reasonable way to measure charge separation, the utility of Δr as a separate metric is
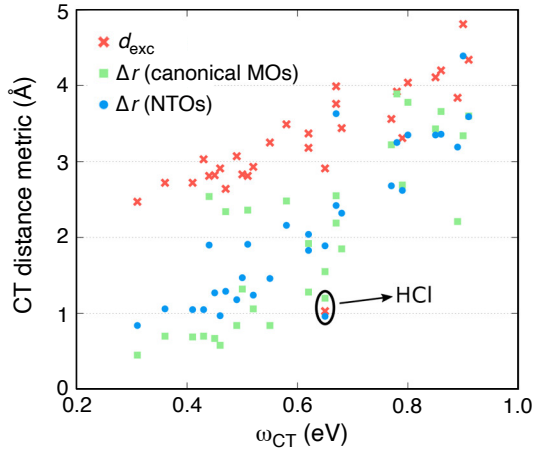
Fig. 22 Correlation between CT excitation energies (ω_{CT}) and various CT metrics. The HCl molecule defies the overall trend and is indicated explicitly. Adapted from Ref. 205.

questionable. Within the TDA, this quantity is

$$\Delta r \stackrel{\text{TDA}}{=} \sum_{ia} x_{ia}^2 \|\mathbf{R}_{ia}\| , \qquad (6.12)$$

which likely encodes similar information as compared to $d_{\text{e-h}}^-$. For full TD-DFT, Δr in eqn. (6.10) employs the same curious choice of normalization that was used to define Λ, namely, use of κ_{jb}^2 in the denominator.

Perhaps more damningly, Δr is not invariant to orbital rotations; its numerical value depends upon which MOs are used. [26] It has been suggested to evaluate Δr in NTO basis, as this affords good correlation between Δr and D_{CT}, [26] but the need to make such a choice is a bothersome artifact of having sacrificed orbital invariance. For an alternative data set of intramolecular CT energies, [391] reasonable correlations are found between definitions of Δr based on either canonical MOs or NTOs, but those values also correlate well with d_{exc} as shown in Fig. 22. [205]

The quantities d_{exc} and $d_{\text{e-h}}^-$, along with expectation values such as $\langle \mathbf{r}_{\text{elec}} \rangle$ and $\langle \mathbf{r}_{\text{hole}} \rangle$, are invariant to unitary transformations of either the occupied MOs or the virtual MOs, just like excitation energies and other excited-state properties in TD-DFT. It is this invariance that provides the freedom to define NTOs, or to use localized MOs, [392–396] without affecting observables, because the aforementioned quantities are fundamental properties of the exciton, independent of representation. As such, these are less arbitrary ways to characterize the nature of a given excited state, as compared to a quantity such as Δr that depends on the choice of representation.

Both $d_{\text{e-h}}^-$ and Δr vanish in centrosymmetric systems, [397] which is a significant drawback in those cases that is not shared by d_{CD}. Alternatively, to obtain a non-vanishing metric in the presence of inversion symmetry, an "effective electron displacement" measure has been suggested, [397] defined as

$$\Gamma = \Delta r + \Delta \sigma . \qquad (6.13)$$

This combines Δr from eqn. (6.10) with

$$\Delta \sigma = \frac{\sum_{ia} \kappa_{ia}^2 |\sigma_i - \sigma_a|}{\sum_{jb} \kappa_{jb}^2} \qquad (6.14)$$

where

$$\sigma_r = \left(\langle \psi_r | \hat{\mathbf{r}} \cdot \hat{\mathbf{r}} | \psi_r \rangle - \| \langle \psi_r | \hat{\mathbf{r}} | \psi_r \rangle \|^2 \right)^{1/2} . \qquad (6.15)$$

The quantity σ_r^2 is the second moment of orbital ψ_r. In a sense, $\Delta \sigma$ is conceptually similar to d_{exc} in eqn. (5.12) in the same way that Δr is conceptually similar to $d_{\text{e-h}}^-$, with the important distinction that both Δr and $\Delta \sigma$ mangle the normalization when $\mathbf{y}$ is nonzero, and that the numerical values of both Δr and $\Delta \sigma$ depend upon the choice of representation.

Correcting the normalization by invoking the TDA, the electron displacement Γ is likely to contain similar information as $d_{\text{e-h}}^- + d_{\text{exc}}$. As such, we suggest that

$$\tilde{d}_{\text{CD}} = d_{\text{e-h}}^- + d_{\text{exc}} \qquad (6.16)$$

is an alternative charge-displacement metric that is constructed from well-defined properties of the exciton, independent of the choice of representation. It should be complementary (though not equivalent) to d_{CD} in eqn. (6.8). This analysis clarifies why numerical values of various charge-displacement metrics are found to be strongly correlated with one another. [26,205,247]

Despite their shortcomings, the metrics Δr and Γ correlate well enough with the largest errors in TD-DFT excitation energies so that one may define a "trust radius" based on their values. [25,397] For GGA functionals, and with Γ evaluated in the NTO representation, it is suggested that states with $\Gamma \leq 1.8$ Å are "safe" in the sense that the excitation energy in question is is unlikely to be seriously affected by TD-DFT's underestimation of long-range CT energies. [397] A trust radius $\Gamma \leq 2.4$ Å is suggested for global hybrid functionals with $C_{\text{HFX}} = 0.2$–0.3, again with Γ evaluated using NTOs. [397] For long-range excitations well beyond 2.0 Å, it is suggested that the use of either LRC functionals, or else global hybrids with $C_{\text{HFX}} \geq 0.33$, is mandatory. [25] As an alternative, the close connection between Γ and $\tilde{d}_{\text{CD}}$ suggests that the latter might also provide a reliability metric for TD-DFT excitation energies, while at the same time affording a physically interpretable (and representation-invariant) numerical value to quantify how charge moves ($d_{\text{e-h}}^-$) and spreads (d_{exc}) upon excitation. The precise trust radius to use in conjunction with $\tilde{d}_{\text{CD}}$ remains to be determined.

Lastly, a "Mulliken-averaged configuration index" (MAC) has been suggested for detecting spurious low-energy CT states. [388,398] A Koopmans-style approximation for long-range electron transfer from ψ_i to ψ_a,

$$\text{IE} + \text{EA} \approx -(\varepsilon_i + \varepsilon_a) , \qquad (6.17)$$

in conjunction with Mulliken's asymptotic formula for ω_{CT} [eqn. (6.2)], suggests a definition

$$\omega_{\text{MAC}} = \frac{-\sum_{ia} x_{ia}(\varepsilon_i + \varepsilon_a)}{\sum_{jb} x_{jb}^2} - \frac{1}{d_{\text{e-h}}^-} . \qquad (6.18)$$

(This is a slightly modified version of the metric called M_{AC} in

Ref. 398, replacing $\sum_{jb} x_{jb}$ in the denominator with $\sum_{jb} x_{jb}^2$, and substituting $d_{\text{e-h}}^-$ for D_{CT}.) The idea is that if $\omega < \omega_{\text{MAC}}$, where ω is the TD-DFT excitation energy, then the excited state in question is likely a "ghost" CT state and should not be taken at face value.[398] However, this metric should only be used for large values of $d_{\text{e-h}}^-$, because Mulliken's formula only makes sense for large donor–acceptor separation. Given the crudeness of the approximation in eqn. (6.17), it is also unclear how robust this metric will be. Proper statistical measures of electron–hole correlation seem preferable as means to define boundaries for trustworthiness in TD-DFT calculations.

7 Summary

TD-DFT is the workhorse method of computational electronic spectroscopy and is widely used by both computational and experimental chemists and materials scientists. Visualizing TD-DFT excitations in terms of NTOs, as a conceptually superior alternative to canonical MOs, has become standard practice but other visualization tools are also available and the connections amongst them are not always obvious to beginning users. The present work provides a theoretical foundation to understand how the NTOs relate to other common visualization tools including attachment and detachment densities, which are densities for the excited electron and the hole, respectively. Atomic or fragment-based partitions of $\Delta\rho(\mathbf{r})$, and quantitative measures of exciton size and electron–hole separation, have been introduced rigorously herein, and demonstrated with numerous examples. Emphasis has been placed on understanding how various tools relate to one another, as previous literature has not always been clear in this regard.

CT numbers $\Omega_{A \to B}$, which quantify electron flow from moiety A to B upon excitation, are a particularly useful atomic or functional-group partition. Arranged in the form of a matrix $\mathbf{\Omega}$, these quantities provides a simple visual representation of the transition density kernel $T(\mathbf{r}_{\text{hole}}, \mathbf{r}_{\text{elec}})$ that has sometimes been described as an "exciton wave function". Heat maps of the matrix $\mathbf{\Omega}$ provide an easy way to distinguish localized versus delocalized excited states, or the presence of charge-separated character, even in centrosymmetric systems where symmetry prevents CT from manifesting as a change in dipole moment. Fragment-based analysis of $T(\mathbf{r}_{\text{hole}}, \mathbf{r}_{\text{elec}})$ can distinguish between delocalization caused by excitonic coupling, versus delocalization due to charge separation, possibilities that are not mutually exclusive but also not equivalent. In multichromophore systems, this analysis exposes qualitative differences in the low-energy states obtained using different XC functionals.

A variety of metrics have been discussed that are intended to quantify CT character in a given excitation, an important descriptor in view of TD-DFT's well-known tendency to underestimate long-range CT excitation energies, sometimes to the point of predicting spurious low-lying states in large systems.[1] Some of these CT metrics have more desirable properties than others, such as correct normalization and invariance to unitary transformations of the MOs. The present work advocates for the use of direct measures of exciton size that correspond to well-defined expectation values, rather than *ad hoc* constructions. The for-

mer include the RMS electron–hole separation (d_{exc}), which is expressed in terms of the particle and hole densities $\Delta\rho_{\text{elec}}(\mathbf{r})$ and $\Delta\rho_{\text{hole}}(\mathbf{r})$. The mean separation between the centroids of those quantities ($d_{\text{e-h}}^-$) can also be used, although it vanishes in centrosymmetric systems. In such cases, a charge-displacement metric (d_{CD} or $\tilde{d}_{\text{CD}}$) can be used instead. These quantities are directly interpretable and readily computable using third-party software,[162,209,399,400] based on formatted output from various electronic structure programs. The TheoDORE program is especially recommended,[209] as it implements various measures of exciton size that are grounded in proper expectation values, as well as CT numbers $\Omega_{A \to B}$ that properly account for non-orthogonality of the AO basis functions. Much of this functionality exists in the Q-Chem program also,[401] without the need for third-party software. The author hopes that this Perspective will lead to better understanding and more erudite discussion of precisely what is being visualized or quantified when discussing the output of TD-DFT calculations.

Conflicts of interest

J.M.H. serves on the board of directors of Q-Chem Inc.

Acknowledgements

References

1 J. M. Herbert, Density-functional theory for electronic excited states, in *Theoretical and Computational Photochemistry: Fundamentals, Methods, Applications and Synergy with Experimental Approaches*, ed. C. García-Iriepa and M. Marazzi; Elsevier, Amsterdam, 2023; chapter 3, pp. 69–118.

2 M. E. Casida, Time-dependent density functional response theory for molecules, in *Recent Advances in Density Functional Methods, Part I*, ed. D. P. Chong, Vol. I of *Recent Advances in Computational Chemistry;* World Scientific, River Edge, NJ, 1995; chapter 5, pp. 155–192.

3 S. Hirata and M. Head-Gordon, Time-dependent density functional theory within the Tamm-Dancoff approximation, *Chem. Phys. Lett.*, 1999, **314**, 291–299.

4 F. Furche, On the density matrix based approach to time-dependent density functional response theory, *J. Chem. Phys.*, 2001, **114**, 5982–5992.

5 C. Ullrich, *Time-Dependent Density-Functional Theory: Concepts and Applications*, Oxford University Press, New York, 2012.

6 M. E. Casida, Time-dependent density-functional theory for molecules and molecular solids, *J. Mol. Struct. (Theochem)*, 2009, **914**, 3–18.

7 P. Elliott, F. Furche, and K. Burke, Excited states from time-dependent density functional theory, in *Reviews in Computational Chemistry*, ed. K. B. Lipkowitz and T. R. Cundari, Vol.

26; Wiley-VCH, New York, 2009; chapter 3, pp. 91–165.

8   F. Furche and D. Rappoport, Density functional methods for excited states: Equilibrium structure and electronic spectra, in *Computational Photochemistry*, ed. M. Olivucci, Vol. 16 of *Theoretical and Computational Chemistry;* Elsevier, Amsterdam, 2005; chapter 3, pp. 93–128.

9   A. Dreuw and M. Head-Gordon, Single-reference ab initio methods for the calculation of excited states of large molecules, *Chem. Rev.*, 2005, **105**, 4009–4037.

10 M. R. Silva-Junior, M. Schreiber, S. P. A. Sauer, and W. Thiel, Benchmarks for electronically excited states: Time-dependent density functional theory and density functional theory based multireference configuration interaction, *J. Chem. Phys.*, 2008, **129**, 104103.

11 S. S. Leang, F. Zahariev, and M. S. Gordon, Benchmarking the performance of time-dependent density functional methods, *J. Chem. Phys.*, 2012, **136**, 104101.

12 A. D. Laurent and D. Jacquemin, TD-DFT benchmarks: A review, *Int. J. Quantum Chem.*, 2013, **113**, 2019–2039.

13 J. Kim, K. Hong, S.-Y. Hwang, S. Ryu, S. Choi, and W. Y. Kim, Effects of the locality of a potential derived from hybrid density functionals on Kohn–Sham orbitals and excited states, *Phys. Chem. Chem. Phys.*, 2017, **19**, 10177–10186.

14 J. Liang, X. Feng, D. Hait, and M. Head-Gordon, Revisiting the performance of time-dependent density functional theory for electronic excitations: Assessment of 43 popular and recently developed functionals from rungs one to four, *J. Chem. Theory Comput.*, 2022, **18**, 3460–3473.

15 J. M. Herbert, Y. Zhu, B. Alam, and A. K. Kumar, Time-dependent density functional theory for x-ray absorption spectra: Comparing the real-time approach to linear response, *J. Chem. Theory Comput.*, 2023, **19**, 6745–6760.

16 T. Etienne, X. Assfeld, and A. Monari, Toward a quantitative assessment of electron transitions' charge-transfer character, *J. Chem. Theory Comput.*, 2014, **10**, 3896–3905.

17 T. Etienne, Theoretical insights into the topology of molecular excitons from single-reference excited states calculation methods, in *Excitons*, ed. S. L. Pyshkin; IntechOpen, 2018; chapter 3, pp. 31–54.

18 F. Plasser, M. Wormit, and A. Dreuw, New tools for the systematic analysis and visualization of electronic excitations. I. Formalism, *J. Chem. Phys.*, 2014, **140**, 024106.

19 F. Plasser, S. A. Bäppler, M. Wormit, and A. Dreuw, New tools for the systematic analysis and visualization of electronic excitations. II. Applications, *J. Chem. Phys.*, 2014, **141**, 024107.

20 S. A. Mewes and A. Dreuw, Density-based descriptors and exciton analyses for visualizing and understanding the electronic structure of excited states, *Phys. Chem. Chem. Phys.*, 2019, **21**, 2843–2856.

21 P. Kimber and F. Plasser, Classification and analysis of molecular excited states, in *Comprehensive Computational Chemistry*, ed. M. Yáñeez and R. J. Boyd, Vol. 4; Elsevier, Oxford, first ed., 2024; pp. 55–83.

22 F. Plasser, B. Thomitzni, S. A. Bäppler, J. Wenzel, D. R. Rehn, M. Wormit, and A. Dreuw, Statistical analysis of electronic excitation processes: Spatial location, compactness, charge transfer, and electron-hole correlation, *J. Comput. Chem.*, 2015, **36**, 1609–1620.

23 M. J. G. Peach, P. Benfield, T. Helgaker, and D. J. Tozer, Excitation energies in density functional theory: An evaluation and a diagnostic test, *J. Chem. Phys.*, 2008, **128**, 044118.

24 D. Jacquemin, T. Le Bahers, C. Adamo, and I. Ciofini, What is the "best" atomic charge model to describe through-space charge-transfer excitations?, *Phys. Chem. Chem. Phys.*, 2012, **14**, 5383–5388.

25 C. A. Guido, P. Cortona, B. Mennucci, and C. Adamo, On the metric of charge transfer molecular excitations: A simple chemical descriptor, *J. Chem. Theory Comput.*, 2013, **9**, 3118–3126.

26 M. Savarese, C. A. Guido, E. Brémond, I. Ciofini, and C. Adamo, Metrics for molecular electronic excitations: A comparison between orbital- and density-based descriptors, *J. Phys. Chem. A*, 2017, **121**, 7543–7549.

27 S. Mai, F. Plasser, J. Dorn, M. Fumanal, C. Daniel, and L. González, Quantitative wave function analysis for excited states of transition metal complexes, *Coord. Chem. Rev.*, 2018, **361**, 74–97.

28 R. J. Magyar and S. Tretiak, Dependence of spurious charge-transfer excited states on orbital exchange in TDDFT: Large molecules and clusters, *J. Chem. Theory Comput.*, 2007, **3**, 976–987.

29 A. W. Lange and J. M. Herbert, Both intra- and interstrand charge-transfer excited states in B-DNA are present at energies comparable to, or just above, the $^1\pi\pi^*$ excitonic bright states, *J. Am. Chem. Soc.*, 2009, **131**, 3913–3922.

30 A. Lange and J. M. Herbert, Simple methods to reduce charge-transfer contamination in time-dependent density-functional calculations of clusters and liquids, *J. Chem. Theory Comput.*, 2007, **3**, 1680–1690.

31 A. W. Lange, M. A. Rohrdanz, and J. M. Herbert, Charge-transfer excited states in a π-stacked adenine dimer, as predicted using long-range-corrected time-dependent density functional theory, *J. Phys. Chem. B*, 2008, **112**, 6304–6308. Erratum: *J. Phys. Chem. B*, 2008, **112**, 7345.

32 C. M. Isborn, B. D. Mar, B. F. E. Curchod, I. Tavernelli, and T. J. Martínez, The charge transfer problem in density functional theory calculations of aqueously solvated molecules, *J. Phys. Chem. B*, 2013, **117**, 12189–12201.

33 N. T. Maitra, Charge-transfer in time-dependent density functional theory, *J. Phys.: Condens. Matt.*, 2017, **29**, 423001.

34 D. J. Tozer, R. D. Amos, N. C. Handy, B. O. Roos, and L. Serrano-Andrés, Does density functional theory contribute to the understanding of excited states of unsaturated organic compounds?, *Mol. Phys.*, 1999, **97**, 859–868.

35 A. Dreuw, J. L. Weisman, and M. Head-Gordon, Long-range charge-transfer excited states in time-dependent density functional theory require non-local exchange, *J. Chem.*

Phys., 2003, **119**, 2943–2946.

36 O. Gritsenko and E. J. Baerends, Asymptotic correction of the exchange–correlation kernel of time-dependent density functional theory for long-range charge-transfer excitations, *J. Chem. Phys.*, 2004, **121**, 655–660.

37 T. Stein, L. Kronik, and R. Baer, Reliable prediction of charge transfer excitations in molecular complexes using time-dependent density functional theory, *J. Am. Chem. Soc.*, 2009, **131**, 2818–2820.

38 R. Baer, E. Livshits, and U. Salzner, Tuned range-separated hybrids in density functional theory, *Annu. Rev. Phys. Chem.*, 2010, **61**, 85–109.

39 S. Kümmel, Charge-transfer excitations: A challenge for time-dependent density functional theory that has been met, *Adv. Energy Mater.*, 2017, **7**, 1700440.

40 Y. Tawada, T. Tsuneda, S. Yanagisawa, T. Yanai, and K. Hirao, A long-range corrected time-dependent density functional theory, *J. Chem. Phys.*, 2004, **120**, 8425–8433.

41 M. A. Rohrdanz and J. M. Herbert, Simultaneous benchmarking of ground- and excited-state properties with long-range-corrected density functional theory, *J. Chem. Phys.*, 2008, **129**, 034107.

42 M. A. Rohrdanz, K. M. Martins, and J. M. Herbert, A long-range-corrected density functional that performs well for both ground-state properties and time-dependent density functional theory excitation energies, including charge-transfer excited states, *J. Chem. Phys.*, 2009, **130**, 054112.

43 S. Refaely-Abramson, R. Baer, and L. Kronik, Fundamental and excitation gaps in molecules of relevance for organic photovoltaics from an optimally tuned range-separated hybrid functional, *Phys. Rev. B*, 2011, **84**, 075144.

44 S. Refaely-Abramson, M. Jain, S. Sharifzadeh, J. B. Neaton, and L. Kronik, Solid-state optical absorption from optimally tuned time-dependent range-separated hybrid density functional theory, *Phys. Rev. B*, 2015, **92**, 081204(R).

45 A. K. Manna, A. Refaely-Abramson, A. M. Reilly, A. Tkatchenko, J. B. Neaton, and L. Kronik, Quantitative prediction of optical absorption in molecular solids from an optimally tuned screened range-separated hybrid functional, *J. Chem. Theory Comput.*, 2018, **14**, 2919–2929.

46 B. Alam, A. F. Morrison, and J. M. Herbert, Charge separation and charge transfer in the low-lying excited states of pentacene, *J. Phys. Chem. C*, 2020, **124**, 24653–24666.

47 T. Yanai, D. P. Tew, and N. C. Handy, A new hybrid exchange-correlation functional using the Coulomb-attenuating method (CAM-B3LYP), *Chem. Phys. Lett.*, 2004, **393**, 51–57.

48 M. Modrzejewski, Ł. Rajchel, G. Chalasinski, and M. M. Szczesniak, Density-dependent onset of the long-range exchange: A key to donor–acceptor properties, *J. Phys. Chem. A*, 2013, **117**, 11580–11586.

49 M. Haasler, T. M. Maier, R. Grotjahn, S. Gückel, A. V. Arbuznikov, and M. Kaupp, A local hybrid functional with wide applicability and good balance between (de)localization and left–right correlation, *J. Chem. Theory Comput.*, 2020, **16**,

5645–5657.

50 S. Fürst, M. Haasler, R. Grotjahn, and M. Kaupp, Full implementation, optimization, and evaluation of a range-separated local hybrid functional with wide accuracy for ground and excited states, *J. Chem. Theory Comput.*, 2023, **19**, 488–502.

51 S. Fürst and M. Kaupp, Accurate ionization potentials, electron affinities, and band gaps from the *ω*LH22t range-separated local hybrid functional: No tuning required, *J. Chem. Theory Comput.*, 2023, **19**, 314–3158.

52 M. Head-Gordon, A. M. Graña, D. Maurice, and C. A. White, Analysis of electronic transitions as the difference of electron attachment and detachment densities, *J. Phys. Chem.*, 1995, **99**, 14261–14270.

53 K. Yabana, T. Nakatsukasa, J.-I. Iwata, and G. F. Bertsch, Real-time, real-space implementation of the linear response time-dependent density functional theory, *Phys. Stat. Sol. B*, 2006, **243**, 1121–1138.

54 M. R. Provorse and C. M. Isborn, Electron dynamics with real-time time-dependent density functional theory, *Int. J. Quantum Chem.*, 2016, **116**, 739–749.

55 X. Li, N. Govind, C. Isborn, A. E. DePrince III, and K. Lopata, Real-time time-dependent electronic structure theory, *Chem. Rev.*, 2020, **120**, 9951–9993.

56 Y. Kawashita, T. Nakatsukasa, and K. Yabana, Time-dependent density-functional theory simulation for electron-ion dynamics in molecules under intense laser pulses, *J. Phys.: Condens. Matt.*, 2009, **21**, 064222.

57 K. Yabana, T. Sugiyama, Y. Shinohara, T. Otobe, and G. F. Bertsch, Time-dependent density functional theory for strong electromagnetic fields in crystalline solids, *Phys. Rev. B*, 2012, **85**, 045134.

58 C. A. Ullrich and A. D. Bandrauk, Atoms and molecules in strong laser fields, in *Fundamentals of Time-Dependent Density Functional Theory*, ed. M. A. L. Marques, N. T. Maitra, F. M. S. Nogueira, E. K. U. Gross, and A. Rubio, Vol. 837 of *Lecture Notes in Physics;* Springer-Verlag, Berlin, 2012; chapter 18, pp. 351–371.

59 U. De Giovannini, G. Brunetto, A. Castro, J. Walkenhorst, and A. Rubio, Simulating pump–probe photoelectron and absorption spectroscopy on the attosecond timescale with time-dependent density functional theory, *ChemPhysChem*, 2013, **14**, 1363–1376.

60 Y. Miyamoto, H. Zhang, X. L. Cheng, and A. Rubio, Modeling of laser-pulse induced water decomposition on two-dimensional materials by simulations based on time-dependent density functional theory, *Phys. Rev. B*, 2017, **96**, 115451.

61 F. Bedurke, T. Klamroth, and P. Saalfrank, Many-electron dynamics in laser-driven molecules: Wavefunction theory *vs.* density functional theory, *Phys. Chem. Chem. Phys.*, 2021, **23**, 13544–13560.

62 Y. Zhu and J. M. Herbert, High harmonic spectra computed using time-dependent Kohn-Sham theory with Gaussian or-

bitals and a complex absorbing potential, *J. Chem. Phys.*, 2022, **156**, 204123.

63 E. Coccia and E. Luppi, Time-dependent *ab initio* approaches for high-harmonic generation spectroscopy, *J. Phys.: Condens. Matt.*, 2022, **34**, 073001.

64 Y. H. Li and C. A. Ullrich, The particle-hole map: A computational tool to visualize electronic excitations, *J. Chem. Theory Comput.*, 2015, **11**, 5838–5852.

65 M. Repisky, L. Konecny, M. Kadek, S. Komorovsky, O. L. Malkin, V. G. Malkin, and K. Ruud, Excitation energies from real-time propagation of the four-component Dirac-Kohn-Sham equation, *J. Chem. Theory Comput.*, 2015, **11**, 980–991.

66 A. Bruner, D. LaMaster, and K. Lopata, Accelerated broad-band spectra using transition dipole decomposition and Padé approximants, *J. Chem. Theory Comput.*, 2016, **12**, 3741–3750.

67 T. P. Rossi, M. Kuisma, M. J. Puska, R. M. Nieminen, and P. Erhart, Kohn-Sham decomposition in real-time time-dependent density-functional theory: An efficient tool for analyzing plasmonic excitations, *J. Chem. Theory Comput.*, 2017, **13**, 4779–4790.

68 R. Sinha-Roy, P. García-González, X. L. Lozano, R. L. Whetten, and H.-C. Weissker, Identifying electronic modes by Fourier transform from δ-kick time-evolution TDDFT calculations, *J. Chem. Theory Comput.*, 2018, **14**, 6417–6426.

69 A. Parise, A. Alvarez-Ibarra, X. Wu, X. Zhao, J. Pilmé, and A. de la Lande, Quantum chemical topology of the electron localization function in the field of attosecond electron dynamics, *J. Phys. Chem. Lett.*, 2018, **9**, 844–850.

70 W. Koch and M. C. Holthausen, *A Chemist's Guide to Density Functional Theory*, Wiley-VCH, New York, 2nd ed., 2001.

71 H. Weiss, R. Ahlrichs, and M. Häser, A direct algorithm for self-consistent-field linear response theory and application to C_{60}: Excitation energies, oscillator strengths, and frequency-dependent polarizabilities, *J. Chem. Phys.*, 1993, **99**, 1262–1270.

72 A. V. Luzanov and O. A. Zhikol, Electron invariants and excited state structural analysis for electronic transitions within CIS, RPA, and TDDFT models, *Int. J. Quantum Chem.*, 2010, **110**, 902–924.

73 T. Etienne, Transition matrices and orbitals from reduced density matrix theory, *J. Chem. Phys.*, 2015, **142**, 244103.

74 T. Etienne, A comprehensive, self-contained derivation of the one-body density matrices from single-reference excited-state calculation methods using the equation-of-motion formalism, *Int. J. Quantum Chem.*, 2020, **120**, e26110.

75 N. Ullah and D. J. Rowe, Properties of real RPA matrices and a simple diagonalization procedure, *Nucl. Phys. A,* 1971, **A163**, 257–264.

76 M. Grüning, A. Marini, and X. Gonze, Exciton-plasmon states in nanoscale materials: Breakdown of the Tamm–Dancoff approximation, *Nano Lett.*, 2009, **9**, 2820–2824.

77 Y.-M. Byun and C. A. Ullrich, Excitons in solids from time-dependent density-functional theory: Assessing the Tamm-Dancoff approximation, *Computation*, 2017, **5**, 9.

78 H. Eshuis, J. E. Bates, and F. Furche, Electron correlation methods based on the random phase approximation, *Theor. Chem. Acc.*, 2012, **131**, 1084.

79 A. Heßelmann and A. Görling, Random-phase approximation correlation methods for molecules and solids, *Mol. Phys.*, 2011, **109**, 2473–2500.

80 X. Ren, P. Rinke, C. Joas, and M. Scheffler, Random-phase approximation and its applications in computational chemistry and materials science, *J. Mater. Sci.*, 2012, **47**, 7447–7471.

81 G. P. Chen, V. K. Voora, M. M. Agee, S. G. Balasubramani, and F. Furche, Random-phase approximation methods, *Annu. Rev. Phys. Chem.*, 2017, **68**, 421–445.

82 M. J. G. Peach, M. J. Williamson, and D. J. Tozer, Influence of triplet instabilities in TDDFT, *J. Chem. Theory Comput.*, 2011, **7**, 3578–3585.

83 M. J. G. Peach and D. J. Tozer, Overcoming low orbital overlap and triplet instability problems in TDDFT, *J. Phys. Chem. A*, 2012, **116**, 9783–9789.

84 M. J. G. Peach, N. Warner, and D. J. Tozer, On the triplet instability in TDDFT, *Mol. Phys.*, 2013, **111**, 1271–1274.

85 C. Y. Cheng, M. S. Ryley, M. J. G. Peach, D. J. Tozer, T. Helgaker, and A. M. Teale, Molecular properties in the Tamm–Dancoff approximation: Indirect nuclear spin–spin coupling constants, *Mol. Phys.*, 2015, **113**, 1937–1951.

86 R. Bauernschmitt and R. Ahlrichs, Stability analysis for solutions of the closed shell Kohn–Sham equation, *J. Chem. Phys.*, 1996, **104**, 9047–9052.

87 M. E. Casida, A. Ipatov, and F. Cordova, Linear-response time-dependent density functional theory for open-shell molecules, in *Time-Dependent Density Functional Theory*, ed. M. A. L. Marques, C. A. Ullrich, F. Nogueira, A. Rubio, K. Burke, and E. K. U. Gross, Vol. 706 of *Lecture Notes in Physics;* Springer-Verlag, Berlin, 2006; chapter 16, pp. 243–257.

88 F. Cordova, L. J. Doriol, A. Ipatov, M. E. Casida, C. Filippi, and A. Vela, Troubleshooting time-dependent density-functional theory for photochemical applications: Oxirane, *J. Chem. Phys.*, 2007, **127**, 164111.

89 E. Tapavicza, I. Tavernelli, U. Rothlisberger, C. Filippi, and M. E. Casida, Mixed time-dependent density-functional theory/classical trajectory surface hopping study of oxirane photochemistry, *J. Chem. Phys.*, 2008, **129**, 124108.

90 J. D. Goddard and G. Orlova, Density functional theory with fractionally occupied frontier orbitals and the instabilities of the Kohn–Sham solutions for defining radical transition states: Ring-opening reactions, *J. Chem. Phys.*, 1999, **111**, 7705–7712.

91 G. Orlova and J. D. Goddard, Singularities in the behavior of density functionals in predictions of singlet biradicals: The 1,2-dichalcogenins, *J. Chem. Phys.*, 2000, **112**, 10085–10094.

92 G. Orlova and J. D. Goddard, Is density functional theory

free of spatial symmetry breaking? The case of the linear carbon radical cations: C_3^+, C_5^+, C_7^+, and C_9^+, *Chem. Phys. Lett.*, 2002, **363**, 486–491.

93 G. Orlova and J. D. Goddard, Practical failures from the inclusion of exact exchange: How much exact exchange is appropriate?, *Mol. Phys.*, 2002, **100**, 483–497.

94 F. Furche and R. Ahlrichs, Adiabatic time-dependent density functional methods for excited state properties, *J. Chem. Phys.*, 2002, **117**, 7433–7447. Erratum, *J. Chem. Phys.*, 2004, **121**, 12772–12773.

95 O. B. Lutnæs, T. Helgaker, and M. Jaszuński, Spin–spin coupling constants and triplet instabilities in Kohn–Sham theory, *Mol. Phys.*, 2010, **108**, 2579–2590.

96 G. Cui and W. Yang, Challenges with range-separated exchange-correlation functionals in time-dependent density functional theory calculations, *Mol. Phys.*, 2010, **108**, 2745–2750.

97 J. S. Sears, T. Koerzdoerfer, C.-R. Zhang, and J.-L. Brédas, Communication: Orbital instabilities and triplet states from time-dependent density functional theory and long-range corrected functionals, *J. Chem. Phys.*, 2011, **135**, 151103.

98 O. S. Bokareva, G. Grell, S. I. Bokarev, and O. Kühn, Tuning range-separated density functional theory for photocatalytic water splitting systems, *J. Chem. Theory Comput.*, 2015, **11**, 1700–1709.

99 A. Savin, C. J. Umrigar, and X. Gonze, Relationship of Kohn–Sham eigenvalues to excitation energies, *Chem. Phys. Lett.*, 1998, **288**, 391–395.

100 M. Petersilka, E. K. U. Gross, and K. Burke, Excitation energies from time-dependent density functional theory using exact and approximate potentials, *Int. J. Quantum Chem.*, 2000, **80**, 534–554.

101 E. J. Baerends, O. V. Gritsenko, and R. van Meer, The Kohn–Sham gap, the fundamental gap and the optical gap: The physical meaning of occupied and virtual Kohn–Sham orbital energies, *Phys. Chem. Chem. Phys.*, 2013, **15**, 16408–16425.

102 R. van Meer, O. V. Gritsenko, and E. J. Baerends, Physical meaning of virtual Kohn–Sham orbitals and orbital energies: An ideal basis for the description of molecular excitations, *J. Chem. Theory Comput.*, 2014, **10**, 4432–4441.

103 J. Kim, K. Hong, S. Choi, S.-Y. Hwang, and W. Y. Kim, Configuration interaction singles based on the real-space numerical grid method: Kohn–Sham *versus* Hartree–Fock orbitals, *Phys. Chem. Chem. Phys.*, 2015, **17**, 31434–31443.

104 S. Kang, J. Woo, J. Kim, H. Kim, Y. Kim, J. Lim, S. Choi, and W. Y. Kim, ACE-Molecule: An open-source real-space quantum chemistry package, *J. Chem. Phys.*, 2020, **152**, 124110.

105 A. Szabo and N. S. Ostlund, *Modern Quantum Chemistry*, Macmillan, New York, 1982.

106 J. M. Herbert, The quantum chemistry of loosely-bound electrons, in *Reviews in Computational Chemistry*, ed. A. L. Parill and K. Lipkowitz, Vol. 28; Wiley-VCH, Hoboken, 2015; chapter 8, pp. 391–517.

107 D. Escudero, A. D. Laurent, and D. Jacquemin, Time-dependent density functional theory: A tool to explore excited states, in *Handbook of Computational Chemistry*, ed. J. Leszczynski, A. Kaczmarek-Kedziera, T. Puzyn, M. G. Papadopoulos, H. Reis, and M. K. Shukla; Springer International Publishing, Switzerland, second ed., 2017; chapter 21, pp. 927–961.

108 F. Maschietto, M. Campetella, M. J. Frisch, G. Scalmani, C. Adamo, and I. Ciofini, How are the charge transfer descriptors affected by the quality of the underpinning electronic density?, *J. Comput. Chem.*, 2018, **39**, 735–742.

109 A. Ipatov, F. Cordova, L. J. Doriol, and M. E. Casida, Excited-state spin-contamination in time-dependent density-functional theory for molecules with open-shell ground states, *J. Mol. Struct. (Theochem)*, 2009, **914**, 60–73.

110 D. Rappoport and J. Hutter, Excited-state properties and dynamics, in *Fundamentals of Time-Dependent Density Functional Theory*, ed. M. A. L. Marques, N. T. Maitra, F. M. S. Nogueira, E. K. U. Gross, and A. Rubio, Vol. 837 of *Lecture Notes in Physics;* Springer-Verlag, Berlin, 2012; chapter 16, pp. 317–336.

111 I. Franco and S. Tretiak, Electron-vibrational dynamics of photoexcited polyfluorenes, *J. Am. Chem. Soc.*, 2004, **126**, 12130–12140.

112 P. R. Surján, Natural orbitals in CIS and singular-value decomposition, *Chem. Phys. Lett.*, 2007, **439**, 393–394.

113 E. Ronca, C. Angeli, L. Belpassi, F. De Angelis, F. Tarantelli, and M. Pastore, Density relaxation in time-dependent density functional theory: Combining relaxed density natural orbitals and multireference perturbation theories for an improved description of excited states, *J. Chem. Theory Comput.*, 2014, **10**, 4014–4024.

114 K. N. Walzl, C. F. Koerting, and A. Kuppermann, Electron-impact spectroscopy of acetaldehyde, *J. Chem. Phys.*, 1987, **87**, 3796–3803.

115 D. E. Freeman, J. R. Lombardi, and W. Klemperer, Electric dipole moment of the lowest singlet π^* state of propynal, *J. Chem. Phys.*, 1966, **45**, 58–60.

116 S. Millefiori, G. Favini, A. Millefiori, and D. Grasso, Electronic spectra and structure of nitroanilines, *Spectrochim. Acta A*, 1977, **33**, 21–27.

117 B. H. Smith, A. Buonaugurio, J. Chen, E. Collins, K. H. Bowen, R. N. Compton, and T. Sommerfeld, Negative ions of p-nitroaniline: Photodetachment, collisions, and *ab initio* calculations, *J. Chem. Phys.*, 2013, **138**, 234304.

118 J. B. Foresman, M. Head-Gordon, J. A. Pople, and M. J. Frisch, Toward a systematic molecular orbital theory for excited states, *J. Phys. Chem.*, 1992, **96**, 135–149.

119 H. K. Sinha and K. Yates, On the ground and excited state dipole moments of planar vs. twisted nitroaniline analogues, *Can. J. Chem.*, 1991, **69**, 550–557.

120 R. L. Martin, Natural transition orbitals, *J. Chem. Phys.*, 2003, **118**, 4775–4777.

121 A. V. Luzanov, A. A. Sukhorukov, and V. E. Umanskii, Application of transition density matrix for analysis of excited states, *Theor. Exp. Chem.*, 1974, **10**, 354–361.

122 A. V. Luzanov and V. F. Pedash, Interpretation of excited states using charge-transfer numbers, *Theor. Exp. Chem.*, 1980, **15**, 338–341.

123 I. Mayer, Using singular value decomposition for a compact presentation and improved interpretation of the CIS wave functions, *Chem. Phys. Lett.*, 2007, **437**, 284–286.

124 P.-O. Löwdin, Quantum theory of many-particle systems. I. Physical interpretation by means of density matrices, natural spin-orbitals, and convergence problems in the method of configuration interaction, *Phys. Rev.*, 1955, **97**, 1474–1489.

125 P.-O. Löwdin and H. Shull, Natural orbitals in the quantum theory of two-electron systems, *Phys. Rev.*, 1956, **101**, 1730–1739.

126 V. I. Minkin, Glossary of terms used in theoretical organic chemistry, *Pure Appl. Chem.*, 1999, **71**, 1919–1981.

127 L. M. Thompson, H. Harb, and H. P. Hratchian, Natural ionization orbitals for interpreting electron detachment processes, *J. Chem. Phys.*, 2016, **144**, 204117.

128 F. Weinhold, Natural bond orbital methods, in *Encyclopedia of Computational Chemistry*, ed. P. v. R. Schleyer, P. R. Schreiner, N. L. Allinger, T. Clark, J. Gasteiger, P. Kollman, and H. F. Schaefer III, Vol. 3; Wiley, 1998; pp. 1792–1811.

129 F. Weinhold and C. R. Landis, *Valency and Bonding*, Cambridge University Press, Cambridge, UK, 2005.

130 E. D. Glendening, C. R. Landis, and F. Weinhold, Natural bond orbital methods, *Wiley Interdiscip. Rev.: Comput. Mol. Sci.*, 2012, **2**, 1–42.

131 A. T. Amos and G. G. Hall, Single determinant wave functions, *Proc. R. Soc. Lond. A*, 1961, **263**, 483–493.

132 H. F. King, R. E. Stanton, H. Kim, R. E. Wyatt, and R. G. Parr, Corresponding orbitals and the nonorthogonality problem in molecular quantum mechanics, *J. Chem. Phys.*, 1967, **47**, 1936–1941.

133 A. F. Morrison, Z.-Q. You, and J. M. Herbert, Ab initio implementation of the Frenkel-Davydov exciton model: A naturally parallelizable approach to computing collective excitations in crystals and aggregates, *J. Chem. Theory Comput.*, 2014, **10**, 5366–5376.

134 I.-M. Høyvik, R. H. Myhre, and H. Koch, Correlated natural transition orbitals for core excitation energies in multilevel coupled cluster models, *J. Chem. Phys.*, 2017, **146**, 144109.

135 C.-N. Tsai, M. M. Allard, R. L. Lord, D.-W. Luo, Y.-J. Chen, H. B. Schlegel, and J. F. Endicott, Characterization of low energy charge transfer transitions in (terpyridine)(bipyridine)ruthenium(II) complexes and their cyanide-bridged bi- and tri-metallic analogues, *Inorg. Chem.*, 2011, **50**, 11965–11977.

136 S. Ling, S. Schumacher, I. Galbraith, and M. J. Paterson, Excited-state absorption of conjugated polymers in the near-infrared and visible: A computational study of oligofluorenes, *J. Phys. Chem. A*, 2013, **117**, 6889–6895.

137 S. Prager, A. Zech, T. A. Wesolowski, and A. Dreuw, Implementation and application of the frozen density embedding theory with the algebraic diagrammatic construction scheme

138 Z. Lin and T. Van Voorhis, Triplet tuning: A novel family of non-empirical exchange–correlation functionals, *J. Chem. Theory Comput.*, 2019, **15**, 1226–1241.

139 T. Zhang, F. Meng, L. Lin, J. Luo, H. Wu, X. Song, C.-Z. Wang, H. Lin, Z. Wang, and S. Zhuo, Theoretical study and experimental validation on the optical emission processes in "free" and "locked" pyrazine derivatives, *Spectrochim. Acta A*, 2019, **223**, 117296.

140 X. Wen, D. S. Graham, D. V. Chulhai, and J. D. Goodpaster, Absolutely localized projection-based embedding for excited states, *J. Chem. Theory Comput.*, 2020, **16**, 385–398.

141 P. Kang, B.-L. Lin, T. A. G. Large, J. Ainsworth, E. C. Wasinger, and T. D. P. Stack, Phenolate-bonded bis(μ-oxido)-bis-copper(II) intermediates: Hydroxylation and dehalogenation reactivities, *Faraday Discuss.*, 2022, **234**, 86–108.

142 M. Hédouin, E. Luppi, O. Ward, D. Harrowven, C. Fressigné, and I. Chataigner, Predictive TDDFT methodology for aromatic molecules UV-vis properties: From benchmark to applications, *ChemistrySelect*, 2023, **8**, e202301943.

143 Z. Wang, J. Liang, and M. Head-Gordon, Earth mover's distance as a metric to evaluate the extent of charge transfer in excitations using discretized real-space densities, *J. Chem. Theory Comput.* 2023, **19**, 7704–7714.

144 L. Mei, J. Hu, X. Cao, F. Wang, C. Zheng, Y. Tao, X. Zhang, and W. Huang, The inductive-effect of electron withdrawing trifluoromethyl for thermally activated delayed fluorescence: Tunable emission from tetra- to penta-carbazole in solution processed blue OLEDs, *Chem. Commun.*, 2015, **51**, 13024–13027.

145 T. Chen, L. Zheng, J. Yuan, Z. An, R. Chen, Y. Tao, H. Li, X. Xie, and W. Huang, Understanding the control of singlet-triplet splitting for organic exciton manipulating: A combined theoretical and experimental approach, *Sci. Rep.*, 2015, **5**, 10923.

146 X. Cai, X. Li, G. Xie, Z. He, K. Gao, K. Liu, D. Chen, Y. Cao, and S.-J. Su, "Rate-limited effect" of reverse intersystem crossing process: The key for tuning thermally activated delayed fluorescence lifetime and efficiency roll-off of organic light emitting diodes, *Chem. Sci.*, 2016, **7**, 4264–4275.

147 R. Chen, Y. Tang, Y. Wan, T. Chen, C. Zheng, Y. Qi, Y. Cheng, and W. Huang, Promoting singlet/triplet exciton transformation in organic optoelectronic molecules: Role of excited state transition configuration, *Sci. Rep.*, 2017, **7**, 6225.

148 Y. Olivier, M. Moral, L. Muccioli, and J.-C. Sancho-García, Dynamic nature of excited states of donor–acceptor TADF materials for OLEDs: How theory can reveal structure–property relationships, *J. Mater. Chem. C*, 2017, **5**, 5718–5729.

149 X. Kong, L. Cai, J. Fan, and L. Lin, Structure-property relationship of phosphine oxide based thermally activated delayed fluorescence molecules: First-principles study, *Org. Electron.*, 2018, **59**, 7–14.

150 R. Ansari, W. Shao, S.-J. Yoon, J. Kim, and J. Kieffer, Charge transfer as the key parameter affecting the color purity of thermally activated delayed fluorescence emitters, *ACS Appl. Mater. Interf.*, 2021, **13**, 28529–28537.

151 S. Xu, Q. Yang, Y. Wan, R. Chen, S. Wang, Y. Si, B. Yang, D. Liu, C. Zheng, and W. Huang, Predicting intersystem crossing efficiencies of organic molecules for efficient thermally activated delayed fluorescence, *J. Mater. Chem. C*, 2019, **7**, 95223–9530.

152 J. Guo, J. Fan, L. Lin, J. Zeng, H. Liu, C.-K. Wang, Z. Zhao, and B. Z. Tang, Mechanical insights into aggregation-induced delayed fluorescence materials with anti-Kasha behavior, *Adv. Sci.*, 2019, **6**, 1801629.

153 R. Dhali, D. K. A. P. Huu, F. Terenziani, C. Sissa, and A. Painelli, Thermally activated delayed fluorescence: A critical assessment of environmental effects on the singlet–triplet energy gap, *J. Chem. Phys.*, 2021, **154**, 134112.

154 C. Leng, S. You, Y. Si, H.-M. Qin, J. Liu, W.-Q. Huang, and K. Li, Unraveling the mechanism of near-infrared thermally activated delayed fluorescence of TPA-based molecules: Effect of hydrogen bond steric hindrance, *J. Phys. Chem. A*, 2021, **125**, 2905–2912.

155 H. Miranda-Salinas, Y.-T. Hung, Y.-S. Chen, D. Luo, H.-C. Kao, C.-H. Chang, K.-T. Wong, and A. Monkman, Controlling through-space charge transfer in bridged D–D′–A TADF emitters, *J. Mater. Chem. C*, 2021, **9**, 8819–8833.

156 C.-Y. Lin, C.-H. Lu, K.-H. Kuo, M. Wang, Y. Tang, Y. Dou, B. Hu, C.-C. Wu, and K.-T. Wong, Highly efficient blue thermally activated fluorescence emitters with a triphenylamine-based macrocyclic donor, *Adv. Opt. Mater.*, 2022, **11**, 2202292.

157 R. Keruckiene, E. Vijaikis, C.-H. Chen, B.-Y. Lin, J.-X. Huang, C.-C. Chu, Y.-C. Dzeng, C. Chen, J.-H. Lee, T.-L. Chiu, S. Macionis, J. Keruckas, R. Butkute, and J. V. Grazulevicius, Power efficiency enhancement of organic light-emitting diodes due to the favorable horizontal orientation of a naphthyridine-based thermally activated delayed fluorescence luminophore, *ACS Appl. Electron. Mater.*, 2023, **5**, 1013–1023.

158 E. Badaeva, V. V. Albert, S. Kilina, A. K. M. Sykora, and S. Tretiak, Effect of deprotonation on absorption and emission spectra of Ru(II)-bpy complexes functionalized with carboxyl groups, *Phys. Chem. Chem. Phys.*, 2010, **12**, 8902–8913.

159 M. Gray and J. M. Herbert, Comprehensive basis-set testing of extended symmetry-adapted perturbation theory and assessment of mixed-basis combinations to reduce cost, *J. Chem. Theory Comput.*, 2022, **18**, 2308–2330.

160 M. Stener, G. Fronzoni, and M. de Simone, Time dependent density functional theory of core electrons excitations, *Chem. Phys. Lett.*, 2003, **373**, 115–123.

161 M. Haranczyk and M. Gutowski, Visualization of molecular orbitals and the related electron densities, *J. Chem. Theory Comput.*, 2008, **4**, 689–693.

162 IQmol, www.iqmol.org (accessed 2023-11-11).

163 H. Ma, T. Qin, and A. Troisi, Electronic excited states in amorphous MEH-PPV polymers from large-scale first principles calculations, *J. Chem. Theory Comput.*, 2014, **10**, 1272–1282.

164 Y. Li, J. Wan, and X. Xu, Theoretical study of the vertical excited states of benzene, pyrimidine, and pyrazine by the symmetry adapted cluster–configuration interaction method, *J. Comput. Chem.*, 2007, **28**, 1658–1667.

165 M. Leclerc, Polyfluorenes: Twenty years of progress, *J. Polym. Sci. A Pol. Chem.*, 2001, **39**, 2867–2873.

166 D. Neher, Polyfluorene homopolymers: Conjugated liquid-crystalline polymers for bright blue emission and polarized electroluminescence, *Macromol. Rapid Commun.*, 2001, **22**, 1365–1385.

167 U. Scherf and E. J. W. List, Semiconducting polyfluorenes—towards reliable structure–property relationships, *Adv. Mater.*, 2002, **14**, 477–487.

168 C. D. Müller, A. Falcou, N. Reckefuss, M. Rojahn, V. Widerhirn, P. Rudati, H. Frohne, O. Nuyken, H. Becker, and K. Meerholz, Multi-colour organic light-emitting displays by solution processing, *Nature*, 2003, **421**, 829–833.

169 *Polyfluorenes*, ed. U. Scherf and D. Neher, Vol. 212 of *Advances in Polymer Science*, Springer-Verlag, Berlin, 2008.

170 L.-H. Xie, S.-H. Yang, J.-Y. Lin, M.-D. Yi, and W. Huang, Fluorene-based macromolecular nanostructures and nanomaterials for organic (opto)electronics, *Phil. Trans. R. Soc. A*, 2012, **371**, 20120337.

171 D. Pugh and J. O. Morley, Molecular hyperpolarizabilities of organic materials, in *Nonlinear Optical Properties of Organic Molecules and Crystals*, ed. D. S. Chemla and J. Zyss, Vol. 1; Academic Press, 1987; chapter II-2, pp. 193–225.

172 I. Mayer, Identifying a pair of interacting chromophores by using SVD transformed CIS wave functions, *Chem. Phys. Lett.*, 2007, **443**, 420–425.

173 H. Uoyama, K. Goushi, K. Shizu, H. Nomura, and C. Adachi, Highly efficient organic light-emitting diodes from delayed fluorescence, *Nature*, 2012, **492**, 234–240.

174 Y. Tao, K. Yuan, T. Chen, P. Xu, H. Li, R. Chen, C. Zheng, L. Zhang, and W. Huang, Thermally activated delayed fluorescence materials towards the breakthrough of organoelectronics, *Adv. Mater.*, 2014, **26**, 7931–7958.

175 P.-Y. Chou, H.-H. Chou, Y.-H. Chen, T.-H. Su, C.-Y. Liao, H.-W. Lin, W.-C. Lin, H.-Y. Yen, I.-C. Chen, and C.-H. Cheng, Efficient delayed fluorescence *via* triplet–triplet annihilation for deep-blue electroluminescence, *Chem. Commun.*, 2014, **50**, 6869–6871.

176 O. Ostroverkhova, Organic optoelectronic materials: Mechanisms and applications, *Chem. Rev.*, 2016, **116**, 13279–13412.

177 T. J. Penfold, F. B. Dias, and A. P. Monkman, The theory of thermally activated delayed fluorescence for organic light emitting diodes, *Chem. Commun.*, 2018, **54**, 3926–3935.

178 J.-H. Li, T. J. Zuehlsdorff, M. C. Payne, and N. D. M. Hine, Identifying and tracing potential energy surfaces of elec-

tronic excitations with specific character *via* their transition origins: Application to oxirane, *Phys. Chem. Chem. Phys.*, 2015, **17**, 12065–12079.

179 A. V. Luzanov and O. A. Zhikol, Collectivity, shell openness indices, and complexity measures of multiconfigurational states: Computations within full CI scheme, *Int. J. Quantum Chem.*, 2005, **104**, 167–180.

180 R. B. Woodward and R. Hoffmann, The conservation of orbital symmetry, *Angew. Chem. Int. Ed. Engl.*, 1969, **8**, 781–853.

181 J. Friedrichs and I. Frank, Mechanism of electrocyclic ring-opening of diphenyloxirane: 40 years after Woodward and Hoffmann, *Angew. Chem. Int. Ed. Engl.*, 2009, **15**, 10825–10829.

182 R. S. Mulliken, Electronic population analysis on LCAO-MO molecular wave functions. I, *J. Chem. Phys.*, 1955, **23**, 1833–1840.

183 S. Huzinaga and S. Narita, Mulliken population analysis and point charge model of molecules, *Isr. J. Chem.*, 1980, **19**, 242–254.

184 S. M. Bachrach, Population analysis and electron densities from quantum mechanics, in *Reviews in Computational Chemistry*, ed. K. Lipkowitz and D. B. Boyd, Vol. 5; Wiley-VCH, Hoboken, 1994; chapter 3, pp. 171–228.

185 M. M. Francl and L. E. Chirlian, The pluses and minuses of mapping atomic charges to electrostatic potentials, in *Reviews in Computational Chemistry*, ed. K. B. Lipkowitz and D. B. Boyd, Vol. 14; Wiley-VCH, New York, 2000; chapter 1, pp. 1–32.

186 R. J. MacDonell, S. Patchkovskii, and M. S. Schuurman, A comparison of partial atomic charges for electronically excited states, *J. Chem. Theory Comput.*, 2022, **18**, 1061–1071.

187 A. V. Luzanov, The structure of the electronic excitation of molecules in quantum-chemical models, *Russ. Chem. Rev.*, 1980, **49**, 1033–1048.

188 A. V. Luzanov, Analysis of the exciton states of polyconjugated systems by the transition density matrix method, *J. Struct. Chem.*, 2002, **43**, 711–720.

189 A. V. Luzanov and O. A. Zhikol, Excited state structural analysis: TDDFT and related models, in *Practical Aspects of Computational Chemistry I: An Overview of the Last Two Decades of Current Trends*, ed. J. Leszczynski and M. K. Shukla; Springer Science + Business Media, 2012; chapter 14, pp. 415–449.

190 D. R. Maurice, *Single Electron Theories of Excited States*, PhD thesis, University of California, Berkeley, CA, 1998.

191 A. F. Morrison, E. Epifanovsky, and J. M. Herbert, Double-buffered, heterogeneous CPU + GPU integral digestion algorithm for single-excitation calculations involving a large number of excited states, *J. Comput. Chem.*, 2018, **39**, 2173–2182.

192 L. Czuchajowski and A. K. Wisor, Electronic effects in multi-bridged cyclophanes as viewed by the indices of excitation, *J. Electron Spectrosc.*, 1987, **43**, 169–181.

193 L. Czuchajowski and A. K. Wisor, Electronic structure of multilayered and multistepped cyclophanes, *J. Mol. Struct. (Theochem)*, 1988, **165**, 163–174.

194 M. Reinhardt, K. Kirschke, and H. Baumann, UV-VIS spectra of some 3-arylazopropenoic acid esters, *J. Mol. Spectrosc.*, 1995, **348**, 417–420.

195 V. G. Mitina, V. V. Ivanov, O. A. Ponomarev, L. A. Sieta, and V. M. Shershukov, Nature of electronic transitions in *N*-phenyl-1,8-naphthalimide and some of its derivatives, *Mol. Eng.*, 1996, **6**, 249–259.

196 A. O. Doroshenko, A. V. Kirichenko, V. G. Mitina, and O. A. Ponomaryov, Spectral properties and dynamics of the excited state structural relaxation of the ortho analogues of POPOP—Effective abnormally large Stokes shift luminophores, *J. Photochem. Photobiol. A*, **94**, 15–26.

197 A. O. Doroshenko, E. A. Posokhov, A. A. Verezubova, and L. M. Ptyagina, Excited state intramolecular proton transfer reaction and luminescent properties of the *ortho*-hydroxy derivatives of 2,5-diphenyl-1,3,4-oxadiazole, *J. Phys. Org. Chem.*, 2000, **13**, 253–265.

198 A. O. Doroshenko, E. A. Posokhov, A. A. Verezubova, L. M. Ptyagina, V. T. Skripkina, and V. M. Shershukov, Radiation-less deactivation of the excited phototautomer form and molecular structure of ESIPT-compounds, *Photochem. Photobiol. Sci.*, 2002, **1**, 92–99.

199 E. Titov, On the low-lying electronically excited states of azobenzene dimers: Transition density matrix analysis, *Molecules*, 2021, **26**, 4245. Erratum: *Molecules*, 2023, **28**, 1370.

200 F. Plasser and H. Lischka, Analysis of excitonic and charge transfer interactions from quantum chemical calculations, *J. Chem. Theory Comput.*, 2012, **8**, 2777–2789.

201 I. Mayer, Charge, bond order and valence in the ab initio SCF theory, *Chem. Phys. Lett.*, 1983, **97**, 270–274.

202 I. Mayer, Bond orders and valences from ab initio wave functions, *Int. J. Quantum Chem.*, 1986, **29**, 477–483.

203 A. A. Voityuk, Fragment transition density method to calculate electronic coupling for excitation energy transfer, *J. Chem. Phys.*, 2014, **140**, 244117.

204 L. Blancafort and A. A. Voityuk, Exciton delocalization, charge transfer, and electronic coupling for singlet excitation energy transfer between stacked nucleobases in DNA: An MS-CASPT2 study, *J. Chem. Phys.*, 2014, **140**, 095102.

205 D. Mester and M. Kállay, Charge-transfer excitations within density functional theory: How accurate are the most recommended approaches?, *J. Chem. Theory Comput.*, 2022, **18**, 1646–1662.

206 P.-O. Löwdin, Quantum theory of cohesive properties of solids, *Adv. Phys.*, 1956, **5**, 1–171.

207 B. C. Carlson and J. M. Keller, Orthogonalization procedures and the localization of Wannier functions, *Phys. Rev.*, 1957, **105**, 102–103.

208 I. Mayer, On Löwdin's method of symmetric orthogonalization, *Int. J. Quantum Chem.*, 2002, **90**, 63–65.

209 F. Plasser, TheoDORE: A toolbox for a detailed and automated analysis of electronic excited state computations,

J. Chem. Phys., 2020, **152**, 084108.

210 K. Rotkiewicz, K. H. Grellmann, and Z. R. Grabowski, Reinterpretation of the anomalous fluorescence of *p*-N,N-dimethylamino-benzonitrile, *Chem. Phys. Lett.*, 1973, **19**, 315–318. Erratum: *Chem. Phys. Lett.*, 1973, **21**, 212.

211 W. Rettig, G. Wermuth, and E. Lippert, Photophysical primary processes in solutions of p-substituted dialkylanilines, *Ber. Bunsenges. Phys. Chem.*, 1979, **83**, 692–697.

212 A. B. J. Parusel, W. Rettig, and W. Sudholt, A comparative theoretical study on DMABN: Significance of excited state optimized geometries and direct comparison of methodologies, *J. Phys. Chem. A*, 2002, **106**, 804–815.

213 W. B. Jensen, The free-electron model: From Otto Schmidt to John Platt, in *Pioneers of Quantum Chemistry*, ed. E. T. Strom and A. K. Wilson, Vol. 1122 of *ACS Symposium Series;* American Chemical Society, 2013; pp. 117–137.

214 J. R. Platt, Classification of spectra of cata-condensed hydrocarbons, *J. Chem. Phys.*, 1949, **17**, 484–495.

215 W. Moffitt, The electronic spectra of cata-condensed hydrocarbons, *J. Chem. Phys.*, 1954, **22**, 320–333.

216 W. Moffitt, Configurational interaction in simple molecular orbital theory, *J. Chem. Phys.*, 1954, **22**, 1820–1829.

217 T. Handa, The interpretation of absorption spectra of condensed polycyclic aromatic hydrocarbons by using a simple resonance theory. I. The resonance structure of the excited state in correlation with Platt's theory, *Bull. Chem. Soc. Jpn.*, 1963, **36**, 235–247.

218 M. Orchin and H. H. Jaffé, *Symmetry, Orbitals, and Spectra*, Wiley, 1971.

219 P. R. Callis, Transition density topology of the L_a and L_b states in indoles and purines, *Int. J. Quantum Chem. Symp.*, 1984, **18**, 579–588.

220 R. M. Richard and J. M. Herbert, Time-dependent density-functional description of the ^1L_a state in polycyclic aromatic hydrocarbons: Charge-transfer character in disguise?, *J. Chem. Theory Comput.*, 2011, **7**, 1296–1306.

221 M. Parac and S. Grimme, A TDDFT study of the lowest excitation energies of polycyclic aromatic hydrocarbons, *Chem. Phys.*, 2003, **292**, 11–21.

222 S. Grimme and M. Parac, Substantial errors from time-dependent density functional theory for the calculation of excited states of large π systems, *ChemPhysChem*, 2003, **4**, 292–295.

223 R. Grotjahn, Learning from the 4-(dimethylamino)benzonitrile twist: Two-parameter range-separated local hybrid functional with high accuracy for triplet and charge-transfer excitations, *J. Chem. Phys.*, 2023, **159**, 174102.

224 D. Rappoport and F. Furche, Photoinduced intramolecular charge transfer in 4-(dimethyl)aminobenzonitrile—a theoretical perspective, *J. Am. Chem. Soc.*, 2004, **126**, 1277–1284.

225 Z. R. Grabowski, K. Rotkiewicz, and W. Rettig, Structural changes accompanying intramolecular electron transfer: Focus on twisted intramolecular charge-transfer states and structures, *Chem. Rev.*, 2003, **103**, 3899–4032.

226 T. Atsbeha, A. M. Mohammed, and M. Redi-Abshiro, Excitation wavelength dependence of dual fluorescence of DMABN in polar solvents, *J. Fluoresc.*, 2010, **20**, 1241–1248.

227 J. Catalán, On the dual emission of *p*-dimethylaminobenzonitrile and its photophysical implications, *Phys. Chem. Chem. Phys.*, 2013, **15**, 8811–8820.

228 D. R. Kanis, M. A. Ratner, and T. J. Marks, Design and construction of molecular assemblies with large second-order optical nonlinearities. Quantum chemical aspects, *Chem. Rev.*, 1994, **94**, 195–242.

229 G. García, C. Adamo, and I. Ciofini, Evaluating push–pull dye efficiency using TD-DFT and charge transfer indices, *Phys. Chem. Chem. Phys.*, 2013, **15**, 20210–20219.

230 D. Pines, E. Pines, T. W. J. Steele, and V. Papper, Dual fluorescence phenomenon in 'push-pull' stilbenes, in *Reviews in Fluorescence 2015*, ed. C. D. Geddes; Springer, 2016; chapter 13, pp. 337–352.

231 H. Imahori, T. Umeyama, and S. Ito, Large π-aromatic molecules as potential sensitizers for highly efficient dye-sensitized solar cells, *Acc. Chem. Res.*, 2009, **42**, 1809–1818.

232 C. Duan, F. Huang, and Y. Cao, Recent development of push-pull conjugated polymers for bulk-heterojunction photovoltaics: Rational design and fine tailoring of molecular structure, *J. Mater. Chem.*, 2012, **22**, 10416–10434.

233 L.-L. Li and E. W.-G. Diau, Porphyrin-sensitized solar cells, *Chem. Soc. Rev.*, 2013, **42**, 291–304.

234 R. C. Jemison and R. D. McCullough, Techniques for the molecular design of push-pull polymers towards enhanced organic photovoltaic performance, in *Polymer Composites for Energy Harvesting, Conversion, and Storage*, ed. L. Li, W. Wong-Ng, and J. Sharp, Vol. 1161 of *ACS Symposium Series;* American Chemical Society, 2014; chapter 4, pp. 71–109.

235 L. Beverina and G. A. Pagani, π-conjugated zwitterions as paradigm of donor-acceptor building blocks in organic-based materials, *Acc. Chem. Res.*, 2014, **47**, 319–329.

236 V. Malytskyi, J.-J. Simon, L. Patrone, and J.-M. Raimundo, Thiophene-based push-pull chromophores for small molecule organic solar cells (SMOSCs), *RSC Adv.*, 2015, **5**, 354–397.

237 Z. Parsa, S. S. Naghavi, and S. N. Shahab, Designing push-pull porphyrins for efficient dye-sensitized solar cells, *J. Phys. Chem. A*, 2018, **122**, 5870–5877.

238 A. Torres, L. R. Prado, G. Bortolini, and L. G. C. Rego, Charge transfer driven structural relaxation in a push–pull azobenzene dye–semiconductor complex, *J. Phys. Chem. Lett.*, 2018, **9**, 5926–5933.

239 I. Ciofini, T. Le Bahers, C. Adamo, F. Odobel, and D. Jacquemin, Through-space charge transfer in rod-like molecules: Lessons from theory, *J. Phys. Chem. C*, 2012, **116**, 11946–11955. Erratum: *J. Phys. Chem. C*, 2012, **116**, 14736.

240 M. P. Balanay and D. H. Kim, Strategic design of bacteriochlorins as possible dyes for photovoltaic applications,

J. Phys. Chem. A, 2017, **121**, 6660–6669.

241 S. Hadsadee, R. Rattanawan, R. Tarsang, N. Kungwan, and S. Jungsuttiwong, Push-pull *n*-annulated perylene-based sensitizers for dye-sensitized solar cells: Theoretical property tuning by DFT/TDDFT, *ChemistrySelect*, 2017, **2**, 9829–9837.

242 S. S. Madugula and S. Yarasi, Molecular design of porphyrin dyes for dye sensitized solar cells: A quantitative structure property relationship study, *Int. J. Quantum Chem.*, 2017, **117**, e25385.

243 B. Basheer, T. M. Robert, K. P. Vijayalakshmi, and D. Mathew, Solar cells sensitized by push-pull azo dyes: Dependence of photovoltaic performance on electronic structure, geometry and conformation of the sensitizer, *Int. J. Amb. Energy*, 2018, **39**, 433–440.

244 F. Castet, V. Rodriguez, J.-L. Pozzo, L. Ducasse, A. Plaquet, and B. Champagne, Design and characterization of molecular nonlinear optical switches, *Acc. Chem. Res.*, 2013, **46**, 2656–2665.

245 M. Kivala and F. Diedrich, Acetylene-derived strong organic acceptors for planar and nonplanar push–pull chromophores, *Acc. Chem. Res.*, 2009, **42**, 235–248.

246 G. N. Lipunova, E. V. Nosova, V. N. Charushin, and O. N. Chupakhin, Functionalized quinazolines and pyrimidines for optoelectronic materials, *Curr. Org. Synth.*, 2018, **15**, 793–814.

247 Y. Olivier, J.-C. Sancho-García, L. Muccioli, G. D'Avino, and D. Beljonne, Computational design of thermally activated delayed fluorescence materials: The challenges ahead, *J. Phys. Chem. Lett.*, 2018, **9**, 6149–6163.

248 M. Kasha, Characterization of electronic transitions in complex molecules, *Discuss. Faraday Soc.*, 1950, **9**, 14–19.

249 G. Brancato, G. Signore, P. Neyroz, D. Polli, G. Cerullo, G. Abbandonato, L. Nucara, V. Barone, F. Beltram, and R. Bizzarri, Dual fluorescence through Kasha's rule breaking: An unconventional photomechanism for intracellular probe design, *J. Phys. Chem. B*, 2015, **119**, 6144–6154.

250 A. P. Demchenko, V. I. Tomin, and P.-T. Chou, Breaking the Kasha rule for more efficient photochemistry, *Chem. Rev.*, 2017, **117**, 13353–13381.

251 V. I. Tomin and A. Włodarkiewicz, Anti-Kasha behavior of DMABN dual fluorescence, *J. Lumin.*, 2018, **198**, 220–225.

252 Z. R. Grabowski and J. Dobkowski, Twisted intramolecular charge transfer (TICT) states: Energy and molecular structure, *Pure Appl. Chem.*, 1983, **55**, 245–252.

253 Z. R. Grabowski, Electron transfer and the structural changes in the excited state, *Pure Appl. Chem.*, 1992, **64**, 1249–1255.

254 N. Ghoneim and P. Suppan, Solvation of TICT* states in solvent mixtures, *Pure Appl. Chem.*, 1993, **65**, 1739–1743.

255 M. Hashimoto and H. Hamaguchi, Structure of the twisted-intramolecular-charge-transfer excited singlet and triplet states of 4-(dimethylamino)benzonitrile as studied by nanosecond time-resolved infrared spectroscopy, *J. Phys. Chem.*, 1995, **99**, 7875–7877.

256 L. Serrano-Andrés, M. Merchán, B. O. Roos, and R. Lindh, Theoretical study of the internal charge transfer in aminobenzonitriles, *J. Am. Chem. Soc.*, 1995, **117**, 3189–3204.

257 J. Dobkowski, J. Wójcik, W. Koźmiński, R. Kołos, J. Waluk, and J. Michl, An experimental test of C–N bond twisting in the TICT state: Syn–anti photoisomerization in 2-(*n*-methyl-*n*-isopropylamino)-5-cyanopyridine, *J. Am. Chem. Soc.*, 2002, **124**, 2406–2407.

258 W. Zhang, Z. Lan, Z. Sun, and K. J. Gaffney, Resolving photoinduced twisted intramolecular charge transfer with vibrational anisotropy and TDDFT, *J. Phys. Chem. B*, 2012, **116**, 11527–11536.

259 H. Li, J. Han, H. Zhao, X. Liu, Y. Luo, Y. Shi, C. Liu, M. Jin, and D. Ding, Lighting up the invisible twisted intramolecular charge transfer state by high pressure, *J. Phys. Chem. Lett.*, 2019, **10**, 748–753.

260 M. A. Kochman and B. Durbeej, Simulating the nonadiabatic relaxation dynamics of 4-(*N,N*-dimethylamino)benzonitrile (DMABN) in polar solution, *J. Phys. Chem. A*, 2020, **124**, 2193–2206.

261 K. A. Zachariasse, T. von der Haar, A. Hebecker, U. Leinhos, and W. Kühnle, Intramolecular charge transfer in aminobenzonitriles: Requirements for dual fluorescence, *Pure Appl. Chem.*, 1993, **65**, 1745–1750.

262 K. A. Zachariasse, M. Grobys, T. von der Haar, A. Hebecker, Y. V. Il'ichev, Y.-B. Jiang, O. Morawski, and W. Kühnle, Intramolecular charge transfer in the excited state. Kinetics and configurational changes, *J. Photochem. Photobiol. A*, 1996, **102**, 59–70.

263 K. A. Zachariasse, M. Grobys, T. von der Haar, A. Hebecker, Y. V. Il'ichev, O. Morawski, I. Rückert, and W. Kühnle, Photoinduced intramolecular charge transfer and internal conversion in molecules with a small energy gap between S_1 and S_2. Dynamics and structure, *J. Photochem. Photobiol. A*, 1997, **105**, 373–383.

264 M. Z. Zgierski, T. Fujiwara, and E. C. Lim, Non-adiabatic photoprocesses of fundamental importance to chemistry: From electronic relaxation of DNA bases to intramolecular charge transfer in electron donor-acceptor molecules, in *Radiation Induced Molecular Phenomena in Nucleic Acids*, ed. M. K. Shukla and J. Leszczynski, Vol. 5 of *Challenges and Advances in Computational Chemistry and Physics;* Springer Science+Business Media, 2008; chapter 15, pp. 395–433.

265 T. Gustavsson, P. B. Coto, L. Serrano-Andrés, T. Fujiwara, and E. C. Lim, Do fluorescence and transient absorption probe the same intramolecular charge transfer state of 4-(dimethylamino)benzonitrile?, *J. Chem. Phys.*, 2009, **131**, 031101.

266 T. Fujiwara, M. Z. Zgierski, and E. C. Lim, The role of the $\pi\sigma^*$ state in intramolecular charge transfer of 4-(dimethylamino)benzonitrile, *Phys. Chem. Chem. Phys.*, 2011, **13**, 6779–6783.

267 A. Perveaux, P. J. Castro, D. Lauvergnat, M. Reguero, and B. Lasorne, Intramolecular charge transfer in 4-

aminobenzonitrile does not need the twist and may not need the bend, *J. Phys. Chem. Lett.*, 2015, **6**, 1316–1320.

268 B. F. E. Curchod, A. Sisto, and T. J. Martínez, Ab initio multiple spawning photochemical dynamics of DMABN using GPUs, *J. Phys. Chem. A*, 2017, **121**, 265–276.

269 J.-S. Yang, K.-L. Liau, C.-M. Wang, and C.-Y. Hwang, Substituent-dependent photoinduced intramolecular charge transfer in *n*-aryl-substituted *trans*-4-aminostilbenes, *J. Am. Chem. Soc.*, 2004, **126**, 12325–12335.

270 T. Fujiwara, C. Reichardt, R. A. Vogt, C. E. Crespo-Hernández, M. Z. Zgierski, and E. C. Lim, Electronic spectra and excited-state dynamics of 4-fluoro-*n,n*-dimethylaniline, *Chem. Phys. Lett.*, 2013, **586**, 70–75.

271 K. A. Zachariasse, A. Demeter, and S. I. Druzhinin, Absence of intramolecular charge transfer with 4-fluoro-*n,n*-dimethylaniline (DMA4F), contrary to an experimental report supported by computations, *J. Phys. Chem. A*, 2017, **121**, 1223–1232.

272 M. V. Bohnwagner and A. Dreuw, Regular fluorescence of 4-fluoro-*N,N*-dimethylaniline: No charge transfer and no twisting, *J. Phys. Chem. A*, 2017, **121**, 5834–5841.

273 M. Kasha, H. R. Rawls, and M. A. El-Bayoumi, The exciton model in molecular spectroscopy, *Pure Appl. Chem.*, 1965, **11**, 371–392.

274 J. B. Birks, Excimers, *Rep. Prog. Phys.*, 1975, **38**, 903–974.

275 S. J. Jang and B. Mennucci, Delocalized excitons in natural light harvesting complexes, *Rev. Mod. Phys.*, 2018, **90**, 035003.

276 S. J. Jang, *Dynamics of Molecular Excitons*, Elsevier, Amsterdam, 2020.

277 F. C. Spano and C. Silva, H- and J-aggregate behavior in polymeric semiconductors, *Annu. Rev. Phys. Chem.*, 2014, **65**, 477–500.

278 B. Alam, H. Jiang, P. M. Zimmerman, and J. M. Herbert, State-specific solvation for restricted active space spin-flip (RAS-SF) wave functions based on the polarizable continuum formalism, *J. Chem. Phys.*, 2022, **156**, 194110.

279 A. K. Chandra and E. C. Lim, Semiempirical theory of excimer luminescence, *J. Chem. Phys.*, 1968, **48**, 2589–2595.

280 A. K. Chandra and E. C. Lim, Semiempirical theory of excimer luminescence. II. Comparison with previous theories and consideration of the transition probability and the stability of the excimer triplet state, *J. Chem. Phys.*, 1968, **49**, 5066–5072.

281 A. L. L. East and E. C. Lim, Naphthalene dimer: Electronic states, excimers, and triplet decay, *J. Chem. Phys.*, 2000, **113**, 8981–8994.

282 R. Improta and V. Barone, Interplay between "neutral" and "charge-transfer" excimers rules the excited state decay in adenine-rich polynucleotides, *Angew. Chem. Int. Ed. Engl.*, 2011, **50**, 12016–12019.

283 F. Plasser, A. J. A. Aquino, W. L. Hase, and H. Lischka, UV absorption spectrum of alternating DNA duplexes. Analysis of excitonic and charge transfer interactions, *J. Phys. Chem. A*, 2012, **116**, 11151–11160.

284 V. A. Spata, W. Lee, and S. Matsika, Excimers and exciplexes in photoiniated processes of oligonucleotides, *J. Phys. Chem. Lett.*, 2016, **7**, 976–984.

285 J. Eisinger, M. Guéron, R. G. Shulman, and T. Yamane, Excimer fluorescence of dinucleotides, polynucleotides, and DNA, *Proc. Natl. Acad. Sci. USA*, 1966, **55**, 1015–1020.

286 M. Guéron, R. G. Shulman, and J. Eisinger, Energy transfer in dinucleotides, *Proc. Natl. Acad. Sci. USA*, 1966, **56**, 814–818.

287 J. Eisinger and R. G. Shulman, Excited electronic states of DNA, *Science*, 1968, **161**, 1311–1319.

288 C. T. Middleton, K. de La Harpe, C. Su, Y. K. Law, C. E. Crespo-Hernández, and B. Kohler, DNA excited-state dynamics: From single bases to the double helix, *Annu. Rev. Phys. Chem.*, 2009, **60**, 217–239.

289 B. Kohler, Nonradiative decay mechanisms in DNA model systems, *J. Phys. Chem. Lett.*, 2010, **1**, 2047–2053.

290 J. Chen, Y. Zhang, and B. Kohler, Excited states in DNA strands investigated by ultrafast laser spectroscopy, in *Photoinduced Phenomena in Nucleic Acids II*, Vol. 356 of *Topics in Current Chemistry;* Springer, 2015; pp. 39–87.

291 S. Sharifzadeh, P. Darancet, L. Kronik, and J. B. Neaton, Low-energy charge-transfer excitons in organic solids from first-principles: The case of pentacene, *J. Phys. Chem. Lett.*, 2013, **4**, 2197–2201.

292 S. Sharifzadeh, C. Y. Wong, H. Wu, B. L. Cotts, L. Kronik, N. S. Ginsberg, and J. B. Neaton, Relating the physical structure and optoelectronic function of crystalline TIPS-pentacene, *Adv. Funct. Mater.*, 2015, **25**, 2038–2046.

293 T. C. Berkelbach, M. S. Hybertsen, and D. R. Reichman, Microscopic theory of singlet exciton fission. II. Application to pentacene dimers and the role of superexchange, *J. Chem. Phys.*, 2013, **138**, 114103.

294 T. C. Berkelbach, M. S. Hybertsen, and D. R. Reichman, Microscopic theory of singlet exciton fission. III. Crystalline pentacene, *J. Chem. Phys.*, 2014, **141**, 074705.

295 N. Monahan and X.-Y. Zhu, Charge transfer–mediated singlet fission, *Annu. Rev. Phys. Chem.*, 2015, **66**, 601–618.

296 M. B. Smith and J. Michl, Singlet fission, *Chem. Rev.*, 2010, **110**, 6891–6936.

297 M. B. Smith and J. Michl, Recent advances in singlet fission, *Annu. Rev. Phys. Chem.*, 2013, **64**, 361–386.

298 T. C. Berkelbach, Electronic structure and dynamics of singlet fission in organic molecules and crystals, *Adv. Chem. Phys.*, 2017, **162**, 1–38.

299 A. Japahuge and T. Zeng, Theoretical studies of singlet fission: Searching for materials and exploring mechanisms, *ChemPlusChem*, 2018, **83**, 146–182.

300 D. Casanova, Theoretical modeling of singlet fission, *Chem. Rev.*, 2018, **118**, 7164–7207.

301 S. W. Eaton, L. E. Shoer, S. D. Karlen, S. M. Dyar, E. A. Margulies, B. S. Veldkamp, C. Ramanan, D. A. Hartzler, S. Savikhin, T. J. Marks, and M. R. Wasielewski, Singlet exciton fission in polycrystalline thin films of a slip-stacked

perylenediimide, *J. Am. Chem. Soc.*, 2013, **135**, 14701–14712.

302 A. K. Le, J. A. Bender, and S. T. Roberts, Slow singlet fission observed in a polycrystalline perylenediimide thin film, *J. Phys. Chem. Lett.*, 2016, **7**, 4922–4928.

303 A. M. Alvertis, S. Lukman, T. J. H. Hele, E. G. Fuemmeler, J. Feng, J. Wu, N. C. Greenham, A. W. Chin, and A. J. Musser, Switching between coherent and incoherent singlet fission via solvent-induced symmetry breaking, *J. Am. Chem. Soc.*, 2019, **141**, 17558–17570.

304 I. Papadopoulos, M. J. Álvaro-Martins, D. Molina, P. M. McCosker, P. A. Keller, T. Clark, A. Sastre-Santos, and D. M. Guldi, Solvent-dependent singlet fission in diketopyrrolopyrrole dimers: A mediating charge trasnfer versus a trapping symmetry-breaking charge separation, *Adv. Energy Mater.*, 2020, **10**, 2001496.

305 A. V. Luzanov, D. Casanova, X. Feng, and A. I. Krylov, Quantifying charge resonance and multiexciton character in coupled chromophores by charge and spin cumulant analysis, *J. Chem. Phys.*, 2015, **142**, 224104.

306 S. A. Bäppler, F. Plasser, M. Wormit, and A. Dreuw, Exciton analysis of many-body wave functions: Bridging the gap between the quasiparticle and molecular orbital pictures, *Phys. Rev. A*, 2014, **90**, 052521.

307 R. J. Bell and P. Dean, Atomic vibrations in vitreous silica, *Discuss. Faraday Soc.*, 1970, **50**, 55–61.

308 R. J. Bell, The dynamics of disordered lattices, *Rep. Prog. Phys.*, 1972, **35**, 1315–1409.

309 J. T. Edwards and D. J. Thouless, Numerical studies of localization in disordered systems, *J. Phys. C: Solid State*, 1972, **5**, 807–820.

310 D. J. Thouless, Electrons in disordered systems and the theory of localization, *Phys. Rep.*, 1974, **13**, 93–142.

311 B. Kramer and A. MacKinnon, Localization: Theory and experiment, *Rep. Prog. Phys.*, 1993, **56**, 1469–1564.

312 S. Tretiak and S. Mukamel, Density matrix analysis and simulation of electronic excitations in conjugated and aggregated molecules, *Chem. Rev.*, 2002, **102**, 3171–3212.

313 T. Meier, Y. Zhao, V. Chernyak, and S. Mukamel, Polarons, localization, and excitonic coherence in superradiance of biological antenna complexes, *J. Chem. Phys.*, 1997, **107**, 3876–3893.

314 S. Mukamel, S. Tretiak, T. Wagersreiter, and V. Chernyak, Electronic coherence and collective optical excitations of conjugated molecules, *Science*, 1997, **277**, 781–787.

315 A. Ishizaki and G. R. Fleming, Quantum superpositions in photosynthetic light harvesting: Delocalization and entanglement, *New J. Phys.*, 2010, **12**, 055004.

316 W. Barford and M. Marcus, Theory of optical transitions in conjugated polymers. I. Ideal systems, *J. Chem. Phys.*, 2014, **141**, 164101.

317 W. Barford and O. R. Tozer, Theory of exciton transfer and diffusion in conjugated polymers, *J. Chem. Phys.*, 2014, **141**, 164103.

318 B. Rice, A. A. Y. Guilbert, J. M. Frost, and J. Nelson, Po-

laron states in fullerene adducts modeled by coarse-grained molecular dynamics and tight binding, *J. Phys. Chem. Lett.*, 2018, **9**, 6616–6623.

319 F. Wegner, Inverse participation ratio in $2 + \varepsilon$ dimensions, *Z. Phys. B*, 1980, **36**, 209–214.

320 A. M. M. Pruisken, Participation ratio in the nonlinear σ-model representation of localization, *Phys. Rev. B*, 1985, **31**, 416–419.

321 G. D. Scholes and C. Smyth, Perspective: Detecting and measuring exciton delocalization in photosynthetic light harvesting, *J. Chem. Phys.*, 2014, **140**, 110901.

322 R. Pastor-Satorras and C. Castellano, Distinct types of eigenvector localization in networks, *Sci. Rep.*, 2016, **6**, 18847.

323 M. Cho, G. R. Fleming, S. Saito, I. Ohmine, and R. M. Stratt, Instantaneous normal mode analysis of liquid water, *J. Chem. Phys.*, 1994, **100**, 6672–6683.

324 J. M. Herbert and J. E. Harriman, Comparison of two-electron densities reconstructed from one-electron density matrices, *Int. J. Quantum Chem.*, 2002, **90**, 355–369.

325 J. H. Burroughes, D. D. C. Bradley, A. R. Brown, R. N. Marks, K. Mackay, R. H. Friend, P. L. Burns, and A. B. Holmes, Light-emitting diodes based on conjugated polymers, *Nature*, 1990, **347**, 539–541.

326 G. Grem, G. Leditzky, B. Ullrich, and G. Leising, Realization of a blue-light-emitting device using poly(*p*-phenylene), *Adv. Mater.*, 1992, **4**, 36–37.

327 D. D. C. Bradley, Conjugated polymer electroluminescence, *Synthetic Met.*, 1993, **54**, 401–415.

328 S. Karg, W. Riess, V. Dyakonov, and M. Schwoerer, Electrical and optical characterization of poly(phenylene-vinylene) light emitting diodes, *Synthetic Met.*, 1993, **54**, 427–433.

329 W. Barford and N. Paiboonvorachat, Excitons in conjugated polymers: Wavefunctions, symmetries, and quantum numbers, *J. Chem. Phys.*, 2008, **129**, 164716.

330 M. Marcus, O. R. Tozer, and W. Barford, Theory of optical transitions in conjugated polymers. II. Real systems, *J. Chem. Phys.*, 2014, **141**, 164102.

331 N. Kirova, Understanding excitons in optically active polymers, *Poly. Int.*, 2008, **57**, 678–688.

332 M. Rohlfing and S. G. Louie, Electron-hole excitations and optical spectra from first principles, *Phys. Rev. B*, 2000, **62**, 4927–4944.

333 S. Sharifzadeh, Many-body perturbation theory for understanding optical excitations in organic molecules and solids, *J. Phys.: Condens. Matt.*, 2018, **30**, 153002.

334 S. Tretiak, V. Chernyak, and S. Mukamel, Two-dimensional real-space analysis of optical excitations in acceptor-substituted carotenoids, *J. Am. Chem. Soc.*, 1997, **119**, 11408–11419.

335 S. Tretiak, K. Igumenshchev, and V. Chernyak, Exciton sizes of conducting polymers predicted by time-dependent density functional theory, *Phys. Rev. B*, 2005, **71**, 033201.

336 K. I. Igumenshchev, S. Tretiak, and V. Y. Chernyak, Excitonic effects in a time-dependent density functional theory,

J. Chem. Phys., 2007, **127**, 114902.

337 E. Zojer, P. Buchacher, F. Wudl, J. Cornil, J. P. Calbert, J. L. Brédas, and G. Leising, Excited state localization in organic molecules consisting of conjugated and nonconjugated segments, *J. Chem. Phys.*, 2000, **113**, 10002–10012.

338 J. Rissler, H. Bässler, F. Gebhard, and P. Schwerdtfeger, Excited states of ladder-type poly-*p*-phenylene oligomers, *Phys. Rev. B*, 2001, **64**, 045122.

339 J. Rissler, Effective conjugation length of π-conjugated systems, *Chem. Phys. Lett.*, 2004, **395**, 92–96.

340 L. Romaner, G. Heimel, H. Wiesenhofer, P. Scandiucci de Freitas, U. Scherf, J.-L. Brédas, E. Zojer, and E. J. W. List, Ketonic defects in ladder-type poly(*p*-phenylene)s, *Chem. Mater.*, 2004, **16**, 4667–4674.

341 E. Hennebicq, C. Deleener, J.-L. Brédas, G. D. Scholes, and D. Beljonne, Chromophores in phenylenevinylene-based conjugated polymers: Role of conformational kinks and chemical defects, *J. Chem. Phys.*, 2006, **125**, 054901.

342 S. A. Mewes, F. Plasser, A. Krylov, and A. Dreuw, Benchmarking excited-state calculations using exciton properties, *J. Chem. Theory Comput.*, 2018, **14**, 710–725.

343 S. A. Mewes, F. Plasser, and A. Dreuw, Communication: Exciton analysis in time-dependent density functional theory: How functionals shape excited-state characters, *J. Chem. Phys.*, 2015, **143**, 171101.

344 S. A. Mewes, J.-M. Mewes, A. Dreuw, and F. Plasser, Excitons in poly(*para* phenylene vinylene): A quantum-chemical perspective based on high-level *ab initio* calculations, *Phys. Chem. Chem. Phys.*, 2016, **18**, 2548–2563.

345 S. A. Mewes, F. Plasser, and A. Dreuw, Universal exciton size in organic polymers is determined by nonlocal orbital exchange in time-dependent density functional theory, *J. Phys. Chem. Lett.*, 2017, **8**, 1205–1210.

346 X. Feng, A. V. Luzanov, and A. I. Krylov, Fission of entangled spins: An electronic structure perspective, *J. Phys. Chem. Lett.*, 2013, **4**, 3845–3852.

347 S. Matsika, X. Feng, A. V. Luzanov, and A. I. Krylov, What we can learn from the norms of one-particle density matrices, and what we can't: Some results for interstate properties in model singlet fission systems, *J. Phys. Chem. A*, 2014, **118**, 11943–11955.

348 N. Mardirossian and M. Head-Gordon, ωB97X-V: A 10-parameter, range-separated hybrid, generalized gradient approximation density functional with nonlocal correlation, designed by a survival-of-the-fittest strategy, *Phys. Chem. Chem. Phys.*, 2014, **16**, 9904–9924.

349 L. Kronik and S. Kümmel, Dielectric screening meets optimally tuned density functionals, *Adv. Mater.*, 2018, **30**, 1706560.

350 S. Tretiak, V. Chernyak, and S. Mukamel, Localized electronic excitations in phenylacetylene dendrimers, *J. Phys. Chem. B*, 1998, **102**, 3310–3315.

351 G. C. Bazan, W. J. Oldham, Jr., R. J. Lachicotte, S. Tretiak, V. Chernyak, and S. Mukamel, Stilbenoid dimers: Dissection of a paracyclophane chromophore, *J. Am. Chem. Soc.*, 1998,

120, 9188–9204.

352 B. M. Wong, Optoelectronic properties of carbon nanorings: Excitonic effects from time-dependent density functional theory, *J. Phys. Chem. C*, 2009, **113**, 21921–21927.

353 J.-L. Jin, H.-B. Li, Y. Geng, Y. Wu, Y.-A. Duan, and Z.-M. Su, Theoretical insight into the origin of large Stokes shift and photophysical properties of anilido-pyridine boron difluoride dyes, *ChemPhysChem*, 2012, **13**, 3714–3722.

354 T. Le Bahers, C. Adamo, and I. Ciofini, A qualitative index of spatial extent in charge-transfer excitations, *J. Chem. Theory Comput.*, 2011, **7**, 2498–2506.

355 P. M. Zimmerman, C. B. Musgrave, and M. Head-Gordon, A correlated electron view of singlet fission, *Acc. Chem. Res.*, 2013, **46**, 1339–1347.

356 A. F. Morrison and J. M. Herbert, Evidence for singlet fission driven by vibronic coherence in crystalline tetracene, *J. Phys. Chem. Lett.*, 2017, **8**, 1442–1448.

357 H. Kim and P. M. Zimmerman, Coupled double triplet state in singlet fission, *Phys. Chem. Chem. Phys.*, 2018, **20**, 30083–30094.

358 M. J. Y. Tayebjee, A. A. Gray-Weale, and T. W. Schmidt, Thermodynamic limit of exciton fission solar cell efficiency, *J. Phys. Chem. Lett.*, 2012, **3**, 2749–2754.

359 M. J. Y. Tayebjee, D. R. McCamey, and T. W. Schmidt, Beyond Shockley–Queisser: Molecular approaches to high-efficiency photovoltaics, *J. Phys. Chem. Lett.*, 2015, **6**, 2367–2378.

360 W.-L. Chan, M. Ligges, and X.-Y. Zhu, The energy barrier in singlet fission can be overcome through coherent coupling and entropic gain, *Nat. Chem.*, 2012, **4**, 840–845.

361 W.-L. Chan, T. C. Berkelbach, M. R. Provorse, N. R. Monahan, J. R. Tritsch, M. S. Hybertsen, D. R. Reichman, J. Gao, and X.-Y. Zhu, The quantum coherent mechanism for singlet fission: Experiment and theory, *Acc. Chem. Res.*, 2013, **46**, 1321–1329.

362 M. J. Y. Tayebjee, R. G. C. R. Clady, and T. W. Schmidt, The exciton dynamics in tetracene thin films, *Phys. Chem. Chem. Phys.*, 2013, **15**, 14797–14805.

363 S. T. Roberts, Singlet to triplet and back again, *Nat. Chem.*, 2015, **7**, 764–765.

364 H. L. Stern, A. Cheminal, S. R. Yost, K. Broch, S. L. Bayliss, K. Chen, M. Tabachnyk, K. Thorley, N. Greenham, J. M. Hodgkiss, J. Anthony, M. Head-Gordon, A. J. Musser, A. Rao, and R. H. Friend, Vibronically coherent ultrafast triplet-pair formation and subsequent thermally activated dissociation control efficient endothermic singlet fission, *Nat. Chem.*, 2017, **9**, 1205–1212.

365 N. R. Monahan, D. Sun, H. Tamura, K. W. Williams, B. Xu, Y. Zhong, B. Kumar, C. Nuckolls, A. R. Harutyunyan, G. Chen, H.-L. Dai, D. Beljonne, Y. Rao, and X.-Y. Zhu, Dynamics of the triplet-pair state reveals the likely coexistence of coherent and incoherent singlet fission in crystalline hexacene, *Nat. Chem.*, 2017, **9**, 341–346.

366 R. Tempelaar and D. R. Reichman, Vibronic exciton theory

of singlet fission. III. How vibronic coupling and thermodynamics promote rapid triplet generation in pentacene crystals, *J. Chem. Phys.*, 2018, **148**, 244701.

367 A. F. Morrison and J. M. Herbert, Analytic derivative couplings and first-principles exciton/phonon coupling constants for an *ab initio* Frenkel-Davydov exciton model: Theory, implementation, and application to compute triplet exciton mobility parameters for crystalline tetracene, *J. Chem. Phys.*, 2017, **146**, 224110.

368 C. B. Dover, J. K. Gallaher, L. Frazer, P. C. Tapping, A. J. Petty II, M. J. Crossley, J. E. Anthony, T. W. Lee, and T. W. Schmidt, Endothermic singlet fission is hindered by excimer formation, *Nat. Chem.*, 2018, **10**, 305–310.

369 Z. L. Cai, K. Sendt, and J. R. Reimers, Failure of density-functional theory and time-dependent density-functional theory for large extended π systems, *J. Chem. Phys.*, 2002, **117**, 5543–5549.

370 Y.-L. Wang and G.-S. Wu, Improving the TDDFT calculation of low-lying excited states for polycyclic aromatic hydrocarbons using the Tamm–Dancoff approximation, *Int. J. Quantum Chem.*, 2008, **108**, 430–439.

371 F. Uhlig, J. M. Herbert, M. P. Coons, and P. Jungwirth, Optical spectroscopy of the bulk and interfacial hydrated electron from ab initio calculations, *J. Phys. Chem. A,* 2014, **118**, 7507–7515.

372 M. B. Robin, Antibonding σ^* orbitals in molecular spectroscopy, *Can. J. Chem.*, 1985, **63**, 2032–2043.

373 M. R. Robin, *Higher Excited States of Polyatomic Molecules*, Vol. III, Academic Press, New York, 1985.

374 W. Graupner, M. Mauri, J. Stampfli, G. Leising, U. Scherf, and K. Mullen, Photo-excited and doping-induced electronic states in a poly(*para*-phenylene)-type ladder polymer, *Solid State Commun.*, 1994, **91**, 7–12.

375 C. Jamorski, J. B. Foresman, C. Thilgen, and H.-P. Lüthi, Assessment of time-dependent density-functional theory for the calculation of critical features in the absorption spectra of a series of aromatic donor–acceptor systems, *J. Chem. Phys.*, 2002, **116**, 8761–8771.

376 C. J. Jamorski and M. E. Casida, Time-dependent density-functional theory investigation of the fluorescence behavior as a function of alkyl chain size for the 4-(n,n-dimethylamino)benzonitrile-like donor–acceptor systems 4-(n,n-diethylamino)benzonitrile and 4-(n,n-diisopropylamino)benzonitrile, *J. Phys. Chem. B*, 2004, **108**, 7132–7141.

377 A. A. Taka, J. M. Herbert, and L. M. McCaslin, Ground-state orbital analysis predicts S_1 charge transfer in donor–acceptor materials, *J. Phys. Chem. Lett.* 2023 (DOI: 10.1021/acs.jpclett.3c02787).

378 M. J. G. Peach, C. R. Le Sueur, K. Ruud, M. Guillaume, and D. J. Tozer, TDDFT diagnostic testing and functional assessment for triazene chromophores, *Phys. Chem. Chem. Phys.*, 2009, **11**, 4465–4470.

379 M. J. G. Peach and D. J. Tozer, Illustration of a TDDFT spatial

380 X. Gui, C. Holzer, and W. Klopper, Accuracy assessment of *GW* starting points for calculating molecular excitation energies using the Bethe–Salpeter formalism, *J. Chem. Theory Comput.*, 2018, **14**, 2127–2136.

381 J. Plötner, D. J. Tozer, and A. Dreuw, Dependence of excited state potential energy surfaces on the spatial overlap of the Kohn–Sham orbitals and the amount of nonlocal Hartree–Fock exchange in time-dependent density functional theory, *J. Chem. Theory Comput.*, 2010, **6**, 2315–2324.

382 B. Moore, II, H. Sun, N. Govind, K. Kowalski, and J. Autschbach, Charge-transfer versus charge-transfer-like excitations revisited, *J. Chem. Theory Comput.*, 2015, **11**, 3305–3320.

383 M. Ehara, R. Fukuda, C. Adamo, and I. Ciofini, Chemically intuitive indices for charge-transfer excitation based on SAC-CI and TD-DFT calculations, *J. Comput. Chem.*, 2013, **34**, 2498–2501.

384 T. Le Bahers, E. Brémond, I. Ciofini, and C. Adamo, The nature of vertical excited states of dynes containing metals for DSSC applications: Insights from TD-DFT and density based indexes, *Phys. Chem. Chem. Phys.*, 2014, **16**, 14435–14444.

385 C. Adamo, T. Le Bahers, M. Savarese, L. Wilbraham, G. García, R. Fukuda, M. Ehara, N. Rega, and I. Ciofini, Exploring excited states using time dependent density functional theory and density-based indexes, *Coord. Chem. Rev.*, 2015, **304–305**, 166–178.

386 J. S. García, F. Maschietto, M. Campetella, and I. Ciofini, Using density based indexes and wave function methods for the description of excited states: Excited state proton transfer reactions as a test case, *J. Phys. Chem. A*, 2018, **122**, 375–382.

387 L. Huet, A. Perfetto, F. Muniz-Miranda, M. Campetell, C. Adamo, and I. Ciofini, General density-based index to analyze charge transfer phenomena: From models to butterfly molecules, *J. Chem. Theory Comput.*, 2020, **16**, 4543–4553.

388 F. Maschietto, M. Campetella, J. S. García, C. Adamo, and I. Ciofini, Chasing unphysical TD-DFT excited states in transition metal complexes with a simple diagnostic tool, *J. Chem. Phys.*, 2021, **154**, 204102.

389 A. D. Laurent, C. Adamo, and D. Jacquemin, Dye chemistry with time-dependent density functional theory, *Phys. Chem. Chem. Phys.*, 2014, **16**, 14334–14356.

390 T. Etienne, Probing the locality of excited states with linear algebra, *J. Chem. Theory Comput.*, 2015, **11**, 1692–1699.

391 P.-F. Loos, M. Comin, X. Blase, and D. Jacquemin, Reference energies for intramolecular charge-transfer excitations, *J. Chem. Theory Comput.*, 2021, **17**, 3666–3686.

392 M. Miura and Y. Aoki, Ab initio theory for treating local electron excitations in molecules and its performance for computing optical properties, *J. Comput. Chem.*, 2009, **30**, 2213–2230.

393 J. Liu and J. M. Herbert, An efficient and accurate approxi-

mation to time-dependent density functional theory for systems of weakly coupled monomers, *J. Chem. Phys.*, 2015, **143**, 034106.

394 J. Liu and J. M. Herbert, Local excitation approximations to time-dependent density functional theory for excitation energies in solution, *J. Chem. Theory Comput.*, 2016, **12**, 157–166.

395 K. D. Closser, Q. Ge, Y. Mao, Y. Shao, Q. Ge, and M. Head-Gordon, Superposition of fragment excitations for excited states of large clusters with application to helium clusters, *J. Chem. Theory Comput.*, 2015, **11**, 5791–5803.

396 D. Mashkovtsev, Y. Orimoto, and Y. Aoki, Fast and accurate calculation of the UV–vis spectrum with the modified local excitation approximation, *J. Chem. Theory Comput.*, 2023, **19**, 5548–5562.

397 C. A. Guido, P. Cortona, and C. Adamo, Effective electron displacements: A tool for time-dependent density functional theory computational spectroscopy, *J. Chem. Phys.*, 2014, **140**, 104101.

398 M. Campetella, F. Maschietto, M. J. Frisch, G. Scalmani, I. Ciofini, and C. Adamo, Charge transfer excitations in TDDFT: A ghost-hunter index, *J. Comput. Chem.*, 2017, **38**, 2151–2156.

399 W. Humphrey, A. Dalke, and K. Schulten, VMD—Visual molecular dynamics, *J. Molec. Graphics*, 1996, **14**, 33–38.

400 T. Lu and F. Chen, Multiwfn: A multifunctional wavefunction analyzer, *J. Comput. Chem.*, 2012, **33**, 580–592.

401 E. Epifanovsky, A. T. B. Gilbert, X. Feng, J. Lee, Y. Mao, N. Mardirossian, P. Pokhilko, A. F. White, M. P. Coons, A. L. Dempwolff, Z. Gan, D. Hait, P. R. Horn, L. D. Jacobson, I. Kaliman, J. Kussmann, A. W. Lange, K. U. Lao, D. S. Levine, J. Liu, S. C. McKenzie, A. F. Morrison, K. D. Nanda, F. Plasser, D. R. Rehn, M. L. Vidal, Z.-Q. You, Y. Zhu, B. Alam, B. J. Albrecht, A. Aldossary, E. Alguire, J. H. Andersen, V. Athavale, D. Barton, K. Begam, A. Behn, N. Bellonzi, Y. A. Bernard, E. J. Berquist, H. G. A. Burton, A. Carreras, K. Carter-Fenk, R. Chakraborty, A. D. Chien, K. D. Closser, V. Cofer-Shabica, S. Dasgupta, M. de Wergifosse, J. Deng, M. Diedenhofen, H. Do, S. Ehlert, P.-T. Fang, S. Fatehi, Q. Feng, T. Friedhoff, J. Gayvert, Q. Ge, G. Gidofalvi, M. Goldey, J. Gomes, C. E. González-Espinoza, S. Gulania, A. O. Gunina, M. W. D. Hanson-Heine, P. H. P. Harbach, A. Hauser, M. F. Herbst, M. Hernández Vera, M. Hodecker, Z. C. Holden, S. Houck, X. Huang, K. Hui, B. C. Huynh, M. Ivanov, A. Jász, H. Ji, H. Jiang, B. Kaduk, S. Kähler, K. Khistyaev, J. Kim, G. Kis, P. Klunzinger, Z. Koczor-Benda, J. H. Koh, D. Kosenkov, L. Koulias, T. Kowalczyk, C. M. Krauter, K. Kue, A. Kunitsa, T. Kus, I. Ladjánszki, A. Landau, K. V. Lawler, D. Lefrancois, S. Lehtola, R. R. Li, Y.-P. Li, J. Liang, M. Liebenthal, H.-H. Lin, Y.-S. Lin, F. Liu, K.-Y. Liu, M. Loipersberger, A. Luenser, A. Manjanath, P. Manohar, E. Mansoor, S. F. Manzer, S.-P. Mao, A. V. Marenich, T. Markovich, S. Mason, S. A. Maurer, P. F. McLaughlin, M. F. S. J. Menger, J.-M. Mewes, S. A. Mewes, P. Morgante, J. W. Mullinax, K. J. Oosterbaan, G. Paran, A. C. Paul, S. K. Paul, F. Pavošević, Z. Pei, S. Prager, E. I. Proynov, A. Rák, E. Ramos-Cordoba, B. Rana, A. E. Rask, A. Rettig, R. M. Richard, F. Rob, E. Rossomme, T. Scheele, M. Scheurer, M. Schneider, N. Sergueev, S. M. Sharada, W. Skomorowski, D. W. Small, C. J. Stein, Y.-C. Su, E. J. Sundstrom, Z. Tao, J. Thirman, G. J. Tornai, T. Tsuchimochi, N. M. Tubman, S. P. Veccham, O. Vydrov, J. Wenzel, J. Witte, A. Yamada, K. Yao, S. Yeganeh, S. R. Yost, A. Zech, I. Y. Zhang, X. Zhang, Y. Zhang, D. Zuev, A. Aspuru-Guzik, A. T. Bell, N. A. Besley, K. B. Bravaya, B. R. Brooks, D. Casanova, J.-D. Chai, S. Coriani, C. J. Cramer, G. Cserey, A. E. DePrince III, R. A. DiStasio Jr., A. Dreuw, B. D. Dunietz, T. R. Furlani, W. A. Goddard III, S. Hammes-Schiffer, T. Head-Gordon, W. J. Hehre, C.-P. Hsu, T.-C. Jagau, Y. Jung, A. Klamt, J. Kong, D. S. Lambrecht, W. Liang, N. J. Mayhall, C. W. McCurdy, J. B. Neaton, C. Ochsenfeld, J. A. Parkhill, R. Peverati, V. A. Rassolov, Y. Shao, L. V. Slipchenko, T. Stauch, R. P. Steele, J. E. Subotnik, A. J. W. Thom, A. Tkatchenko, D. G. Truhlar, T. Van Voorhis, T. A. Wesolowski, K. B. Whaley, H. L. Woodcock III, P. M. Zimmerman, S. Faraji, P. M. W. Gill, M. Head-Gordon, J. M. Herbert, and A. I. Krylov, Software for the frontiers of quantum chemistry: An overview of developments in the Q-Chem 5 package, *J. Chem. Phys.*, 2021, **155**, 084801.

402 Ohio Supercomputer Center, http://osc.edu/ark:/19495/f5s1ph73 (accessed 2023-11-11).